Cell penetration of supramolecular sunscreen components and the effects of these components on UVA-irradiation of cells

Biao Shen

A Thesis
in
The Department
of
Biology

Presented in Partial Fullfillment of the Requirements
for the Degree of Master of Science at
Concordia University
Montreal, Quebec, Canada

June 2003

National Library
of Canada

Acquisitions and
Bibliographic Services

395 Wellington Street
Ottawa ON K1A 0N4
Canada

Bibliothèque nationale
du Canada

Acquisisitons et
services bibliographiques

395, rue Wellington
Ottawa ON K1A 0N4
Canada

Your file Votre référence
ISBN: 0-612-83851-X
Our file Notre référence
ISBN: 0-612-83851-X

ABSTRACT

Cell penetration of supramolecular sunscreen components
and the effects of these components on UVA-irradiation of cells

Biao Shen

Sunburn, pigmentation, hyperplasia, immunosuppression, and vitamin D synthesis represent acute responses of the skin to solar ultraviolet radiation, whereas photoaging and photocarcinogenesis constitute chronic effects. Sunscreens are known to protect against sunlight-induced erythema and sunburn. However, a number of studies demonstrated that UV-irradiated sunscreen components such as PABA and TiO_2, when in contact with skin cells, cause biological damage (*e.g.*, to DNA or enzymes) through facilitating generation of reactive oxygen species (ROS) in cells. Therefore, novel supramolecular sunscreens are under development based on zeolites (porous material) as hosts with sunscreen components as guests. Encapsulation should alleviate adverse side effects by preventing direct contact of the sunscreen guests with skin cells.

Supramolecular sunscreens involving the use of supramolecular composites based on zeolite hosts may reduce or even eliminate biomolecular damage by sunscreen components such as titanium dioxide (TiO_2). The focus of this research is to examine the penetration, if any, of zeolite particles into cells (rat keratinocytes and human skin fibroblasts). Zeolites modified with fluorophores were used to obtain a distribution profile within cells using confocal microscopy. Fluorescent probes that can be taken up by viable cells were further used to examine the release of guests from the zeolite hosts. The protective effect of zeolites against the production of harmful ROS caused by UV-irradiation was examined by observing H_2O_2 generation in cells using confocal

microscopy. The results revealed that zeolites do not penetrate cells and they reduce the amount of ROS produced by UV-irradiation of cells. The data presented here will help in the design of supramolecular sunscreens.

ACKNOWLEDGMENTS

I would like to express my sincere gratitude to all those who helped me fulfill this task, especially to:

Dr. Ann M. English, my supervisor, for giving me this opportunity to study and do research in her laboratory, and for her guidance, encouragement, kindness and patience during my time at Concordia University.

Dr. Paul Joyce and Dr. Reginald K. Storms, my Research Committee Members, for their invaluable comments and scientific guidance.

All members in the Departments of Biology and Chemistry & Biochemistry, particularly Aleksandrs J. Spurmanis for always being so helpful and for showing me how to master confocal microscopy.

My colleagues and friends: Dr. Farida Mohamed, Pascal Turcotte, Menwei Ye, Heng Jiang, Limei Tao, Hasnain Jaffer, Dave Yeung, Georgia Kremmydiotis, Mihai Ciortea, and Vira Patel. Their frequent discussions, suggestions, and friendship helped me to overcome all obstacles during the course of my work.

My parents and my wife, for their love and endless support of every kind. I dedicate this thesis to the special memory of my father and my unborn twin boys.

TABLE OF CONTENTS

PAGE

LIST OF FIGURES

FIGURE PAGE

LIST OF TABLES

TABLE PAGE

Abbreviations

The following abbreviations are used in this thesis:

cF	6-carboxyfluorescein
cFDA	6-carboxyfluorescein diacetate
CMTMR	5-(and-6)-(((4-chloromethyl)benzoyl)amino)tetramethylrhodamine
CuZnSOD	copper zinc superoxide dismutase
DCF	2',7'-dichlorofluorescein
DCFH	2',7'-dichlorofluorescin
DCFH-DA	2',7'-dichlorofluorescin diacetate
DIC	differential interference contrast
DMEM	Dulbecco's modified Eagle's medium
FCS	fetal calf serum
F@NaY	fluorescein-modified faujasite
HBSS	Hank's Balanced Salt Solution
LSCM	laser scanning confocal microscopy
MnSOD	manganese superoxide dismutase
NaY	faujasite Y
PBS	phosphate buffered saline
$Ru(bipy)_3^{2+}$	2,2'-bipyridine ruthenous dichloride hexahydrate
Ru@NaY	$Ru(bipy)_3^{2+}$-modified faujasite
SOD	superoxide dismutase
TEMPOL	4-hydroxy-2,2,6,6-tetramethylpiperydine-1-oxyl (4-hydroxy Tempo)
TiO_2	titanium dioxide

TP^+	2,4,6-triphenylpyrylium; TiO_2, titanium dioxide
TiO_2+NaY	free TiO_2 plus free NaY
TP@β	triphenylpyrylium-modified β-nanocrystalline
TiO_2@NaY	TiO_2 encapsulated in faujasite
UVA	ultraviolet A
UVB	ultraviolet B
UVC	ultraviolet C
UVR	ultraviolet radiation
YPD	yeast extract, peptone and D-glucose

Introduction

1.1 Solar radiation

1.1.1 Sunlight composition at the earth's surface

We know that solar rays can cause irreversible photo damage to the skin. Initially, skin damage starts as sunburn, tanning, and increased freckling. In addition to this, cumulative damage can occur and manifest as pigmentation, skin cancer, and solar keratosis. In practical terms, the biologically important output from the sun reaching the earth's surface can be divided into three wavelength regions: ultraviolet (180 – 400 nm), visible light (400 – 700 nm), and infrared (700 – 10^6 nm), which are about 15%, 60% and 25%, respectively, of total solar radiation reaching the earth's surface. Visible light does not appear to be harmful to healthy individuals. Infrared is essentially heat, and although nonsolar sources can cause skin tumors and cataracts, it is uncertain at present if the infrared in sunlight contributes significantly to the problem of skin cancer (1). Even though UV radiation (UVR) is the smallest fraction of terrestrial solar radiation, it is nonetheless the most energetic and induces biological damage to living systems. Thus, the major sources of the damaging effects of sunlight are primarily from its UV portion.

1.1.2 Ultraviolet radiation

UVR is divided into 3 different types, namely UVC (180 – 280 nm), UVB (280 – 320 nm) and UVA (320 – 400 nm). UVC is very toxic and carcinogenic to humans. Fortunately, virtually all UVC is filtered out by the earth's ozone layer, which is a canopy of a special form of oxygen in the atmosphere that is able to block out most of the harmful radiation in sunlight. While UVB is also filtered out by the ozone layer, about 1% reaches the earth's surface. UVA, unlike UVC and UVB, is largely unaffected by the ozone layer and about 99% of it reaches the earth's surface. Hence, UVA makes up 90 to 95% of total UVR exposure on the surface of earth (Figure 1).

1.2 Properties of human skin

The skin, composed of specialized epithelial and connective tissue cells, is divided into the epidermis, dermis (Figure 2) and hypodermis (subcutis). Human skin consists of various types of cells that form the epidermal layer. The upper portion, or stratum corneum, is composed of dead keratinocytes. The basal layer between the dermis and the stratum corneum is made up of actively proliferating cells and contains melanocytes that produce melanin. Melanosomes (granules containing melanin) are present in melanocyte dendrites and these granules are transferred to surrounding keratinocytes. The melanocytes tend to form a cap over the keratinocyte nucleus and partially protect it from UVR. Cells produced in the proliferating basal layer move to the surface of the epidermis where they become flattened to form, ultimately, the dense protective keratin matrix of the stratum corneum. The dermis consists of irregularly arranged fibrous tissues containing a network of collagen and elastic fibers, together with an extensive capillary blood supply. It also contains fibroblasts, histiocytes, endothelial cells, and dendritic cells. The hypodermis contains adipose tissue and serves to attach the dermis to its underlying tissues.

The basal keratinocyte is a mitotically active cell (analogous to the stem cell of bone marrow), which differentiates from the basal form (least keratin) to the cornified form

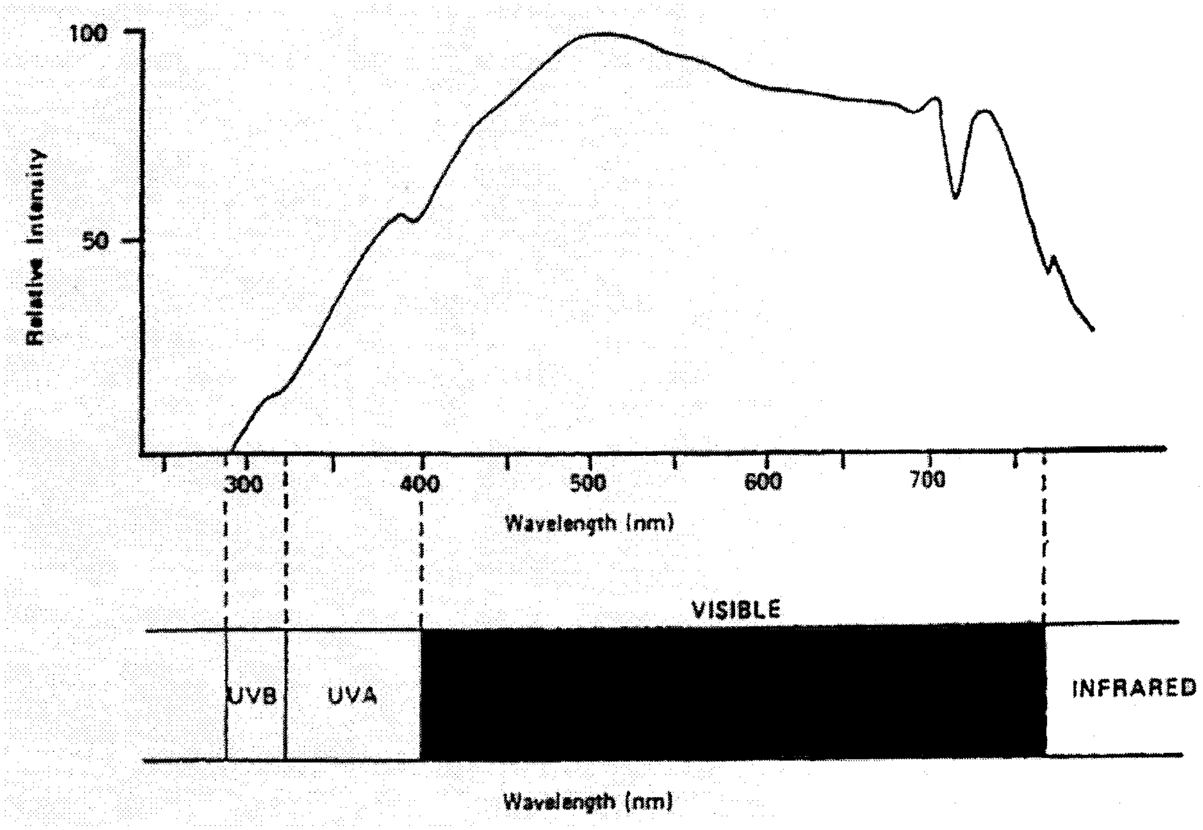

Figure 1. Sunlight spectrum reaching the Earth's surface (2).

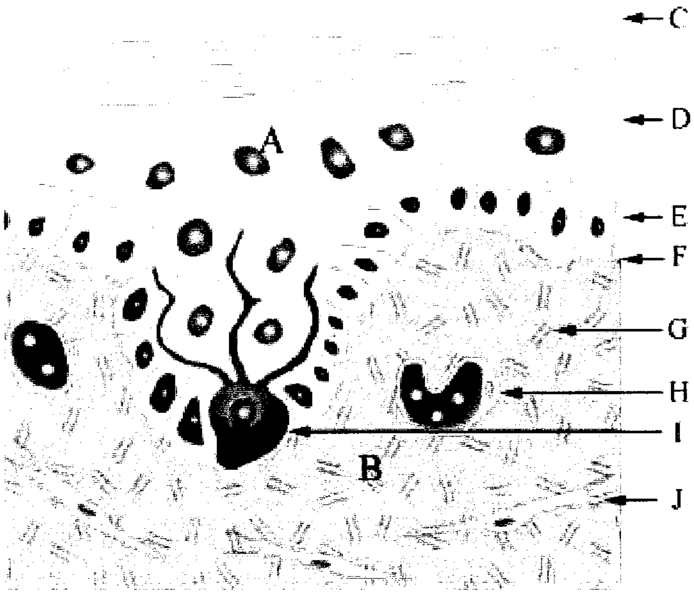

A = Epidermis
B = Dermis
C = Stratum corneum
D = Suprabasal keratinocytes
E = Basal layer
F = Basement membrane
G = Collagen fibers in dermis
H = Capillary (enclosed by a single microvascular endothelial cell)
I = Melanocyte
J = Fibroblast

Figure 2. A transverse section of human skin illustrating the epidermis, basement membrane, dermis, capillaries and major cellular components. The hypodermis (not shown) serves to attach the dermis (B) to its underlying tissues.
From *www.cascadebio.com/.../ Skin%20cross%20section.html*

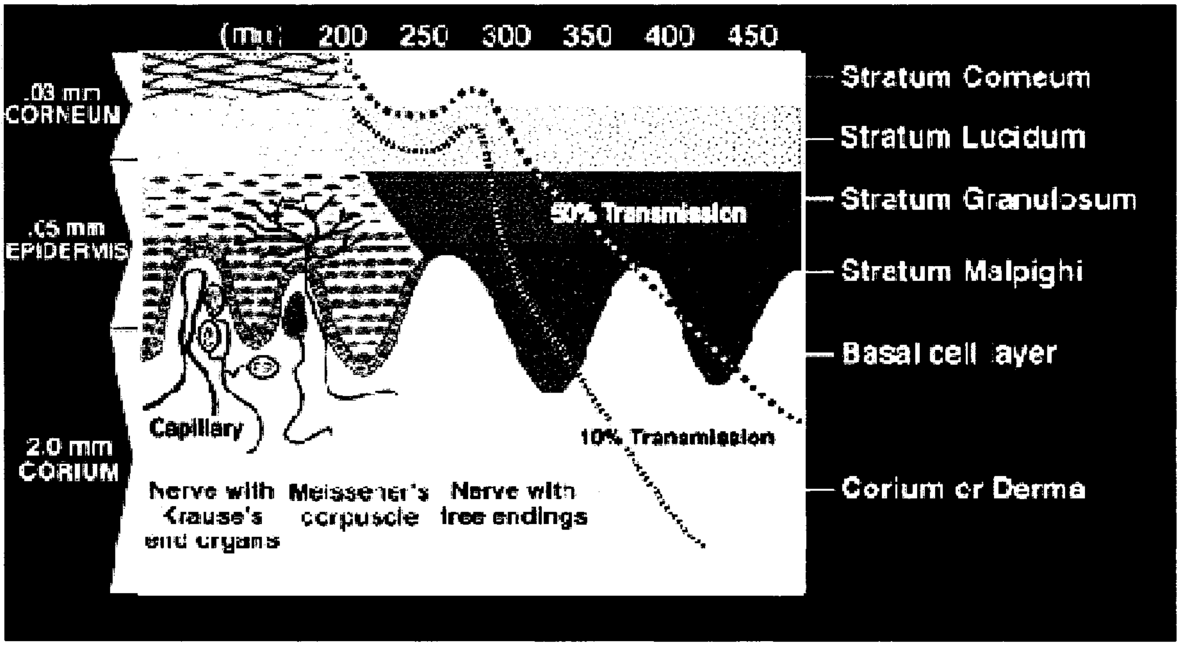

Figure 3. Penetration of human skin by ultraviolet energy.
From *medlib.med.utah.edu/kw/ derm/pages/meet_2.html*

(most keratin). As it migrates upward, there is progressive synthesis of keratin proteins, which constitute part of the protective interface between the body and the environment. Fibroblast cells in the skin synthesize collagen, elastin and reticulin.

1.2.1 Effects of UVR on skin

UVR effects the skin in a variety of ways. In addition to sunburn, UVR provokes photoallergies and reactions of the skin in susceptible individuals. It is also an important factor in the development of skin aging and skin cancer. The UVR-induced skin effects manifest as acute responses such as sunburn, pigmentation, hyperplasia, immunosuppression and vitamin D synthesis (3) and chronic effects, primarily photocarcinogenesis and photoaging (4). During photocarcinogenesis, UVR works as both an initiator by directly damaging DNA and as a promoter by suppressing immunologic rejection (5). Much evidence has shown that exposure to UVR from sunlight causes skin cancers, and also accelerates aging of human skin, characterized by dryness, roughness, irregular pigmentation such as wrinkling, actinic keratoses, elastosis, inelasticity and freckling (6). UVR is absorbed by different molecular species, including proteins, DNA and lipids at various wavelength-dependent depths (Figure 3). This is very important since specific tumor types are associated with different cell types.

Skin damage caused by UVR is not just thermal injury. UVR damages small vessels and cells in the skin. The net result is that small vessels leak and inflammatory chemicals, including histamine and prostaglandins, are released. UVB is about 1000 times more effective than UVA in inducing sunburn. UVB is strongly absorbed by DNA, which results in chromosomal damage that is a major cause of lethal and tumorigenic events.

Cancer may be viewed as a disease that progresses through multiple stages that involve initiation, promotion, progression, and metastasis. Each stage is accompanied by further changes in DNA. UVB is considered to be the major cause of skin cancers and animal studies indicate that it is the major action spectrum for melanoma formation (1). The longer wavelengths penetrate deeper into the subcutis. UVA penetrates into the middle of the dermis whereas UVB just penetrates into the epidermis but not into the dermis (Figure 3). Hence, much of the sun's UVA damage occurs in the dermis and epidermis, and UVB damage in the epidermal layer. It is estimated that 19 to 50% of solar UVA reaches the depth of the melanocytes, whereas only 9 to 14% of solar UVB reaches these cells (7).

Possibly because of its ability to penetrate more deeply into the skin, UVA is more responsible for photoaging and wrinkling of the skin, and also is linked to the formation of skin cancer. Studies indicate that about 90% of sunlight's melanoma-causing effect may come from UVA rays with only 10% from UVB rays (7). UVA is absorbed very poorly by DNA, but it is capable of damaging DNA via photosensitized reactions that result in production of ROS, including superoxide anion ($O_2^{\bullet -}$) and the hydroxyl radical ($HO^{\bullet}$), as well as nonradical species such as hydrogen peroxide (H_2O_2) and singlet oxygen ($^1O_2$). These ROS can cause single-strand breaks, mutations, sister chromatid exchanges, and chromosomal aberrations that can result in cytotoxicity and carcinogenesis. Furthermore, the ROS generated by UVA can damage mitochondria and induce apoptosis in cell cultures (7). In cases of increased ROS generation, antioxidant enzymes (CuZnSOD, MnSOD and catalase) may be overwhelmed, resulting in oxidative stress and oxidative protein damage (8, 9).

Clouds and fog cannot block the more energetic and shorter wavelength UVR and this is why it is still possible to be sunburned on an overcast day. Studies on UVR protection offered by cotton fabrics used in summer clothing show that a substantially greater percent transmission of UVA, as compared with UVB, occurred through these fabrics. This means that people wearing summer clothing may receive substantially higher UVA than UVB exposure. The longer wavelength of UVA also allows it to pass through most window glass, whereas UVB is blocked (7). On the other hand, UVB rays are most intense between the hours of 10:00 to 14:00, while the intensity of UVA rays remains constant throughout all daylight hours (7). Consequently, protection against UVA radiation is likely as important as protection against UVB radiation.

1.3 Sunscreens

Although sun exposure is a destructive force to human skin, it is not necessary (or realistic) for humans to become nocturnal or avoid exposure to the sun at all costs. The sun provides psychological and physiological benefits. Being outdoors makes people feel good and elevates their mood. Sunlight provides a physiological benefit by causing the skin to manufacture vitamin D from cholesterol precursors in the skin, which historically was an important means of avoiding rickets. Studies provide evidence that sunscreens used on a regular year-round basis provide substantial protection from sun-induced skin lesions (1, 10). Some individuals may experience equivalent amounts of sunlight exposure to the face, neck, and arms in winter months as in the summer. Exposure to UVR always produces more skin damage in unprotected than in sunscreen-protected skin because the acute and chronic effects of UVR are dose-, time- and wavelength-dependent, and sunscreens reduce the dose of UVR.

Sunscreens are UVR-absorbing chemicals that attenuate the amount of UVR reaching the skin. Photoprotection is concerned with the reduction of exposure to UVR, specifically UVB and UVA, from the sun. The protection provided by a sunscreen is indicated by the sun protection factor (SPF), which is approved by the U.S. Food and Drug Administration (FDA), and measures the effectiveness of blockage against UVB radiation only. There is no current standard to measure UVA protection. The SPF number is a guide for the consumer, which helps people determine how long they can stay in the sun without burning as compared to the normal amount of time it takes to obtain a sunburn. UVR is considered to be the major cause of skin cancer and UVB to be a major risk factor for melanoma (1, 7). Sunscreens, which block the penetration of UVR through the epidermis by acting as filters and absorbing and reflecting UVR, can be expected to have a substantial impact in reducing the incidence of melanoma and nonmelanoma skin cancers in those individuals who use them regularly (1).

1.3.1 Active sunscreen ingredients

Chemical sunscreens block the penetration of UVR through the epidermis by acting as filters and absorbing and reflecting high-energy UV. The ingredients used in sunscreen products in the United States and approved by the FDA (11) are listed in Table 1. These ingredients are divided in two categories: organic and inorganic. The organic sunscreens are referred to as soluble or chemical sunscreens. The inorganic sunscreens are commonly known as physical, mineral, insoluble, natural or nonchemical sunscreens. The

Table 1. List of FDA-approved sunscreen ingredients and maximum concentrations*

Ingredients	Max. concentration (%)	Comment
Aminobenzoic acid (PABA)	15	Rarely used
Avobenzone	3	Currently four products
Benzoate (Padimate-O)	8	
Cinoxate	3	Rarely used
Dioxybenzone	3	Rarely used
Homosalate	15	
Menthyl anthranilate	5	
Octocrylene	10	Found in many recreational sunscreen products
Octyl methoxycinnamate (OMC)	7.5	Found in over 90% of sunscreen products used in the world
Octyl salicylate	5	Used in oxybenzone/OMC primarily for its solvent properties
Oxybenzone	6	Combined with OMC in many beach products
Phenylbenzimidazole sulfonic acid (PBSA)	4	Used in combination with OMC in daily UV protectant products
Sulisobenzone	10	Rarely used
Trolamine salicylate	12	
Titanium dioxide	25	
Zinc oxide	25	

* Data from the 1995 Federal Register of the USA (11)

distinction between these two categories of sunscreens is based on mechanism of action.

Organic sunscreens have been the mainstay of sunscreen formulation for decades. Organic molecules are capable of absorbing and converting UV light into heat through a process known as cyclic photochemistry (6). One of the first commercially and widely used sunscreen was *p*-aminobenzoic acid (PABA), which absorbs UVB (12, 13). Padimate-O is a PABA derivative that was introduced later into sunscreens. It was an attractive sunscreen component because it is virtually insoluble in water and is a colorless oily liquid easily incorporated into lotions and it clings well to the skin. Currently, the most widely used organic sunscreen is octyl methoxycinnamate (OMC).

The inorganic materials, which have been used as sunscreens with increasing frequency during this decade, act as light scatterers. The most commonly used scatterers are titanium dioxide (TiO_2) and zinc oxide (ZnO). Both exist as odorless white powders, and the particles scatter or absorb UV and visible light in a manner that depends on their size. TiO_2 and ZnO are divided into several general grades depending on their sizes (Table 2). Any color rendered to a sunscreen by an ingredient, so-called whitening, is undesirable for cosmetic reasons. Thus, the average particle size of a metal oxide is reduced below the optimal light scattering size, ~ 200 nm, allowing visible light to be transmitted and so that the particles appear transparent. Since micronized metal oxides are transparent to visible radiation, they are used in cosmetic products. Studies have shown that the smaller the particle size, the less UV light is transmitted, and the more UVB and UVA protection is expected (14). The intensity of scattering is proportional to the refractive index of a material, and since the refractive index of ZnO is lower, it is more transparent than TiO_2. TiO_2 is a UVB absorber and a UVA scatterer (15). TiO_2 has

Table 2. Primary particle size of TiO_2 and ZnO

<table>
<tr><th colspan="2"></th><th>Pigmentary</th><th>Micronized
(microfine)</th><th colspan="2">Attenuation
(ultrafine)</th></tr>
<tr><td rowspan="3">Size
(nm)</td><td rowspan="2">TiO_2</td><td rowspan="2">> 200</td><td rowspan="2">60 - 100</td><td>Medium</td><td>Small</td></tr>
<tr><td>35 - 60</td><td>15 - 35</td></tr>
<tr><td>ZnO</td><td>> 200</td><td>60 - 200</td><td colspan="2">15 - 35</td></tr>
</table>

excellent protection against UVB at small particle size. However, to optimize UVA protection, the TiO_2 particle size should be increased slightly, because scattering intensity increases with particle size (14). At the right size, TiO_2 can be very effective in UVA protection. The common polymorphs of TiO_2 are the anatase and rutile forms, and both are used in sunscreens (16). ZnO attenuates UVA and UVB mainly by its absorption, and protection is inversely related to its particle size, the smaller the size, the higher the absorption and protection (14). Generally, ZnO provides better UVA protection than TiO_2 because it absorbs UVA strongly.

The majority of the commercially available products today use sunscreens in combination. No single sunscreen ingredient, used at levels currently allowed by the FDA, can provide a high SPF. Further, individual sunscreen ingredients have a relatively narrow absorption spectrum that can be broadened by combinations. Most recently, the combination of organic and inorganic sunscreen ingredients has become increasingly popular in sunscreen products. Sun protection should not be limited to avoiding sunburns. It should also minimize long-term skin damage and decrease the risk of skin cancer associated with sun exposure.

1.3.2 Effects of sunscreens on skin exposure to UVR

Sunscreens are increasingly included in diverse consumer products. Given this, questions regarding their safety, particularly in the presence of UVR exposure have been raised. In general, studies have been conducted to identify what effect sunscreens have on UVR-induced damage, either genetic or cytotoxic, and, by inference, UVR-induced skin carcinogenesis. These studies, which have been built on *in vitro* findings using preparations of naked DNA or cultured cells, have found that following irradiation, sunscreens may attack DNA either directly or indirectly through free radicals to produce damage in the form of adducts or cell death (17 – 23).

Organic sunscreens are usually in contact with biological materials and can be absorbed by the skin and come into direct contact with live tissue (24, 25). Such contact and absorption can have adverse effects, particularly, in combination with exposure to UVR. *In vitro* studies show that PABA-like sunscreens were potential carcinogens and that Padimate-O, a derivative of PABA, was harmless in the dark but mutagenic following exposure to solar-simulated radiation (SSR) from an artificial light source. These data suggest that PABA-like sunscreens might represent a human hazard if applied and exposed to UVR from sunlight as intended (6, 26). Many organic sunscreen ingredients, with PABA being the most efficient, are good triplet state sensitizers with the potential to convert harmless triplet oxygen ($^3O_2$) into singlet oxygen ($^1O_2$), a well-known cytotoxic species (27). Oxidative damage to amino acids, particularly histidine, tryptophan, and cysteine, as well as nucleic acids, proteins, and lipids, as a result of reaction with $^1O_2$ is known to occur (28). The reaction of $^1O_2$ with cellular lipids results in the formation of lipid peroxides that decompose, forming highly reactive free radical species that can lead to genotoxic effects (29). Padimate-O is known to cause indirect DNA damage (strand breaks) with UV irradiation (20, 21, 22). Padimate-O penetrates human skin (24) and any Padimate-O in contact with the cells substantially increases strand breaks following UVR exposure (19).

Although TiO_2 and ZnO have been used for years in consumer products and are generally considered to be inert, recent photocatalytic applications of TiO_2 have led some to a reconsideration of their effect in sunscreens. TiO_2 is susceptible to excitation by UVB and UVA in sunlight. It is a semiconductor with a band gap in the region of 3.0 eV, corresponding to light at wavelengths below ~380 nm, which is the UVR region. Under certain conditions, TiO_2 can generate free radicals (30, 31). Absorption of UV by TiO_2 results in the formation of electrons (e^-) and holes (h^+). The electron is a reducing agent, whereas the hole is a powerful oxidizing agent. Usually, the electron recombines with the hole, but sometimes the hole migrates to the surface of the particle, where it can react with absorbed species. In an aqueous environment, electrons can react with oxygen (reaction 3) and holes with water or hydroxyl ions (reaction 2), forming hydroxyl radicals (17). A number of ROS may be subsequently generated in aqueous solutions (reactions 3-8). The photocatalytic activity of anatase TiO_2 is greater than that of the rutile form (17) because its optical band gap is greater (3.23 eV *vs* 3.06 eV). Hence, UVA-irradiation of

$$TiO_2 \xrightarrow[\lambda = 350\text{ nm}]{h\nu} \text{hole}^+ + e^- \qquad (1)$$

$$\text{hole}^+ + H_2O \longrightarrow HO^\bullet + H^+ \qquad (2)$$

$$O_2 + e^- \longrightarrow O_2^{\bullet -} \qquad (3)$$

$$O_2^{\bullet -} + H^+ \longrightarrow HO_2^{\bullet} \qquad (4)$$

$$HO_2^{\bullet} + HO_2^{\bullet} \longrightarrow H_2O_2 + O_2 \qquad (5)$$

$$H_2O_2 + O_2^{\bullet -} \longrightarrow HO^- + HO^{\bullet} + O_2 \qquad (6)$$

$$\text{hole}^+ + HO^- \longrightarrow HO^{\bullet} \qquad (7)$$

$$H_2O_2 + e^- \longrightarrow HO^- + HO^{\bullet} \qquad (8)$$

anatase TiO_2 should generate electrons and holes more efficiently than irradiation of rutile TiO_2 (32). The photocatalytic activity of TiO_2 has been used experimentally to degrade suspensions of organic materials, treat contaminated waters and purify drinking water (33).

There is evidence that TiO_2 particles are capable of penetrating into the lower layers of the skin (34). Studies have shown that the use of sunscreens containing microfine TiO_2 (30-220 nm) can result in the percutaneous absorption of titanium (23, 34). Investigations also have shown that TiO_2 in sunscreens penetrates the human stratum corneum and hair follicles (35). TiO_2 particles were incorporated into the cytoplasm of human skin fibroblasts *in vitro* (18) and also into Hela cells (23). The distribution of TiO_2 in HeLa cells was observed using a transmission electron microscope (23), and particles were observed in the cytoplasm. HeLa cells were killed in the presence of TiO_2 following short UV-irradiation times (~10 min at <100 μg TiO_2/cm^2), whereas more than 90% of the control cells (no TiO_2) remained alive. Thus, photoexcitation of TiO_2 not only in the cell membrane, but also in the cytoplasm is toxic to cells (23). Other investigators concluded that greater permeability to calcium following membrane damage may play a role in TiO_2-sensitized phototoxicity in cells (18, 36, 37). *In vitro* studies demonstrate that both TiO_2 and ZnO produced DNA stand-breaking, converting supercoiled plasmid DNA to a relaxed and ultimately liner form after irradiation (17, 31). It was suggested that the DNA stand-breaking activity of irradiated TiO_2 is due to ROS since effects could be reduced in the presence of free radical scavengers (17). Wamer *et al.* (18) demonstrated that cellular nucleic acids, particularly RNA, are targets for photoxidative damage sensitized by TiO_2. The enzyme horseradish peroxidase is extensively inactivated by UVA exposure in the presence of TiO_2 (38). *In vitro* studies in our lab showed that catalase and CuZn-superoxide dismutase (CuZnSOD) are rapidly inactivated when irradiated in the presence of TiO_2. The ROS generated in TiO_2 solutions upon UVA irradiation presumably attack and inactivate these enzymes.

Any new generation sunscreen composition must protect against both UVB and UVA, unlike most current sunscreens, which are mainly UVB filters. A combination of both organic and inorganic components will most likely make it easier to achieve this. But in conventional sunscreens the question of possible intermolecular interactions, leading to potential hazards, or loss of activity is of concern since it is known that TiO_2 interacts with the organic components of these mixtures.

1.4 Supramolecular sunscreen components

Our overall goal is to develop and test sunscreens based on supramolecular chemistry. The concept of encapsulation is widely employed by the pharmaceutical industry as a way of preventing direct contact of chemicals with non-target biological materials, or to achieve slow release of drugs. In these novel sunscreens, submicron particles of a well-defined porous material, zeolites, will be used as hosts for the actual sunscreen composed of organic or inorganic molecules (39). Zeolites are non-toxic and they are widely used as dietary supplements in animal feeds, filters for drinking water and have had success in the healing of cuts and wounds (40). Zeolites can be prepared in a wide range of particle sizes (20-1000 nm), and their particulate nature will allow them to act as truly inert light scatterers.

1.4.1 Properties of zeolites

Compositionally, zeolites are similar to clay minerals, both being aluminosilicates. They differ, however, in their crystalline structure. Many clays have a layered crystalline structure (similar to a deck of cards) and are subject to shrinking and swelling as water is absorbed and removed between the layers. In contrast, zeolites have a rigid, 3-dimensional crystalline structure (similar to a honeycomb). Their primary structure is formed by SiO_4^{4-} and AlO_4^{5-} tetrahedral sharing edges (41), and a tertiary structural network of interconnected tunnels and cavities (micropores) of molecular dimensions. For example, faujasite (zeolite Y), a common zeolite, has a cavity of 13 Å with 7 Å windows (Figure 4A, B). The lower valence of Al relative to that of Si creates excess negative charge (one per Al) that requires charge-balancing cations to maintain electroneutrality. These cations are located in the interior of the cavities and can be exchanged without disturbing the rigid framework (Figure 4C).

The porous zeolite is host to water molecules, as well as to a variety of other

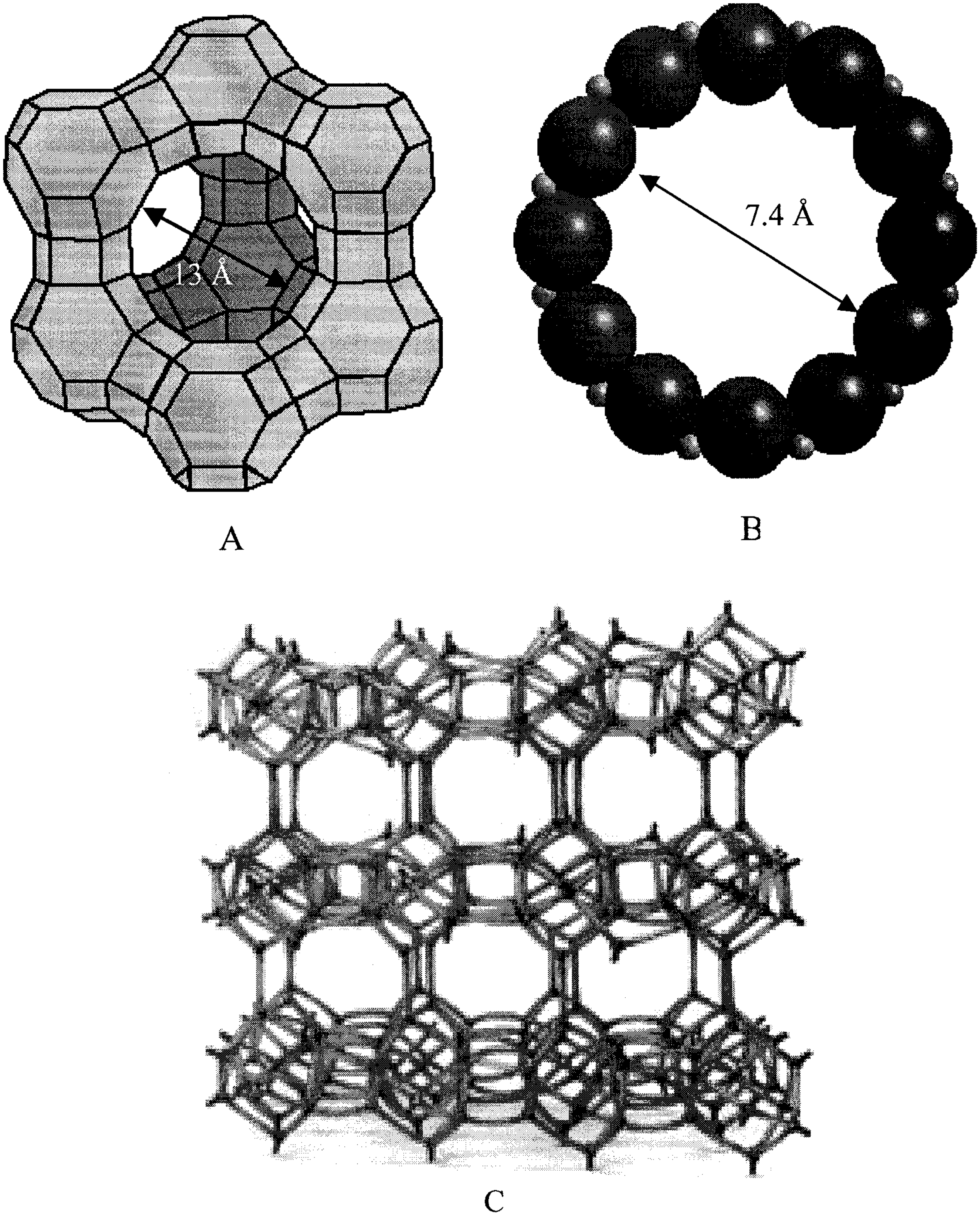

Figure 4. The structure of faujasite (A) and its window (B) (from *www.olemiss.edu/depts/chemistry/web/ellison.html*). Zeolites (C) are aluminosilicates. They have a rigid, 3-dimensional crystalline structure (similar to a honeycomb) consisting of a network of interconnected tunnels and cages whose sizes are nearly uniform (from *www.zeoponix.com/zeolite.html*).

molecules, but only those of appropriate molecular size to fit into the pores are admitted since the zeolite framework remains rigid. In fact, the pore and channel sizes are nearly uniform, allowing the crystal to act as a molecular sieve. Organic and inorganic molecules used as light absorbers can be readily encapsulated within these cavities and permanently trapped. Zeolites should alleviate any adverse side effects by preventing direct contact of their organic or inorganic guests with biological materials. Zeolites also effectively isolate molecules, and therefore the level of intermolecular interactions can be easily controlled, or totally eliminated.

Although some zeolites are natural minerals, most are synthesized by hydrothermal crystallization of mother gels. For some zeolites, it is possible to change the framework Si/Al ratio slightly, and thus the abundance of charge-balancing cations. Zeolites can be classified as small-, medium-, and large-pore, depending on the number of oxygen atoms (8, 10, or 12) defining the pore apertures. Typical zeolite particles are in the 500 – 2000 nm range, but particles as small as 20 nm can be produced. Zeolites can accommodate guests in the micropores, provided they are smaller than the pore apertures. The dimensions of the pore and the geometry of the voids control the possible guest uptake and their intercavity diffusion. These limitations to incorporation of large organic species inside a solid host of a narrow pore size distribution can be overcome since novel mesoporous aluminosilicates have been reported (42). Among them, the most widely used is MCM-41, whose internal voids are formed by parallel hexagonal channels. Silicalite is another example of a neutral (and in this case hydrophobic) zeolite.

1.4.2 Synthesis of supramolecular sunscreen

Molecules can be incorporated within zeolite cavities either through diffusional processes from the particle exterior, or through *ship-in-the-bottle* synthesis, a terminology that refers to diffusion of small precursors followed by reaction within the cavity to make the desired molecule. This strategy is particularly attractive for systems where the target molecule fits in the cavity, but it is too large to diffuse through the windows of zeolites. The example of zeolite Y mentioned above has 13 Å cavities but only 7.3 Å windows. Large molecules prepared within the cavity are permanently entrapped in the zeolite and cannot escape. This strategy has been used for photocatalysis, and should be adaptable to sunscreens.

1.5 Experimental approach

The objective of this project is to develop supramolecular sunscreens to alleviate the adverse side effects of common sunscreens on exposure to UVR. The safety and efficacy of free zeolites and zeolites with sunscreen ingredients as hosts were tested in the presence of keratinocytes and fibroblasts. The effect of UVA irradiation of cells in the presence of the composites *vs* the individual composite components was investigated. The second objective was to test the penetration, if any, of zeolite particles into cultured cells. Zeolites containing fluorescent hosts were used to probe cell penetration using laser scanning confocal microscopy. The initial choice of zeolite was NaY, a faujasite which is readily available, inexpensive and of very low acidity. Near-neutral zeolites are less likely to cause adverse effects on skin. Faujasite zeolites are usually produced in particle sizes between 500 and 1000 nm, which makes them ideal for *in vitro* studies but too large to be cosmetically acceptable. Hence, small (< 200 nm) zeolites, such as β-nanocrystalline, will have to be studied in future experiments. While fluorescent guests will not be used in actual sunscreen products, the development of zeolite-incorporated probes provides a straightforward way of establishing whether the zeolite particles bind or penetrate live cells.

1.5.1 Laser scanning confocal microscopy (LSCM)

Confocal microscopy is an established tool in many fields of biomedical research. Its major application is for improved light microscopic imaging of either fixed or living cells within fluorescently-labeled tissues. Image resolution of a conventional light microscopy is often compromised by fluorescence from outside the focal plane of interest, especially in tissues made up of multiple cell layers. In order to gain acceptable resolution, many methods are used to prepare the specimens. Nevertheless, most of the methods have the potential of introducing artifacts and therefore lead to questions about the validity of the results, especially imaging of viable cells. Confocal microscopy can improve the resolution to a theoretical maximum resolution of 0.2 μm along the optical axis. Hence, structures in the middle of a cell may be distinguished from those on the top or bottom.

The illumination in a confocal microscope is achieved by scanning one or more focused beams of light, usually from a laser, across the specimen and so the technique is called laser scanning confocal microscopy (LSCM). A laser beam is focused to a small spot by an objective lens and onto a plane within the fluorescent specimen each time. The fluorescent light from points in the specimen that are not within the focal plane (out-of-focus light) will be largely obstructed by the confocal aperture (pinhole). In this way, any out-of-focus fluorescent light (both above and below the focal plane) ray is greatly reduced. Only the fluorescent light from the focal plane (in-focus fluorescent ray) can pass through the pinhole and reach the photodetector. This feature of LSCM becomes especially important when dealing with thick specimens. The main advantage of confocal microscopy is the ability to facilitate the imaging of living cells by allowing the automated collection of three-dimensional (3D) data in the form of a Z-series. A Z-series is a sequence of optical sections collected at different planes within a specimen (Figure 5). The high resolution and capability of LSCM to generate Z-series through cells and the ability to merge the separate series into 3D images are exploited here to detect the penetration of zeolite particles into cells. By labeling the cells and the zeolite particles with different fluorochromes, the distribution profiles of the particles within the cells can be probed.

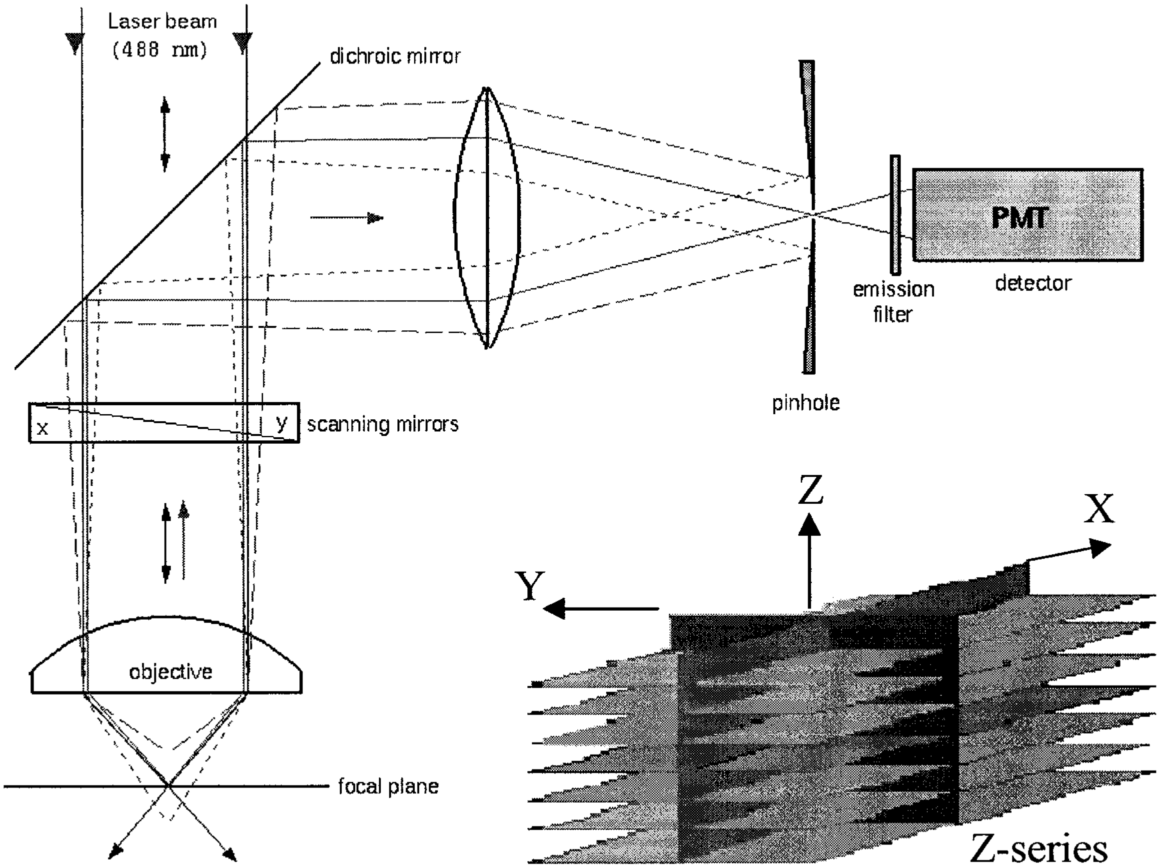

Figure 5. Laser scanning confocal microscope

—▶— In-focus light rays from laser beam

—— In-focus light rays from fluorescent probe

·········· Out-of-focus light rays from fluorescent probe

From *www.soton.ac.uk/~mfc/ confocal.html*

Materials and methods

2.1 Chemicals

Fluorescent probes cFDA, DCFH-DA, fluorescein, CMTMR were purchased from Molecular Probes. cFDA (10.9 mM) and CMTMR (9 mM) stock solutions were prepared in dimethyl sulphoxide (DMSO, BDH). DCFH-DA stock solution (14.4 mM) and fluorescein (240 μM) stock solution were prepared in ethanol (Fisher) and dimethylformamide (DFM, Aldrich), respectively. All stock solutions were stored at –20°C and diluted with saline or PBS or McIlvaine buffer (100 mM citric acid and 200 mM disodium hydrogen phosphate dihydrate, pH 4.0). $Ru(bipy)_3Cl_2$ was purchased from GFS Chemicals and 4-hydroxy-2,2,6,6-tetramethylpiperydine-1-oxyl (TEMPOL) and 2,4,6-triphenylpyrylium hydrogensulfate (TP^+) from Sigma. Stock solutions of $Ru(bipy)_3Cl_2$ (15 mg/ml), TEMPOL (290 mM), and TP^+ (11 mM) were prepared in deionized water from a Model MP-11A Mega-Pure System from Barnstead. TiO_2@NaY and fluorochrome modified zeolites, Ru@NaY, F@NaY and TP@β, were obtained from Dr. Tito Scaiano, University of Ottawa. TiO_2 (anatase) with an average particle size of 32 nm, which is comparable to that employed in sunscreens and cosmetics (14), was purchased from Alfa Aesar.

2.2 Cell cultures

Wild-type yeast *Saccharomyces cerevisiae* W303-1B from our lab was grown aerobically in rich YPD medium [2% Bacto-peptone (Difco), 1% Bacto-yeast extract (Difco), 2% D-glucose (Sigma)] on a shaker-incubator at 180 rpm at 30°C. Cells were harvested by centrifugation (453xg, 5 min, at room temperature) at the end of the exponential growth phase (~ 20 h) at a cell concentration of approximately 3×10^7 cells per ml of medium as determined with a Bright-Line counting chamber (0.1 mm depth). After removing broth, cells were washed with buffer (see Section 2.3.1).

Rat keratinocytes were purchased from American Type Culture Collection (ATCC) and human skin fibroblasts were obtained from forearm skin biopsies of normolipidemic subjects in Dr. Katherine Cianflone's lab at Royal Victoria Hospital, Montreal (43). Cells were maintained at 37°C under an atmosphere of 5% CO_2 in 100 mm cell culture dishes (Corning) containing Dulbecco's modified Eagle's medium (DMEM), which contained 100 units/ml penicillin and 0.1 mg/ml streptomycin (Sigma) and was supplemented with 5% (for use with rat keratinocytes) or 10% (for use with human skin fibroblasts) fetal calf serum (FCS, Sigma). After ~ 20 h incubation, subconfluent cells were harvested by trypsin-EDTA solution treatment, which removes cells from dishes. Harvested cells were suspended in DMEM with 5% or 10% FCS, and 1 ml cell suspensions were transferred to 4-well chamber slides (VWR). The cells were incubated at 37°C under an atmosphere of 5% CO_2 in preparation for zeolite penetration and intracellular ROS assays.

2.3 Fluorochrome staining of cells

Samples, which were stained with fluorochromes and prepared on glass or chamber slides for examination by LSCM, were transferred to a Leica microscope, equipped with ×63 and ×40 objectives and a Leica TCS SP2 confocal attachment. Three lasers, Ar/ArKr, GreNe and HeNe, were used to obtain 458, 488, 543 and 633 nm light to excite fluorescence. The fluorescence images of the samples were recorded by computer for further analysis. Samples also were imaged by differential interference contrast (DIC) microscopy, using the Leica confocal microscope.

2.3.1 cFDA, DCFH-DA and Ru(bipy)$_3^{2+}$ staining of S. cerevisiae

Yeast cells washed and resuspended in McIlvaine buffer were incubated with cFDA (43 μM) for 15 min at 40°C, and then cooled on ice for a minimum of 10 min. The suspension was analyzed with an Aminco-Bowman Series 2 spectrofluorometer using excitation and emission wavelengths of 488 and 520 nm, respectively. The stained cells were examined by LSCM to determine the distribution profile of cF within the cells. Previously, cFDA has been used as a viability probe with a variety of cells. cFDA is nonfluorescent in the acetylated form and moderately permeant to most cell membranes. Upon diffusion into cells and hydrolysis by nonspecific intracellular esterases, cFDA is converted to the fluorescent product, cF (Figure 6), which because of its extra negative charges, is better retained in cells. Thus, after staining with cFDA, fluorescence can be detected from viable cells only. The increase in cF fluorescence in whole cells is linear with the cFDA concentration since the uptake of cFDA is a simple diffusion process. To obtain an optimal signal-to-noise ratio, millimolar intracellular cF concentrations are needed, but higher cF concentrations result in quenching (44).

DCFH-DA (10 μM) was added to the yeast cell suspension in 50 mM phosphate buffered saline (PBS, pH 7.0) and incubated at 30°C for 20 min. After incubation, the cell suspensions were examined in the spectrofluorometer using excitation and emission wavelengths of 488 and 520 nm, respectively, and the stained cells were transferred to glass slides to detect the fluorescence by LSCM from DCF in the cells. DCFH-DA is a

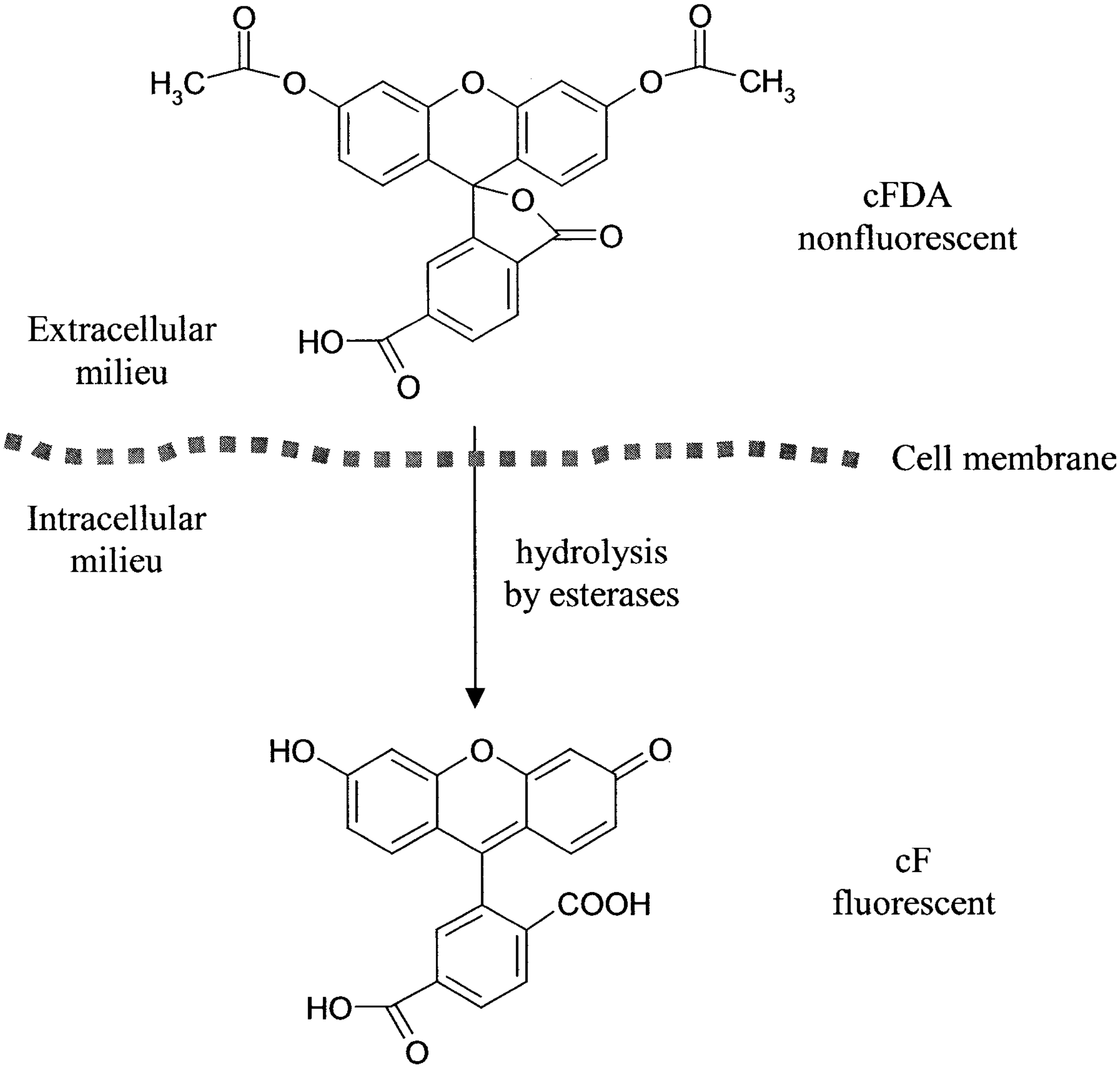

Figure 6. cFDA conversion to cF in cells

nonpolar compound that readily diffuses into cells, where it is hydrolyzed to the nonfluorescent polar derivative DCFH and thereby trapped within the cells. In the presence of an oxidant (hydrogen peroxide), DCFH is oxidized to the highly fluorescent DCF (Figure 7).

Yeast cells were incubated in deionized water or 10 mM PBS (pH 7.4) containing 200 μM $Ru(bipy)_3Cl_2$ at room temperature for 30 min. Cells were washed twice and resuspended in deionized water or PBS before analysis on the spectrofluorometer (excitation, 450 nm and emission, 610 nm). Cells were transferred onto glass slides and subjected to LSCM to detect intracellular fluorescence (excitation, 458 nm and emission, 600 - 620 nm) from $Ru(bipy)_3^{2+}$.

2.3.2 Viability of yeast under cFDA staining conditions

Conditions associated with the cFDA staining procedure (incubation at 40°C for 15 min in McIlvaine buffer at pH 4.0) may affect the viability of yeast cells. To assess the viability of *S. cerevisiae*, 1 ml of cells in YPD was added to each of four microtubes (1.5 ml). Cells in tubes 1 and 2 were washed with McIlvaine buffer twice to remove medium and resuspended in buffer only. Cells in tube 3 were washed with fresh YPD twice and resuspended in fresh YPD. Cells in tube 4 were not washed and this tube was used as the control. Following addition of cFDA to tube 1, tubes 1-3 were incubated at 40°C for 15 min. After the incubation, the steady-state fluorescence of the yeast cells in tube 1 was measured and the cells were examined by LSCM to verify that they were loaded with cFDA by monitoring cF fluorescence. To assay cell viability, 0.5 ml of cell suspension from each of the four tubes was transferred to four flasks containing 50 ml fresh YPD.

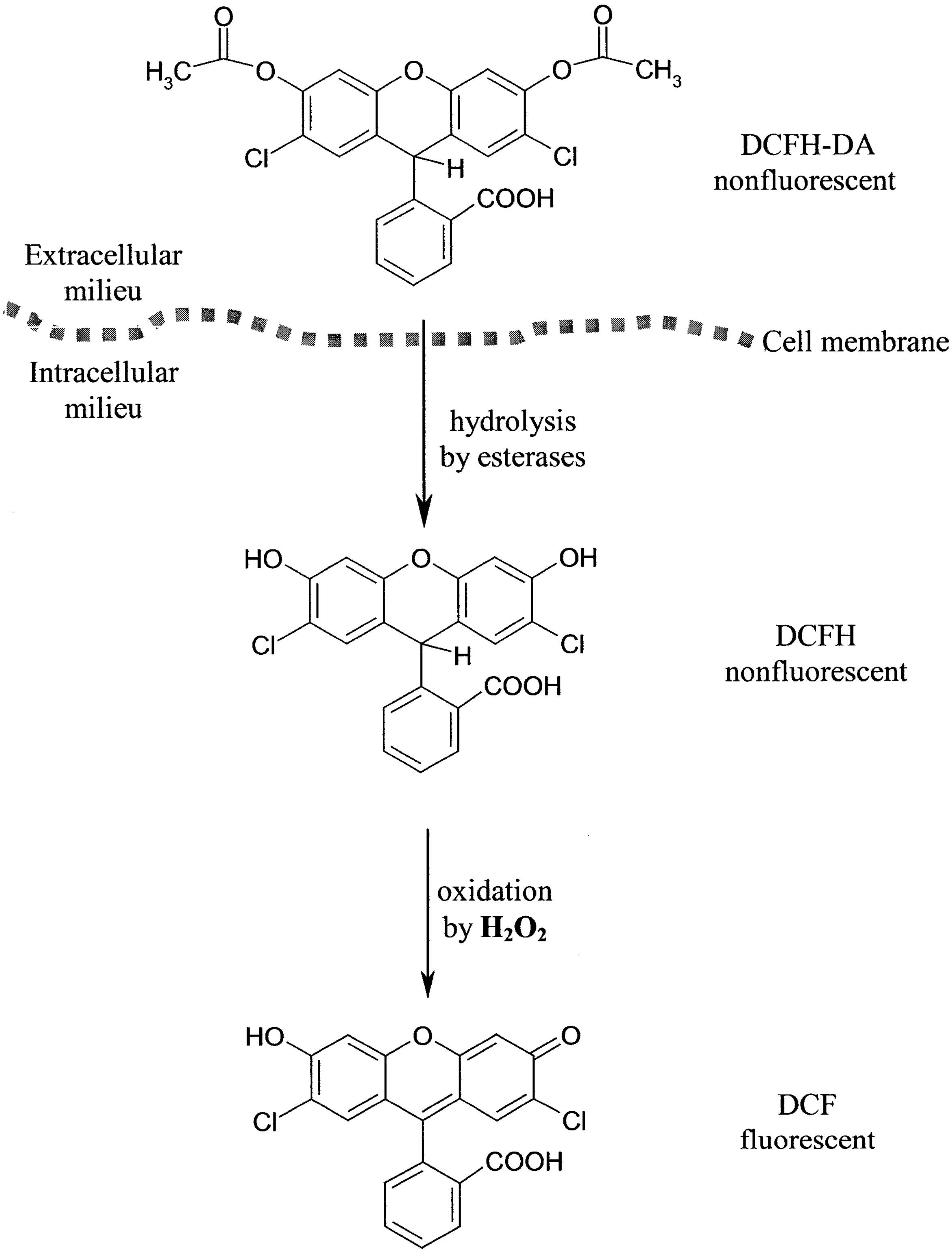

Figure 7. DCFH-DA conversion to DCF via DCFH in cells

Following 6 h incubation at 30°C with shaking at 180 rpm, 1 ml of cell suspension was removed every 8–12 h from each of the four flasks, and the absorbance was measured at 600 nm on a Beckman DU650 UV-Visible spectrophotometer. The growth curve of each culture is plotted as OD_{600} *vs* growth time.

2.3.3 Staining of mammalian cells with cFDA, DCFH-DA, $Ru(bipy)_3^{2+}$ and fluorescein

Rat keratinocytes and human skin fibroblasts grown on chamber slides were washed twice with 0.9% saline. The cells then were incubated in saline containing 40 μM cFDA or 10 μM CFDH-DA at room temperature for 4 min, and the intracellular fluorescence from cF or DCF was examined by LSCM.

For staining with $Ru(bipy)_3^{2+}$ and fluorescein, the washed cells were incubated for 25 min on chamber slides in saline with 40 μM $Ru(bipy)_3^{2+}$ at room temperature or in saline with 2 μM fluorescein at 37°C. The cells were washed twice with saline to remove the extracellular fluorochromes, and intracellular fluorescence from $Ru(bipy)_3^{2+}$ (excitation, 458 nm; emission, 600 – 620 nm) and fluorescein (excitation, 488 nm; emission, 510 - 520 nm) was detected by LSCM.

2.4 Release of guests from probe-modified zeolites

Ru@NaY, F@NaY and TP@β were used to probe the release of guests from modified zeolites. The zeolites were suspended in 0.9% saline (~1 mg/ml) and sonicated at room temperature for 15 min on Fisher FS30H sonicator. The supernatants were removed after centrifugation at 35,064xg for 5 min. Except Ru@NaY and TP@β, F@NaY was washed with saline twice to remove any remaining fluorochromes and resuspended in saline. The steady-state fluorescence of the modified zeolite suspensions and the supernatants were measured following excitation at 450 nm for $Ru(bipy)_3^{2+}$ and fluorescein, and 420 nm for TP^+. The emission was set at 610, 550 and 500 nm for $Ru(bipy)_3^{2+}$, fluorescein and TP^+, respectively. The fluorescence of free $Ru(bipy)_3^{2+}$ (200 μM), fluorescein (2.4 μM) and TP^+ (110 μM) solutions was measured before and after centrifugation as controls using the same excitation and emission setting as for the modified zeolites.

2.5 Sample irradiation

UVA irradiation of samples was performed in a photoreactor, model LZC- ICH2 from Luzchem Research (Ottawa), which was equipped with a power meter to measure irradiation intensity. To calculate the light intensity in mW/cm^2, the power meter was set to the 2000 FC scale and the intensity was calculated from:

$$\text{intensity in mW/cm}^2 = \text{meter reading} \times \text{calibration factor}$$

The calibration factor used for our instrument was 0.0277. Four 350-nm Luzchem UVA lamps were placed in the ceiling of the light chamber. The total UVA irradiation received by each sample was 1.7-2.0 mW/cm^2. A turntable was used to ensure homogeneous irradiation. Non-irradiated controls were foil-covered and placed in the light chamber so that all samples were treated identically except for UVA exposure. The temperature of the light chamber was maintained at 25 ± 1°C. Cultured cells in each well of chamber slides were covered with 1 ml HBSS when exposed to UVA irradiation. HBSS is permeable to UVA light.

2.6 Cell penetration of modified zeolite particles

After ~ 20 h incubation, the medium surrounding the cultured cells in the chamber slides was removed and new DMEM medium containing 30 μg/ml sonicated fluorochrome-modified-zeolite (Ru@NaY and F@NaY) was added to the cells at various times. DMEM with FCS was used for dividing cells and serum-free DMEM was used for growth-arrested cells. The cells on chamber slides were exposed to the modified-zeolite suspensions at 37°C under an atmosphere of 5% CO_2. After different times of exposure to the modified zeolites, the cells were washed twice with 0.9% saline and incubated at room temperature in saline containing cFDA (40 μM) for 5 min or CMTMR (4.5 μM) for 15 min. Cell penetration of the modified zeolite particles was probed by LSCM by selecting appropriate excitation and emission wavelengths (cFDA/Ru@NaY pair: excitation 488 nm; emission 510-530 and 600-620 nm; CMTMR/F@NaY pair: excitation 543 and 488 nm; emission 560 - 580 and 510 - 530 nm).

2.7 Assay of intracellular H_2O_2

Intracellular H_2O_2 production was measured by the method of Bass *et al.* (45) as modified for LSCM by Ohba *et al.* (46). Briefly, chamber slides containing confluent cells, to which TiO_2, NaY, NaY plus TiO_2 (NaY+TiO_2) and TiO_2-encapsulated NaY (TiO_2@NaY) suspensions were added, were exposed to UVA for different times and washed twice with HBSS. The washed cells were incubated at room temperature for 5 min in HBSS containing 22 μM DCFH-DA (45). Intracellular ROS generation was detected by LSCM following oxidation of DCFH to DCF (Figure 7). DCFH photooxidation were minimized by collecting the fluorescent image with a single rapid scan (line average, 4; total scan time, 4.33 s) and identical parameters, such as contrast and brightness, for all samples. The cells were also imaged by DIC microscopy. All images were collected using a 512 × 512 pixel format. Five to seven groups of 20±3 clearly defined cells were selected from the images in the DIC channels for each sample to quantify the fluorescence. Well defined cells were selected since it is possible to measure all of the intensity from these cells. The intensity of the fluorescence in single cells was quantified (using Leica software) for each group of 20 cells, and the relative fluorescence intensity per cell was obtained from the average of ~100 cells per sample using the untreated control cells as a reference (100% intensity). All experiments were repeated three times.

TEMPOL is a stable nitroxide radical, which is capable of scavenging free radicals and mimics superoxide dismutase (SOD) activity. Unlike SOD, TEMPOL readily penetrates cell membranes providing intracellular protection against free radicals (47, 48). Furthermore, it is water soluble and can be added directly to the culture medium. In this study, we investigated the ability of TEMPOL to protect against UVA-induced H_2O_2 generation *in vitro* in human skin fibroblasts and to confirm the oxidation of DCFH by H_2O_2 in cells. Before cells were exposed to UVA irradiation, the medium was removed and fresh DMEM containing 5 mM TEMPOL was added to the chamber slides for 15 min. During UVA irradiation, DMEM-containing TEMPOL was replaced by HBSS-containing TEMPOL (5 mM). Control cells were incubated with HBSS only. After UVA irradiation, cells were examined by LSCM to determine the effect of TEMPOL on DCFH oxidation. Since TEMPOL does not absorb above 320 nm, it will not absorb the UVA irradiation (320 – 400 nm) produced in light chamber.

Results

3.1 Uptake of free fluorochromes by cells

3.1.1 S. cerevisiae loading with cFDA, DCFH-DA and $Ru(bipy)_3^{2+}$

The uptake of selected fluorescent probes by viable cells was first tested in yeast. After yeast cells were incubated with the fluorescent probes, the steady-state fluorescence of the cell suspensions was measured on a spectrofluorometer. Figure 8 shows the fluorescence spectra of yeast cells loaded with three fluorescent probes. Figure 8A reveals that McIlvaine buffer, the buffer plus cFDA and the cell suspension are nonfluorescent. However, the fluorescence of a cell suspension plus cFDA is high, revealing that cFDA is converted to fluorescent cF in cells (Figure 6). Furthermore, the fluorescence intensity of the supernatant is much lower than that of cFDA-loaded yeast suspension (Figure 8A), indicating that cF was trapped in the cells and did not escape during the 15-min incubation period.

Like cFDA, after DCFH-DA is taken up by viable cells, its DCF derivative will fluoresce (Figure 7). The fluorescence intensity of PBS, DCFH-DA in PBS and the yeast cell suspension was low while that of the yeast cells plus DCFH-DA was high (Figure 8B). These results indicate that nonfluorescent DCFH-DA penetrates into yeast cells and is converted to fluorescent DCF (Figure 7). The fluorescence of DCFH-DA in PBS should be the same as that of buffer alone, but its intensity was found to be higher than that of buffer (Figure 8B). Fresh solutions of DCFH-DA in PBS were less fluorescent than old solutions (not shown), indicating that DCFH-DA may be oxidized to DCF by impurities in the buffer. Figure 8B shows that the cell suspension plus DCFH-DA

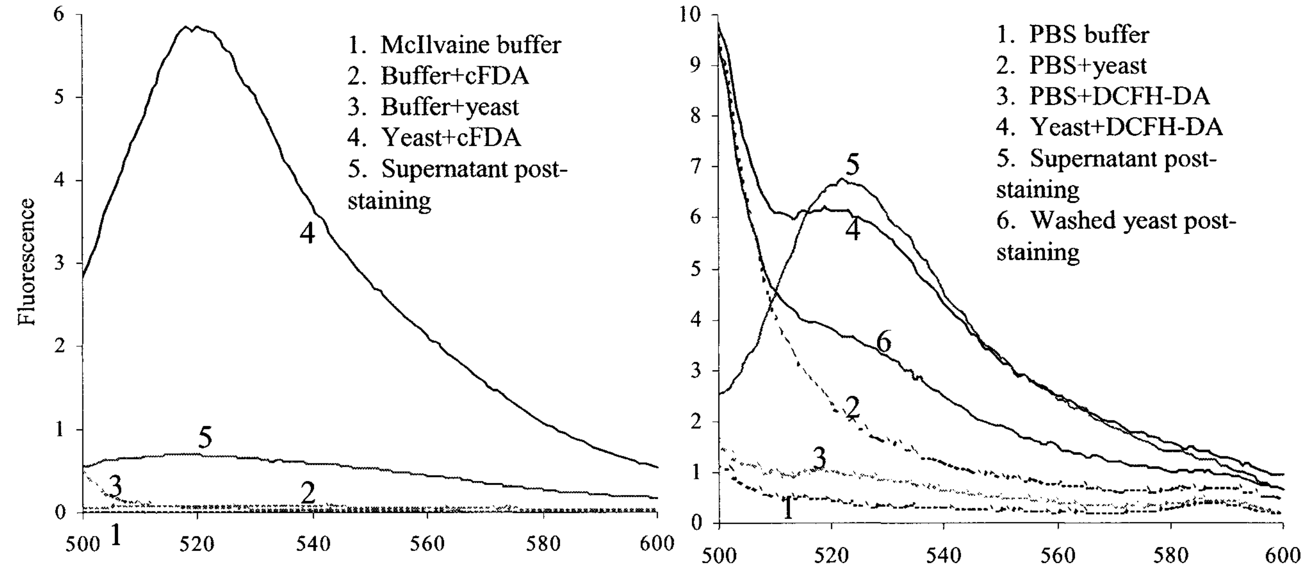

(A) cFDA (Ex 490nm)

(B) DCFH-DA (Ex 490nm)

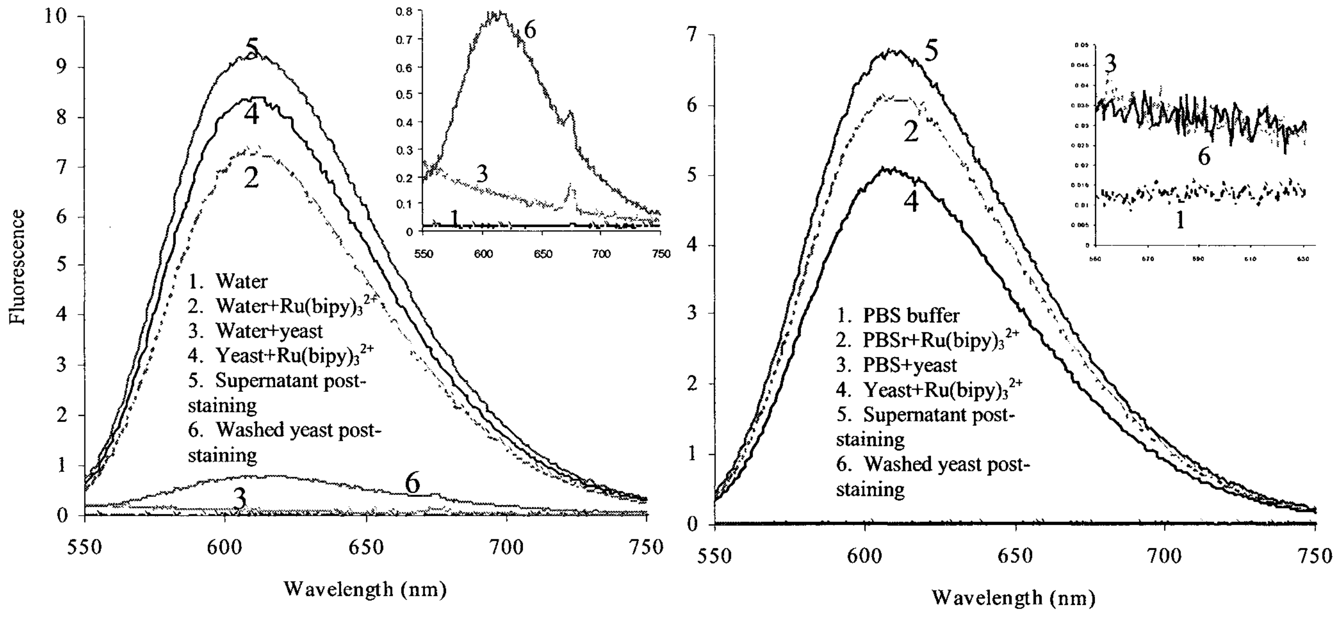

(C) Ru(bipy)$_3^{2+}$ (water, Ex 450nm)

(D) Ru(bipy)$_3^{2+}$ (PBS, Ex 450nm)

Figure 8. Steady-state fluorescence of yeast cells loaded with fluorochromes. Cells were incubated in McIlvaine buffer (pH 4.0) at 40°C for 15 min for cFDA-loading, in PBS (pH 7.0) at 30°C for 20 min for DCFH-DA-loading, and in PBS (pH 7.4) or deionized water at room temperature for 30 min for Ru(bipy)$_3^{2+}$-loading.

(spectrum 4) was less fluorescent than the supernatant (spectrum 5) post-staining. After washing with PBS, the cell suspension (spectrum 6) is less fluorescent than before (spectrum 4), indicating that DCF leaked out of the cells into buffer.

Yeast cells were also loaded with $Ru(bipy)_3Cl_2$ in PBS and deionized water. Because $Ru(bipy)_3^{2+}$ itself fluoresces, steady-state fluorescence measurement cannot differentiate between extra- and intracellular $Ru(bipy)_3^{2+}$. After incubation in PBS or water containing $Ru(bipy)_3^{2+}$, the yeast cells were washed twice and resuspended in PBS or water. The inserts of Figure 8 C *vs* D show that the fluorescence intensity of yeast stained in water is clearly higher than that of yeast stained in PBS. These results suggest that $Ru(bipy)_3^{2+}$ penetrates into yeast cells when stained in deionized water but not in PBS. LSCM was used next to confirm the penetration of $Ru(bipy)_3^{2+}$ and the other probes into yeast cells.

As mentioned in Section 1.5.1, LSCM can focus on different planes within cells. Hence, it is possible to detect the penetration of fluorochromes into cells by using confocal microscopy. Figure 9A shows the fluorescence of cF, converted from cFDA in yeast cells. LSCM focuses on one plane at a time, and different planes are detected in a group of cells. Figure 9B shows the DIC image, which confirms that the observed fluorescence comes from the yeast cells. By performing a wavelength scan, the emission spectrum can be obtained, and compared with that of the free probe to verify that the fluorescence from the cells is that of the probe. The emission spectra using the LSCM wavelength scan and the spectrofluorometer are similar (Figure 9C), which verifies that the fluorescence from the cells is due to cF excitation. A Z-series of fluorescence images were taken at ~0.2 μm intervals (minimum) within the cells from top to bottom (Figure 10). Using the LSCM software to color the images based on fluorescence intensity

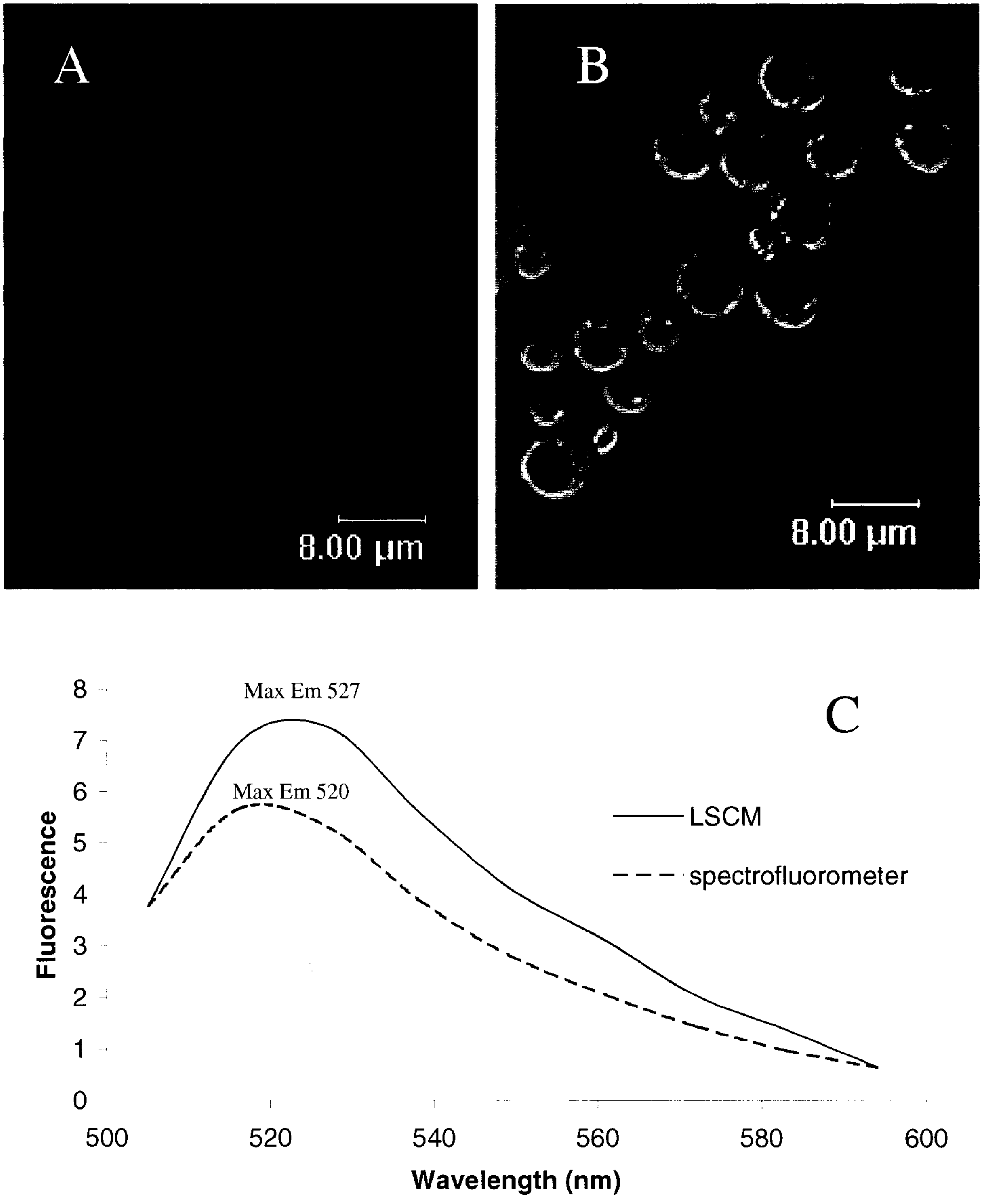

Figure 9. LSCM analysis of yeast cells loaded with cFDA. (A) Fluorescence at ~520 nm from cF in yeast cells following excitation at 488 nm; (B) DIC image of yeast cells; (C) overlay of the emission recorded by LSCM and with the spectrofluorometer.

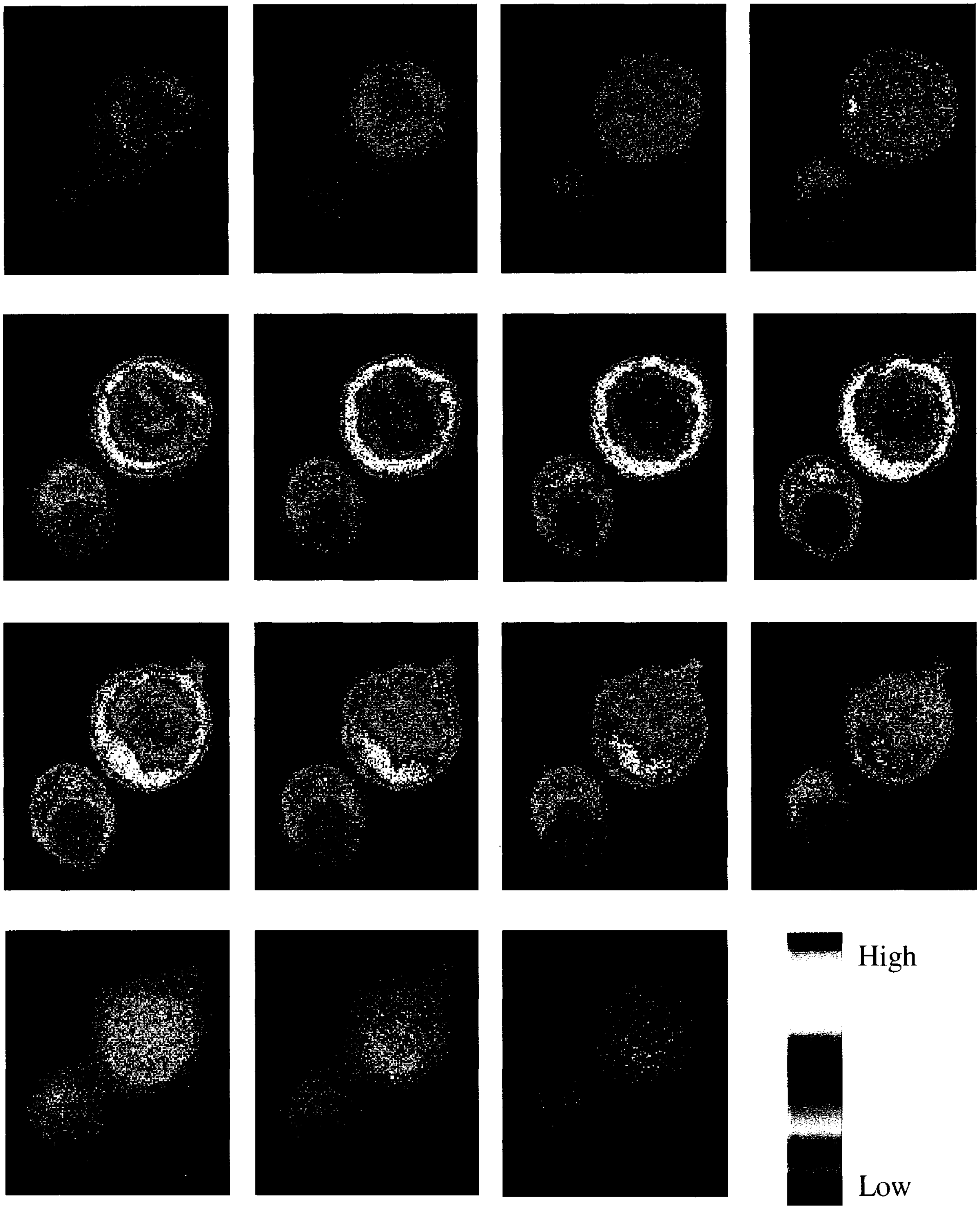

Figure 10. Computer-treated Z-series images of cFDA-loaded yeast cells. The fluorescence intensity is represented by the variation in color (see color bar) and demonstrates the distribution profile of the fluorochrome within the yeast cells after 15 min exposure to 43 μM cFDA.

indicates the distribution of cF in the cells (Figure 10). A 3D video (not given here) based on the Z-series images clearly demonstrated the penetration of cF into the yeast cells as well as its distribution profile. Thus, the LSCM results confirm those obtained using steady-state fluorescence, which suggested that cFDA penetrated into the yeast cells and was converted to fluorescent cF.

Yeast cells loaded with DCFH-DA also were examined by LSCM to confirm the cell penetration of DCFH-DA. The fluorescence from DCF, formed from DCFH-DA within cells, was detected (Figure 11A) and the DIC image (Figure 11B) confirms the presence of the cells. The emission spectra obtained by LSCM and using the spectofluorometer (Figure 11C) are similar in shape and indicate that the detected fluorescence was from DCF in the cells. Z-series images and a 3D video of the images (not shown) further confirmed that DCFH-DA penetrated into yeast cells and was converted to fluorescent DCF in cells.

The penetration of $Ru(bipy)_3^{2+}$ into yeast cells suspended in PBS buffer and deionized water also was tested by LSCM. Because $Ru(bipy)_3^{2+}$ itself fluoresces, stained cells were washed and resuspended in buffer or water to remove extracellular $Ru(bipy)_3^{2+}$. No fluorescence was observed from yeast cells suspended in PBS buffer containing $Ru(bipy)_3^{2+}$ (Figure 12A), and the DIC image (Figure 12B) confirms that the cells were scanned. However, when the yeast cells were stained with $Ru(bipy)_3^{2+}$ in deionized water, fluorescence was observed (Figure 12C). The similarity of the emission spectra recorded by LSCM and on the spectrofluorometer confirms that the fluorescence is from $Ru(bipy)_3^{2+}$ (Figure 12D). A Z-series scan was performed, and the 3D video of the

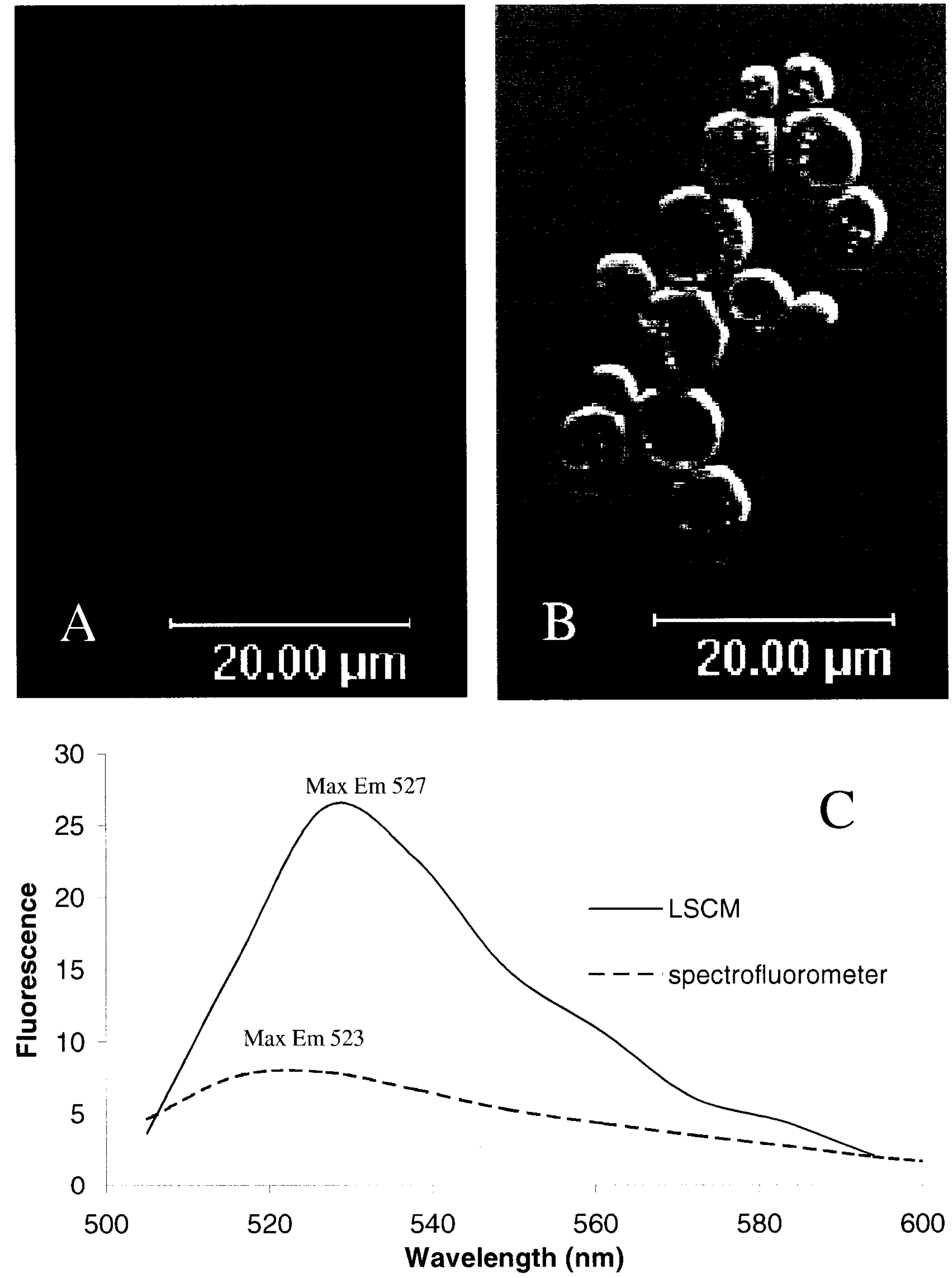

Figure 11. LSCM analysis of yeast cells loaded with DCFH-DA. (A) Fluorescence at ~520 nm from DCF in yeast cells following excitation of 488 nm; (B) DIC image of yeast cells; (C) overlay of the emission recorded by LSCM and with the spectrofluorometer. Cells were exposed to 10 μM DCFH-DA for 20 min.

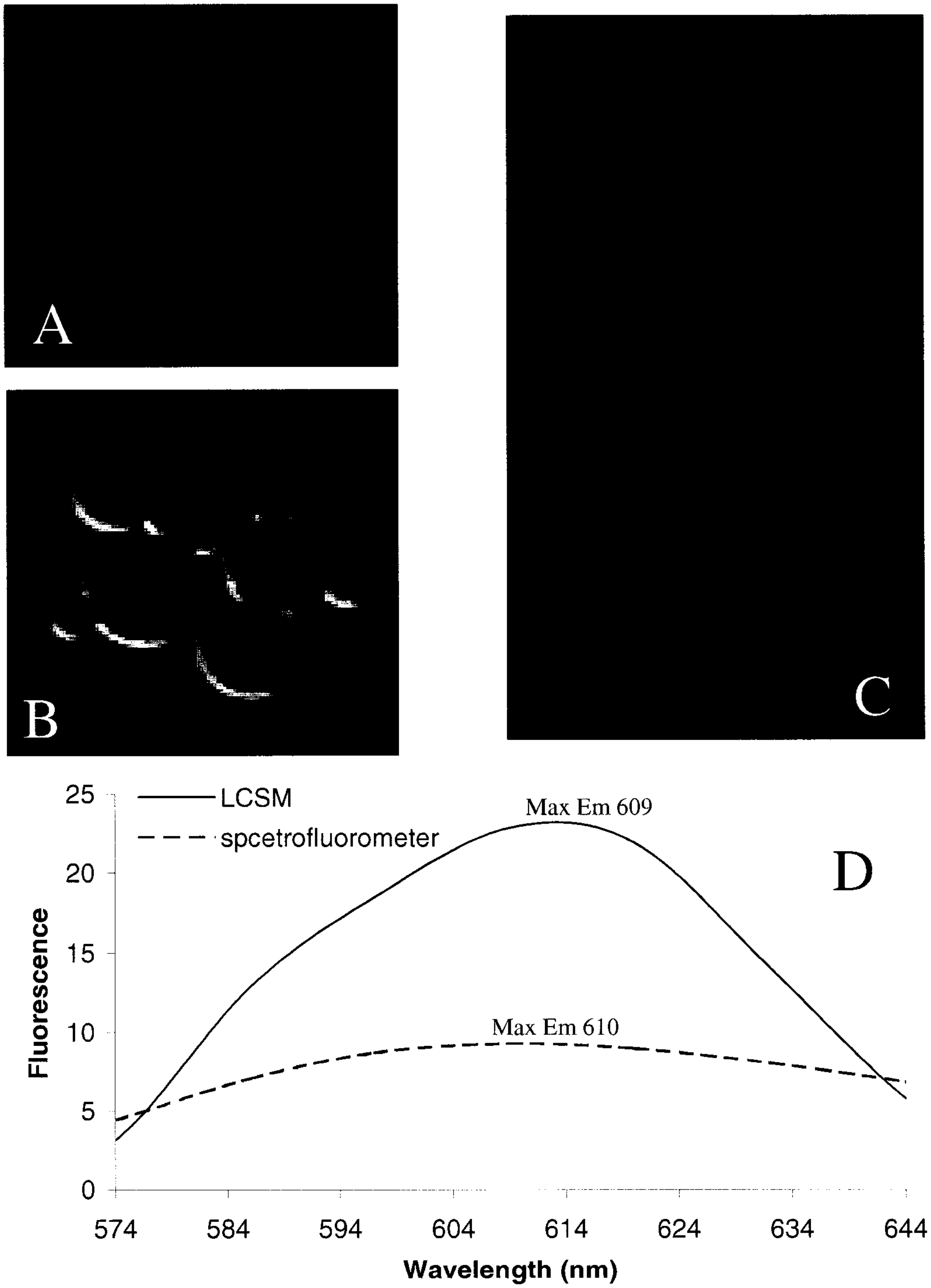

Figure 12. . LSCM analysis of yeast cells loaded with Ru(bipy)$_3^{2+}$. (A) Fluorescence at ~610 nm from Ru(bipy)$_3^{2+}$ following excitation at 456 nm is not observed in yeast cells suspended in PBS; (B) DIC image of the yeast cells; (C) fluorescence at ~610 nm from Ru(bipy)$_3^{2+}$ in cells suspended in deionized water; (D) overlay of the emission recorded by LSCM and with the spectrofluorometer. Cells were exposed to 200 µM Ru(bipy)$_3^{2+}$ for 30 min

images confirms that $Ru(bipy)_3^{2+}$ penetrated into yeast cells suspended in deionized water.

Live cells autofluoresce when excited at certain wavelengths. Thus, untreated yeast cells were examined by LSCM under the same conditions used to monitor probe fluorescence. No autofluorescence was observed (Figure 13 A, C), confirming that the fluorescence detected was from the probes.

3.1.2 Viability of yeast cells after staining with cFDA

Because they were loaded with cFDA under conditions that may cause cell death (pH 4.0 buffer, at 40°C for 15 min), the viability of yeast cells after staining was examined. Two suspensions in McIlvaine buffer (tubes 1 and 2), one of which contained cFDA (tube 1), and the third suspension in fresh YPD medium (tube 3) were incubated at 40°C for 15 min. The original suspension (tube 4), which was incubated at 30°C, was used as the control. Fluorescence from cF in the cells in tube 1 was observed using the spectrofluorometer and LSCM (Figure 14A, B), and confirmed that cFDA penetrated the cells. Four flasks, containing 50 ml fresh YPD each and 0.5 ml cell suspension each from tubes 1-4, were incubated on a shaker (30°C, 180 rmp). At 8-12 h interval, the OD_{600} of the cell suspensions in the flasks was measured and growth curves were constructed for each sample (Figure 14C). Since the growth curves of three treated samples are the same as that of untreated control, the viability of yeast is not affected by the cFDA-loading conditions, which was confirmed by staining with Trypan Blue. This vital stain penetrates the plasma membranes of dead cells but not viable cells, so that dead cells are stained blue and viable cells remain colorless. Few blue cells were detected in the treated and

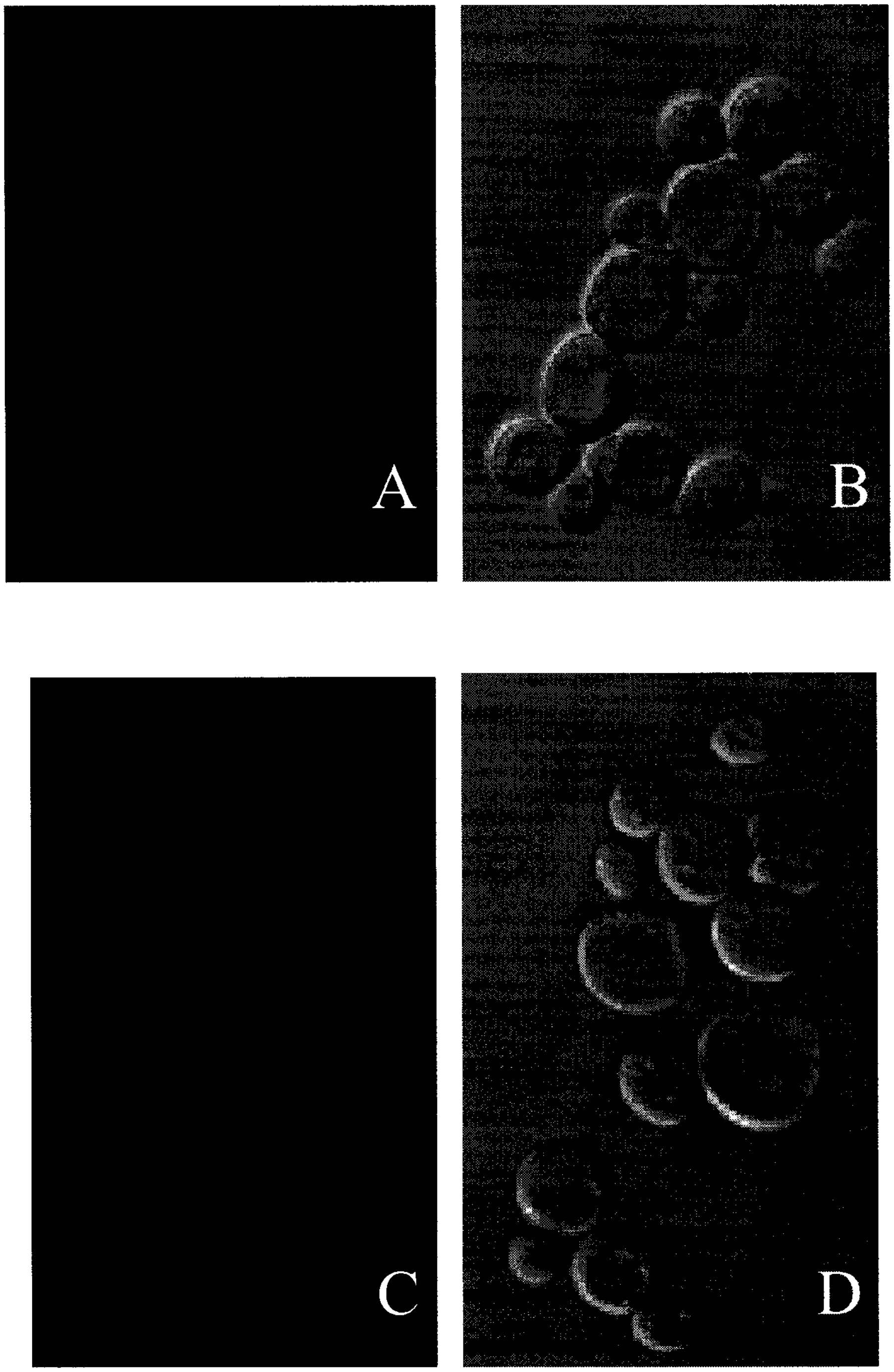

Figure 13. No autofluorescence from yeast cells excited at (A) 458 nm and (C) 488 nm; (B) and (D) are DIC images of cells

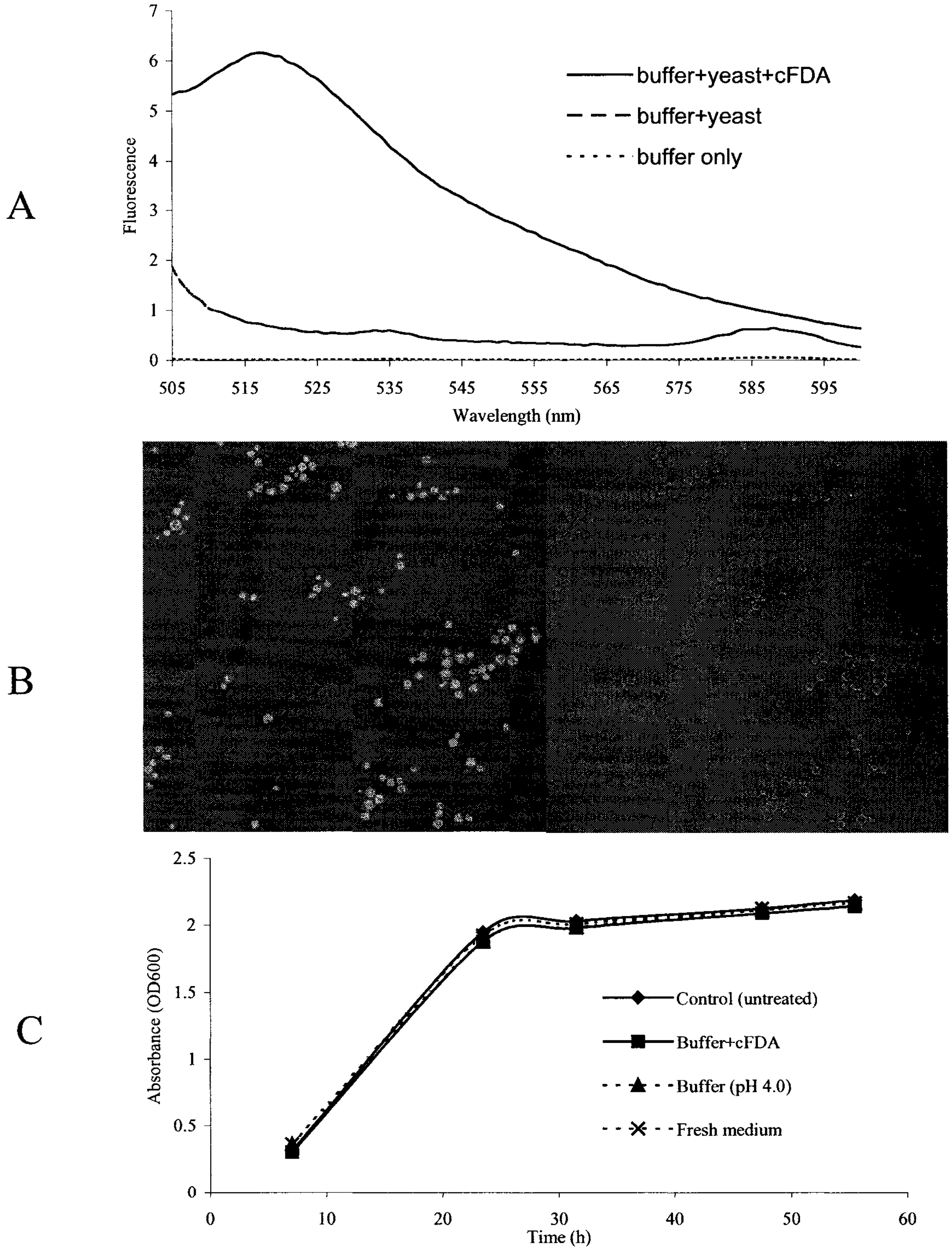

Figure 14. Viability of yeast cells under cFDA staining conditions. Yeast was washed and resuspended in different solutions and exposed to the cFDA staining conditions (15 min at 40°C in pH 4.0 buffer). (A) Fluorescence spectra of cFDA-treated yeast; (B) fluorescence (left) and DIC (right) images of yeast loaded with cFDA; (C) growth curve of yeast in YPD following exposure to the cFDA staining conditions. The control cells were from the original cell suspension in YPD.

control samples (data not shown), revealing the same level of viability, consistent with the growth curve results.

3.1.3 Rat keratinocytes loading with cFDA, DCFH-DA, fluorescein and Ru(bipy)$_3^{2+}$

Following the procedures used for the yeast cells, the penetration of the free fluorochromes into cultured rat keratinocytes was examined. Rat keratinocytes were stained with the probes in 0.9% saline on chamber slides and examined by LSCM. Figure 15 shows the fluorescence from cells loaded with cFDA. The results are consistent with cFDA penetration into cells and its convertion to cF. A DIC image of the cells was taken at the same time (Figure 15) to confirm that the fluorescence arises from the cells and not the background. A wavelength scan, a Z-series scan and a 3D video (not shown) were recorded and confirmed that the fluorescence is from cF in the rat keratinocytes. Fluorescence from DCF (derived from DCFH-DA) in the cells also was detected (Figure 15), and the DIC image of the cells recorded. Analysis of the wavelength scan, Z-series scan and 3D video (not shown) of the loaded cells confirmed that the fluorescence was from DCF in the keratinocytes.

Only weak fluorescence was detected from fluorescein-stained (excitation, 488 nm; emission, 510-530 nm) rat keratinocytes in 0.9% saline (Figure 15). The cells were also stained in PBS (pH7.4), and the results (not shown) were the same as those in 0.9% saline. This suggests that only a little fluorescein penetrates into rat keratinocytes or that it rapidly leaks from the cells.

No fluorescence was observed by LSCM (excitation, 488 nm; emission, 600-620 nm) from rat keratinocytes loaded with Ru(bipy)$_3^{2+}$ in 0.9% saline on chamber slides. DIC

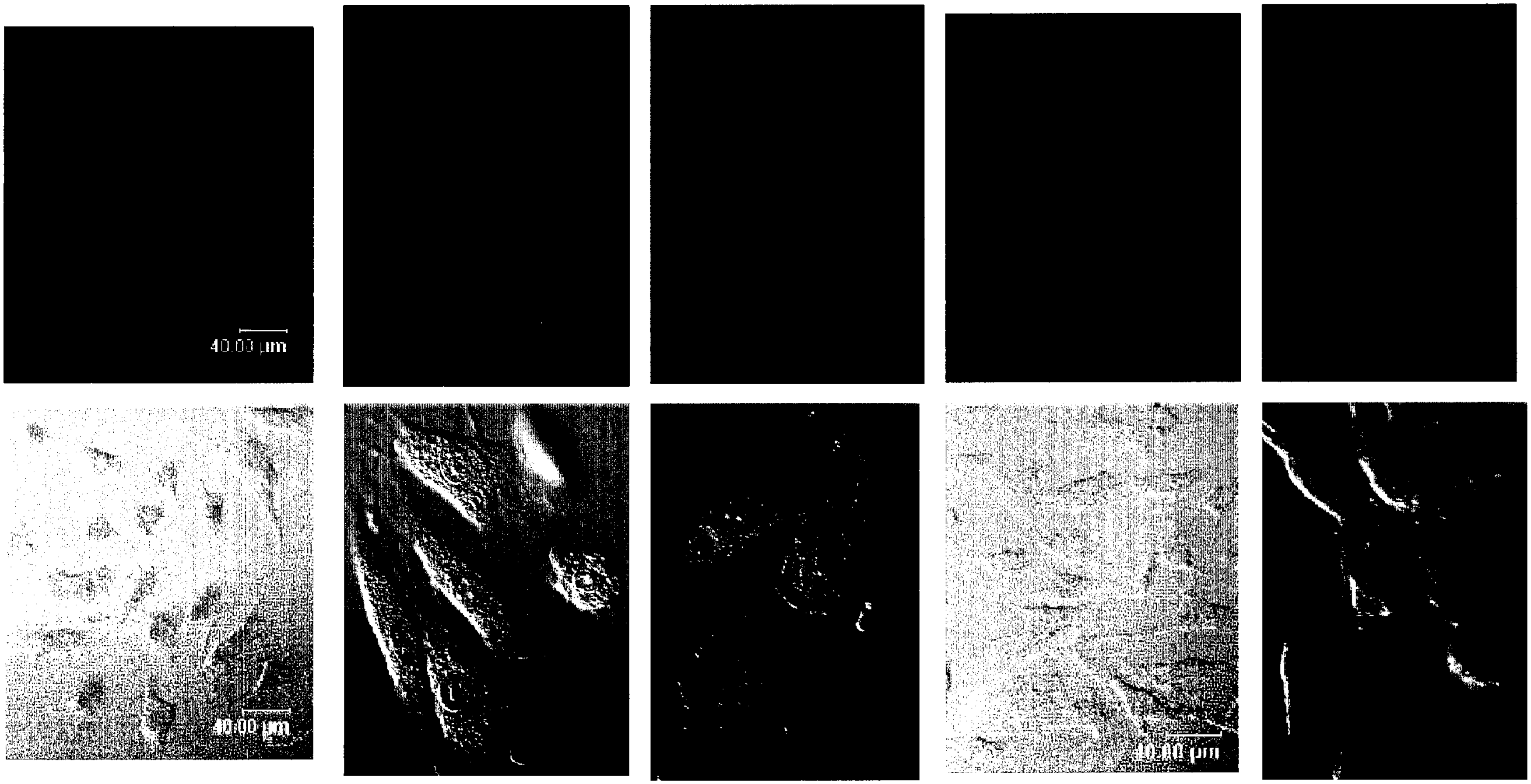

CFDA
(em ~520 nm)

DCFH-DA
(em ~520 nm)

$Ru(bipy)_3^{2+}$
(em ~610 nm)

Fluorescein
(em ~515 nm)

Autofluorescence

Figure 15. LSCM analysis of rat keratinocytes loaded with fluorochromes. Cells were loaded in 0.9% saline at room temperature for 4 min (40 µM cFDA and 10 µM DCFH-DA) or 25 min [40 µM $Ru(bipy)_3Cl_2$ and 2 µM fluorescein). Upper panels are the fluorescence images and autofluorescence on excitation at 488 nm and lower panels are DIC images of the same samples. $Ru(bipy)_3^{2+}$ was also excited at 458 nm but no fluorescence was detected (not shown).

images were recorded at same time to verify that the cells were present on the slides (Figure 15). Because the excitation maximum of $Ru(bipy)_3^{2+}$ is 450 nm, the 458 nm line of the Argon laser also was used to excite the cells, but no fluorescence was observed (not shown). A Z-series scan was performed to detect fluorescence from different planes within the cells, but again no fluorescence was detected, indicating that $Ru(bipy)_3^{2+}$ did not penetrate into the rat keratinocytes in 0.9% saline.

The autofluorescence (excitation, 488 nm) of rat ketatinocytes was examined to verify that the observed fluorescence was from the probes. No autofluorescence (Figure 15) was detected under the conditions used to examine the penetration of the probes into the rat cells. DIC images confirm that the cells were present. In summary, the results reveal that cFDA and DCFH-DA stain rat keratinocytes in 0.9% saline, fluorescein stains weakly, and $Ru(bipy)_3^{2+}$ does not stain the cells.

3.1.4 Human skin fibroblasts loading with cFDA, DCFH-DA, fluorescein and $Ru(bipy)_3^{2+}$

Penetration of the fluorescent probes into human skin fibroblasts also was examined by LSCM. The cells were stained in 0.9% saline on chamber slides and examined by LSCM. Fluorescence from cF and DCF was observed (Figure 16) by LSCM and the penetration of the probes into the cells was verified by performing wavelength and Z-series scans (not shown). Unlike the rat keratinocytes, strong fluorescence from fluorescein was detected in the fibroblasts (Figure 16) and confirmed by wavelength and Z-series scans. However, no fluorescence from $Ru(bipy)_3^{2+}$ was detected in the fibroblasts (Figure 16) and the cells did not autofluoresce on excitation at 488 nm. The

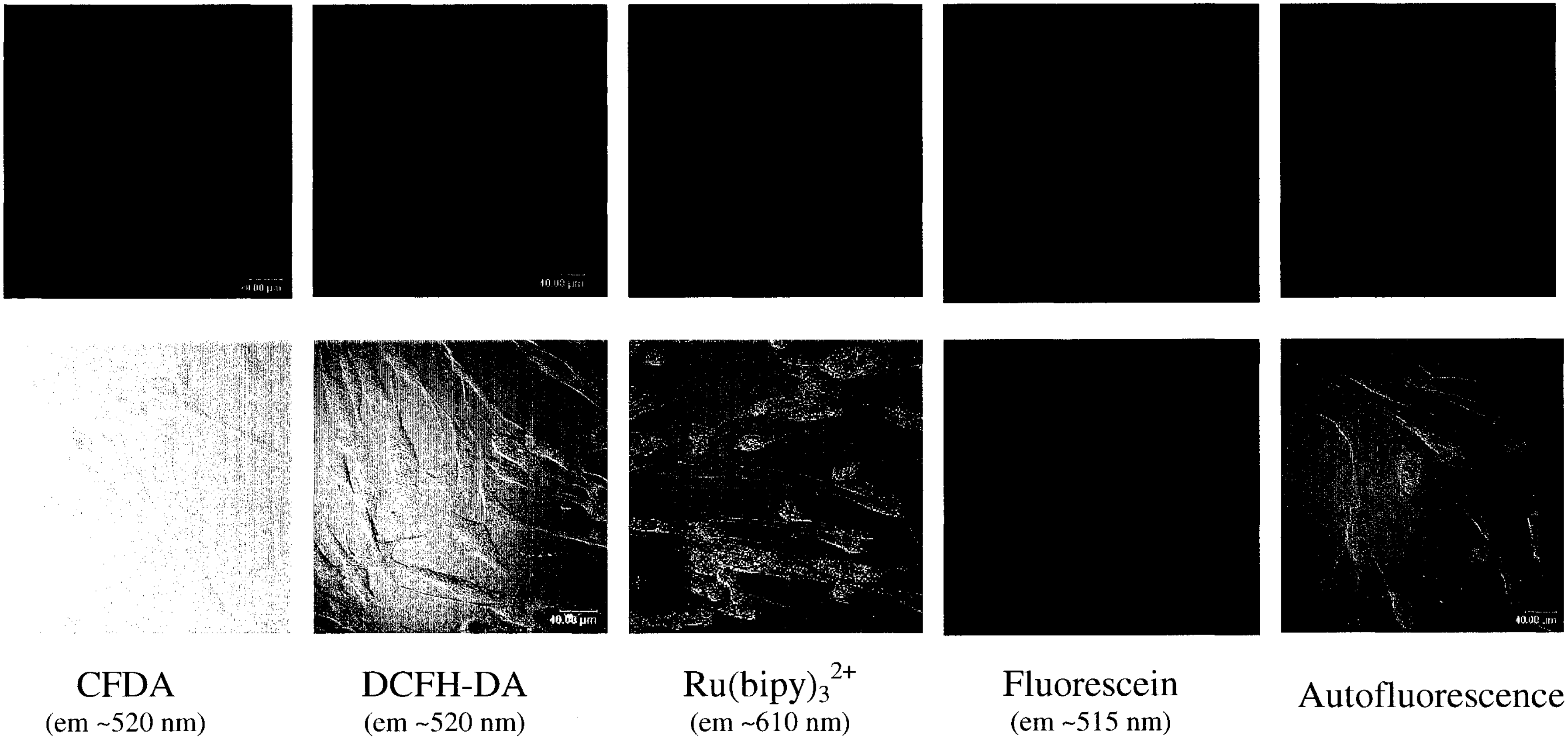

CFDA
(em ~520 nm)

DCFH-DA
(em ~520 nm)

$Ru(bipy)_3^{2+}$
(em ~610 nm)

Fluorescein
(em ~515 nm)

Autofluorescence

Figure 16. LSCM analysis of human skin fibroblasts loaded with fluorochromes. Cells were loaded in 0.9% saline at room temperature for 4 min (40 µM cFDA and 10 µM DCFH-DA) or 25 min [40 µM $Ru(bipy)_3Cl_2$ and 2 µM fluorescein]. Upper panels are the fluorescence images and autofluorescence on excitation at 488 nm and lower panels are DIC images of the same samples. $Ru(bipy)_3^{2+}$ was also excited at 458 nm but no fluorescence was detected (not shown).

combined results show that cFDA, DCFH-DA and fluoresein penetrate into human skin fibroblasts in 0.9% saline but Ru(bipy)$_3^{2+}$ does not.

3.2 Cell penetration of the fluorochrome-modified zeolites

3.2.1 Examination of escape of the fluorescent probes from the zeolites

Three fluorescent-probe-modified zeolite samples were provided by our collaborators at the University of Ottawa. The fluorescent probes were encapsulated in the cavities of the zeolites, and these fluorescent zeolites were used to examine by LSCM the cell penetration of the zeolites. However, before testing cell penetration, escape of the probes from the zeolite cavities had to be examined. The modified zeolites were suspended in 0.9% saline, the solution used to examine cell penetration, and escape of the probes was monitored by steady-state fluorescence.

The fluorescence of an Ru@NaY suspension was measured just after it was prepared. The suspension was subjected to centrifugation at 35,064xg for 5 min, and the fluorescence of supernatant and the resuspended pellet were measured. The fluorescence intensities of the initial Ru@NaY suspension and the suspension reformed after centrifugation were almost the same. Also, the fluorescence intensity of the supernatant was very low (Figure 17A), indicating that Ru(bipy)$_3^{2+}$ did not escape from the faujasite at this time point (0 h). Another sample of Ru@NaY was left standing in 0.9% saline at room temperature for 24 h and the fluorescence measurements were repeated. The fluorescence intensities of the Ru@NaY suspension and resuspension also were very close, and that of the supernatant was very low (Figure 17B). These results indicate that Ru(bipy)$_3^{2+}$ did not escape from the faujasite over 24 h. A solution containing free

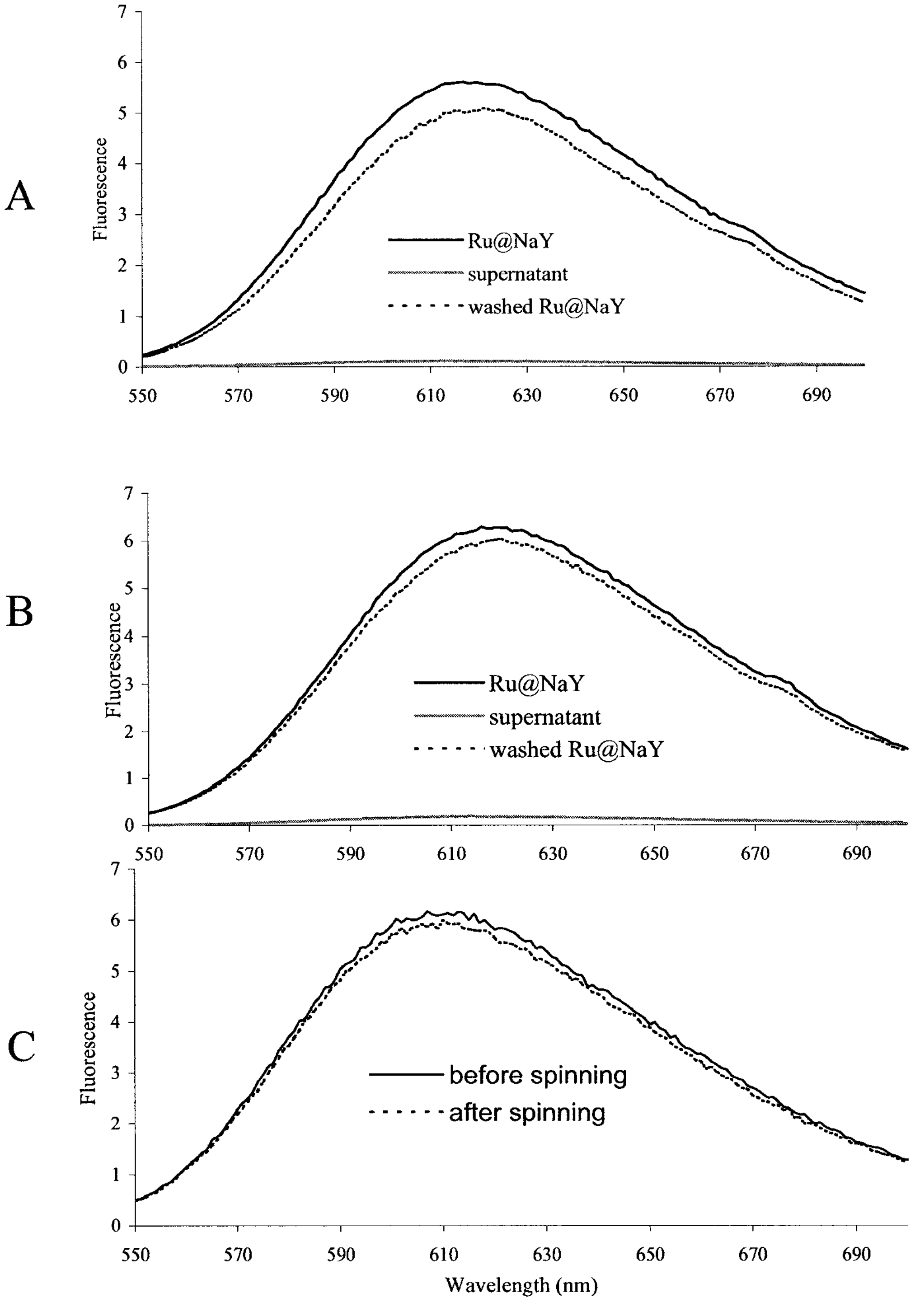

Figure 17. Emission spectra of Ru@NaY suspensions and supernatants in 0.9% saline. (A) Spectra recorded just after preparation (0 h) of an Ru@NaY suspension; (B) spectra recorded 24 h after preparation; (C) spectra of free Ru(bipy)$_3$Cl$_2$ before and after centrifugation. All experiments were performed at room temperature (excitation 450 nm and slits 4 nm). The concentration of suspension was ~ 1 mg/ml and that of free Ru(bipy)$_3$Cl$_2$ was 0.15 mg/ml (200 μM).

$Ru(bipy)_3^{2+}$ also was centrifuged at 35,064xg for 5 min and the fluorescence measured before and after centrifugation to insure that free $Ru(bipy)_3^{2+}$ did not precipitate under the centrifugation conditions. The results verified that free $Ru(bipy)_3^{2+}$ did not precipitate (Figure 17C), although the fluorescence intensity measured before and after centrifugation was slightly different, which may be caused by the high $Ru(bipy)_3^{2+}$ concentration used.

TP@β was examined using the same procedure. The fluorescence intensity of a TP@β suspension and resuspension were very close and that of the supernatant was very low. A 24 h suspension gave the same results as a 0 h suspension (Figure 18A, B), demonstrating that TP^+ was trapped in the cavities of the β-nanocrystalline zeolite. The fluorescence of a free TP^+ solution also was measured before and after centrifugation and the results showed that free probe did not precipitate under the centrifugation conditions (Figure 18C).

Unlike Ru@NaY and TP@β, the supernatant of F@NaY was highly fluorescent and the F@NaY resuspension was less fluorescent than the original suspension (Figure 19A). Did fluorescein molecules escape from the cavities of faujasite or just from its surface? When F@NaY was washed with saline twice, the fluorescence intensity of the third supernatant was close to zero (Figure 19A). The washed F@NaY was held at room temperature for 24 h and the fluorescence measurements were repeated. As the spectra show (Figure 19B), the fluorescence intensity of supernatant remained very low, suggesting that fluorescein does not escape from the cavities of faujasite. The high fluorescence intensity of the supernatant of non-washed F@NaY was caused by fluorescein molecules on the surface of the faujasite particles. The fluorescence intensity

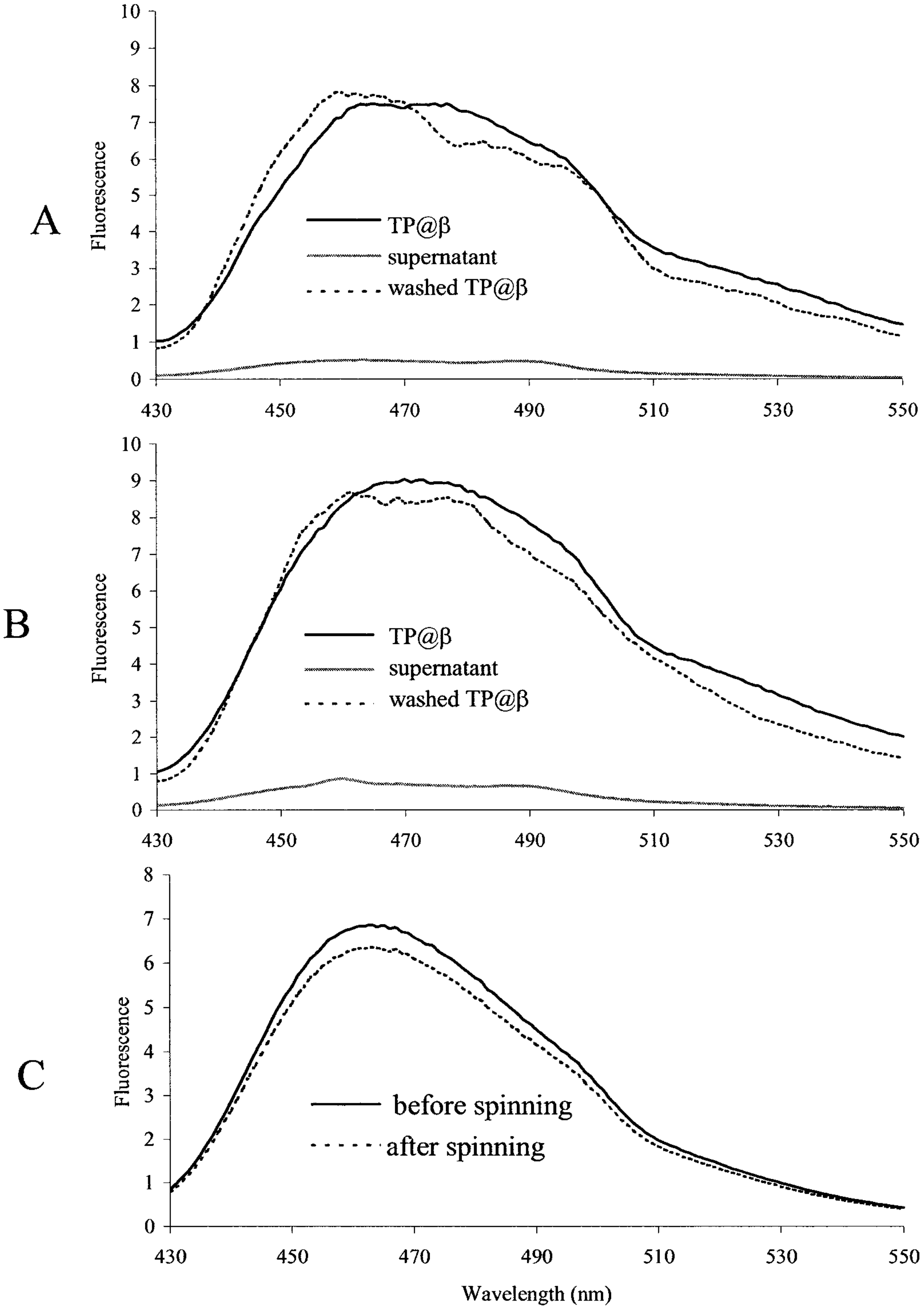

Figure 18. Emission spectra of TP@β suspensions and supernatants in 0.9% saline. (A) Spectra recorded just after preparation (0 h) of a TP@β suspension; (B) spectra recorded 24 h after preparation; (C) spectra of free TP before and after centrifugation. All experiments were performed at room temperature (excitation 420 nm and slits 4 nm). The concentration of the TP@β suspension was ~ 1 mg/ml and that of free TP was 45 µg/ml (110 µm).

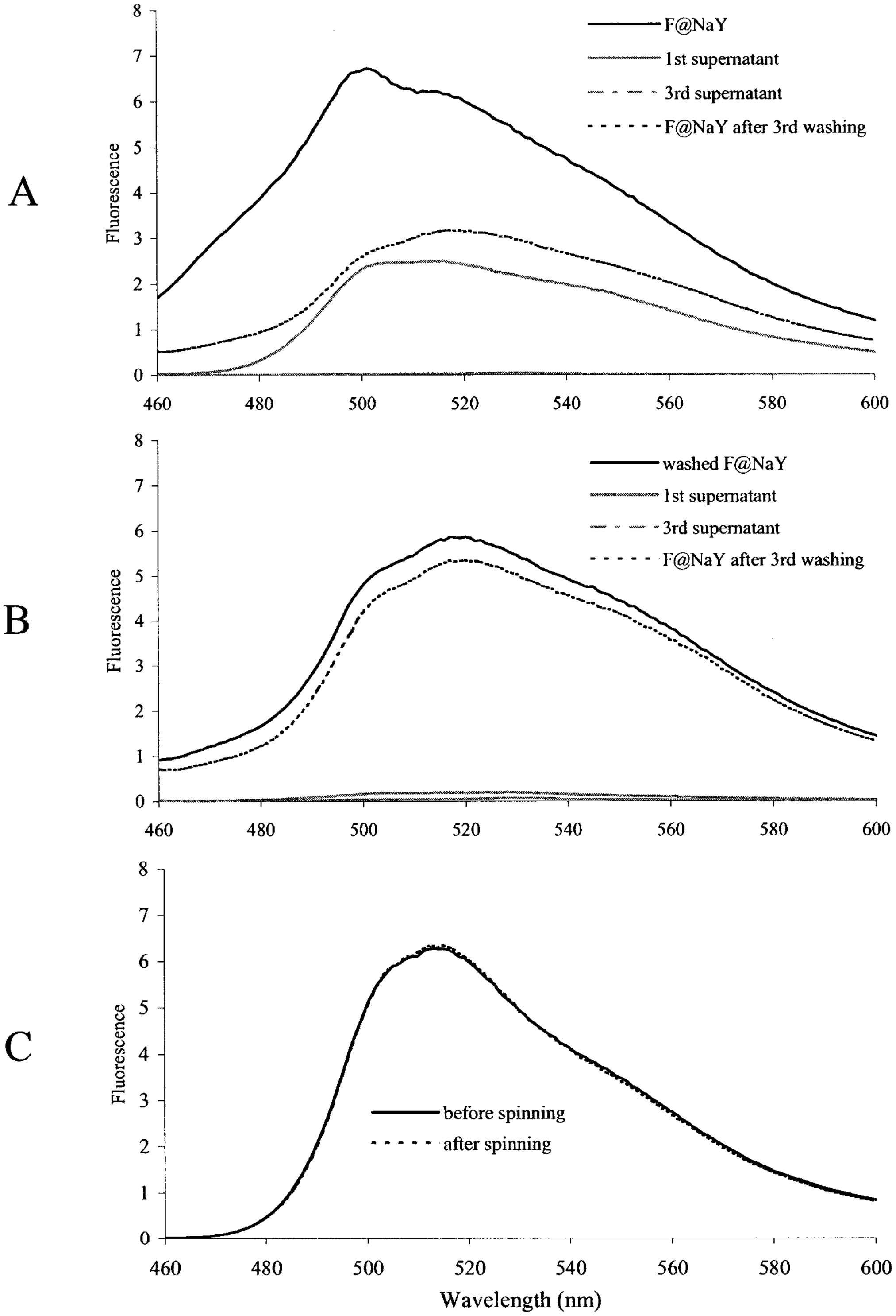

Figure 19. Emission spectra of F@NaY suspensions and supernatants in 0.9% saline. (A) Spectra recorded just after preparation (0 h) of a F@NaY suspension; (B) spectra recorded 24 h after preparation; (C) spectra of free fluorescein before and after centrifugation. All experiments were performed at room temperature (excitation 450 nm and slits 4 nm). The concentration of suspension was ~ 1 mg/ml and that of free fluorescein was 0.8 µg/ml (2.4 µm).

of free fluorescein was also measured before and after centrifugation and the results verified that free fluorescein does not precipitate during centrifugation (Figure 19C).

In summary, the fluorochromes encapsulated in zeolites are trapped in the cavities and cannot escape.

3.2.2 Counterstains for examining zeolite cell penetration

To image cells by fluorescence LSCM, they must be stained by fluorochromes. As tested above, rat keratinocytes and human skin fibroblasts can be stained with cFDA and DCFH-DA and their derivatives (cF and DCF) emit around 520 nm (excitation, 488 nm). Since $Ru(bipy)_3^{2+}$ emits around 610 nm (excitation, 488 nm), cFDA and DCFH-DA should be ideal counterstains for Ru@NaY. Therefore, cFDA was selected because of its higher retention by the cells, and the penetration of Ru@NaY into rat keratinocytes was tested. Figure 20 showed the fluorescence images within a single plane recorded by LSCM following excitation at 488 nm. Image A shows the fluorescence (emission 600-620 nm) from $Ru(bipy)_3^{2+}$ encapsulated in faujasite, while image B shows the fluorescence (emission 510-530 nm) from cF in cells. Using these different emission wavelength settings, fluorescence from the modified zeolites or the cells can be detected by LSCM. In image A, only the red fluorescence from Ru@NaY is observed whereas the green fluorescence of cF in the cells is seen in image B. Since the emission maxima of Ru@NaY and cF do not overlap (Figure 21), and there is negligible overlap within the detection ranges selected (600-610 and 510-530 nm), cFDA is a good counterstain to test cell penetration of Ru@NaY by LSCM (Figure 20C).

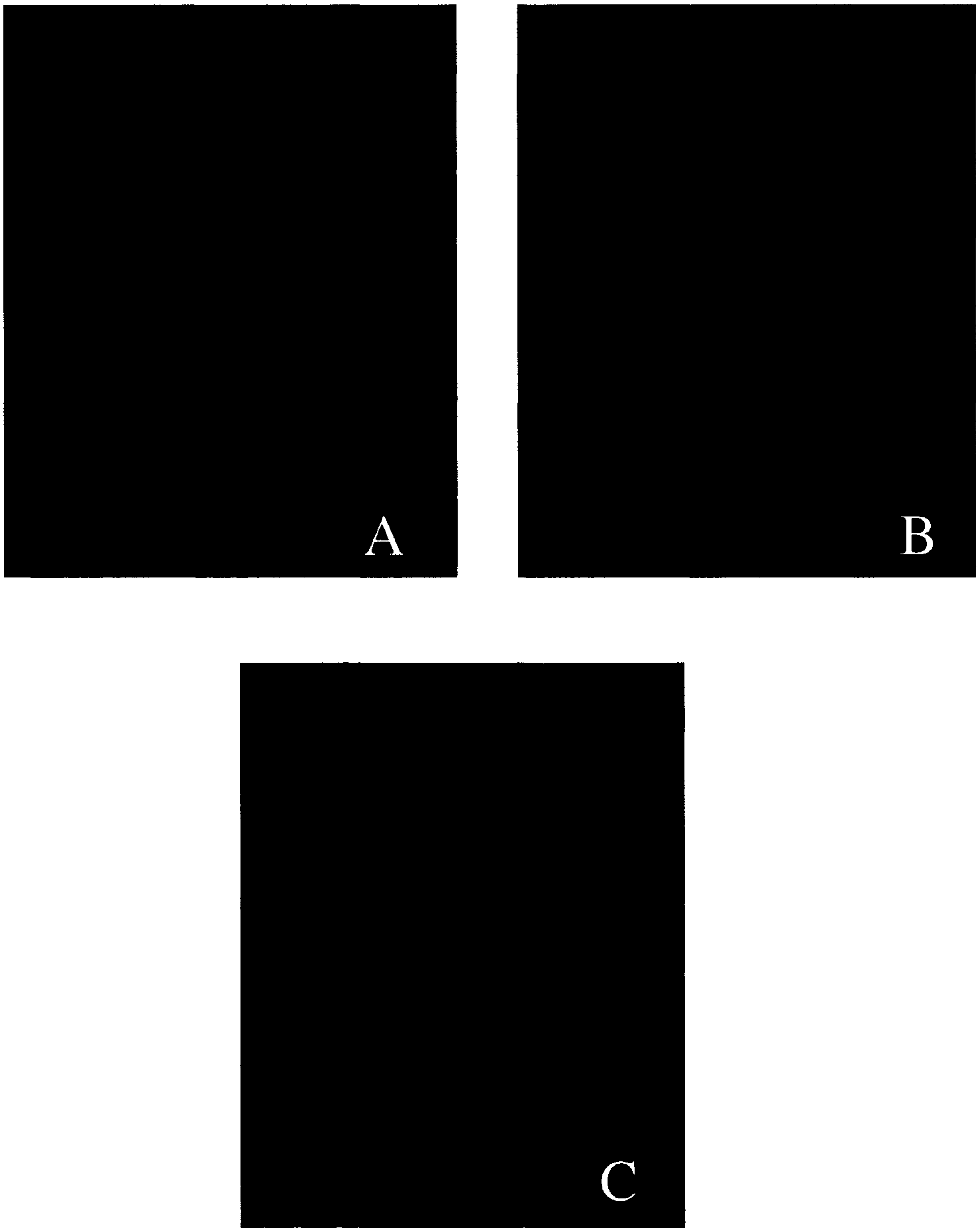

Figure 20. cFDA as a counterstain to test Ru@NaY penetration into rat keratinocytes. Subconfluent cells in 0.9% saline were incubated with 30 μg/ml of Ru@NaY for ~20 min on chamber slides, stained with cFDA, and excited at 488 nm under LSCM. (A) Fluorescence from Ru@NaY (em ~610 nm); (B) fluorescence from free cFDA (em ~520 nm); (C) overlay of image A and B in the same plane.

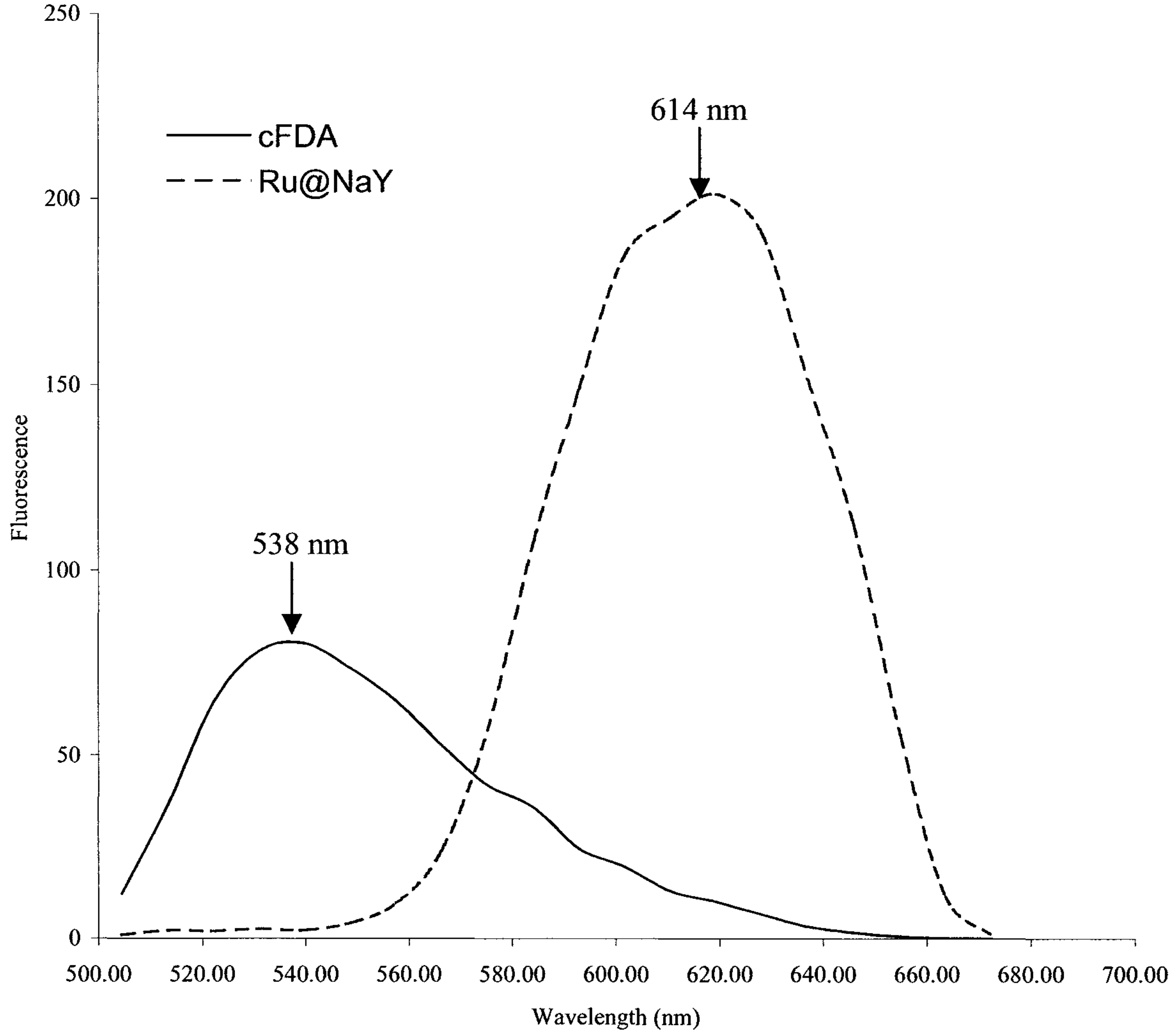

Figure 21. LSCM emission spectra of cFDA-stained keratinocytes exposed to Ru@NaY. The emission maxima of cF and Ru@NaY are well separated. The experimental conditions are given in the caption to Figure 20.

Neither cFDA nor DCFH-DA is an ideal counterstain for F@NaY because the emission maximum of the modified zeolite is ~ 520 nm. Therefore, other probes had to be examined as counterstains for F@NaY. With excitation and emission maxima at 540 and ~ 570 nm, respectively, CMTMR was tested as a counterstain for F@NaY. In Figure 22, image A shows that only CMTMR emission (565-575 nm) was observed following excitation of the cells at 543 nm, and image B reveals that only F@NaY emission (510-520 nm) is detected on excitation at 488 nm. Since the fluorescence from the two probes does not overlap (Figure 22C), CMTMR is a good counterstain for F@NaY.

After exposure to Ru@NaY or F@NaY for 20 min in saline on chamber slides, rat keratinocytes were stained with cFDA or CMTMR and examined by LSCM. Overlaying image A and B (Figure 20C), the distribution profile of Ru@NaY in the cells should be observed. However, image C revealed that Ru@NaY did not penetrate into the cells but particles adhered to their surface. A Z-series scan was performed and confirmed that there is no cell penetration of Ru@NaY (not shown). No cell penetration of F@NaY was detected (Figure 22C) under the same conditions. In summary, NaY does not penetrate into rat keratinocytes when cells are exposed to the zeolite in 0.9% saline for a short period (~ 20 min). Does penetration occur when cells are exposed for longer times to NaY in DMEM, which is close to their natural growth environment?

3.2.3 Probing cell penetration of the modified zeolites at longer times

After growth on chamber slides for ~ 20 h, cells were added to fresh DMEM with or without FCS. In serum-free DMEM, cells cannot divide but remain viable, whereas cells in DMEM containing FCS can divide and reproduce. Modified zeolites were added

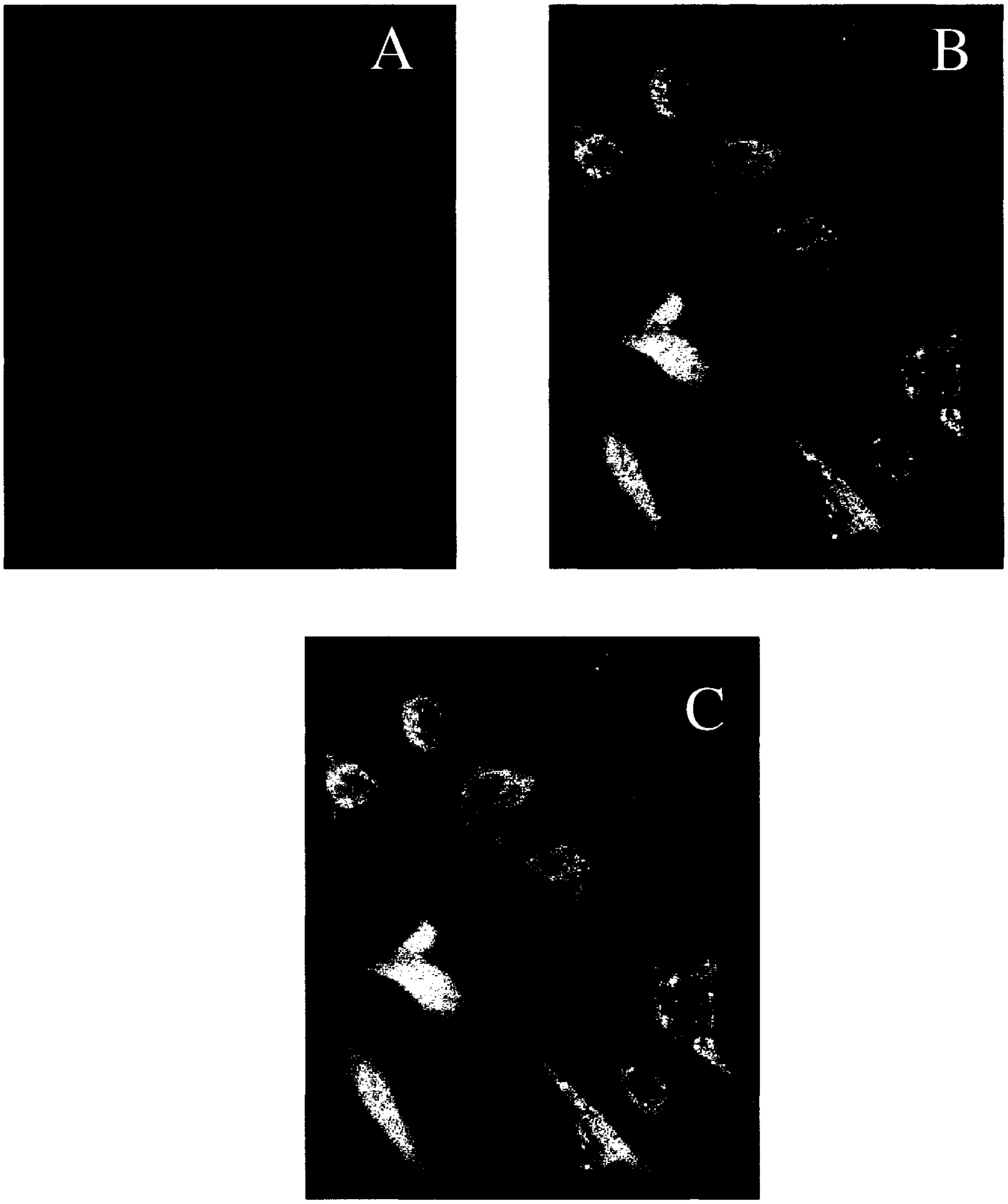

Figure 22. CMTMR as a counterstain to test F@NaY penetration into rat keratinocytes. Subconfluent cells in 0.9% saline were incubated with 30 μg/ml of F@NaY for ~20 min on chamber slides, stained with CMTMR, and excited under LSCM. (A) fluorescence from F@NaY (ex 488 nm, em ~520 nm); (B) Fluorescence from CMTMR (ex 543 nm, em ~570 nm); (C) overlay of image A and B in same plane.

to the cells at different times, the cells were washed with 0.9% saline twice and incubated with cFDA for 4 min at room temperature. Figure 23 shows the images of growth-arrested rat keratinocytes exposed to Ru@NaY for 1, 4 and 30 h. Upper panels show fluorescence from a single plane within the cells and the lower panels show the overlay of the fluorescence and DIC images. The Ru@NaY particles aggregated on the surface of the rat keratinocytes, as can be seen clearly from the overlaid images (Figure 23, lower panels). There was no penetration of Ru@NaY into cells since there is no Ru@NaY fluorescence from within the cells in Figure 23, although the particles accumulated at several places on the surface of the cells. Z-series scans were performed and the results are consistent with Ru@NaY aggregation on the surface but no cell penetration after exposure up to 30 h. The same experiments were repeated for dividing rat keratinocytes, with the same results. The images in Figure 24 show Ru@NaY particles aggregated on the surface of dividing rat keratinocytes but no cell penetration. Thus, Ru@NaY did not penetrate into either dividing or growth-arrested rat keratinocytes even after 30 h incubation in DMEM.

The time course of cell penetration of $Ru(bipy)_3^{2+}$-modified zeolites was also tested with both dividing and growth-arrested human skin fibroblasts. Even after 27 h exposure to Ru@NaY, no penetration of the zeolite into the fibroblasts was observed. The Ru@NaY particles aggregated on the surface of the fibroblasts (Figure 25, 26), and a Z-series scan and 3D video (not shown) confirm the results. Thus, Ru@NaY did not penetrate into either rat keratinocytes or human skin fibroblasts after long exposure times (30 and 27 h, respectively).

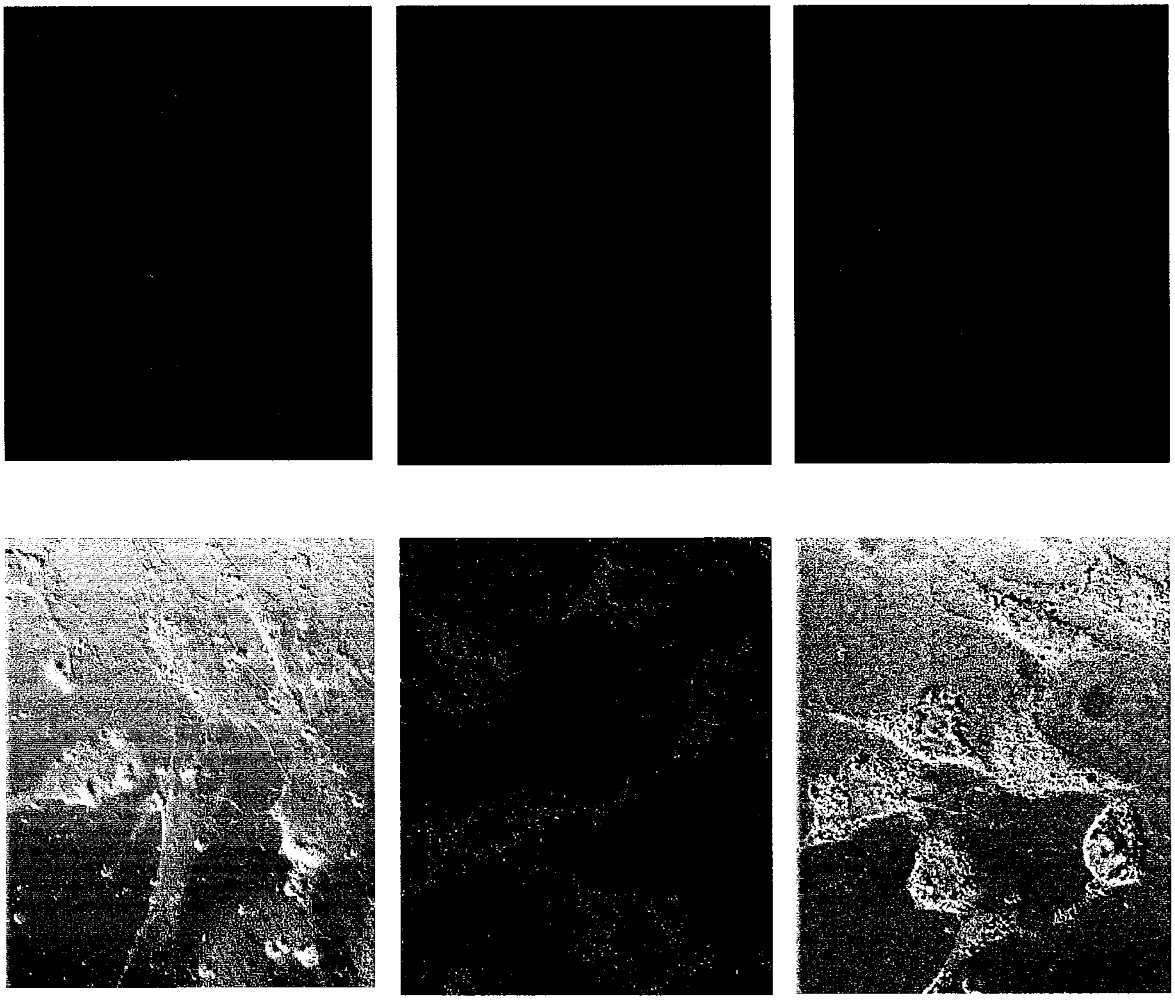

1 h 4 h 30 h

Figure 23. Effects of Ru@NaY exposure on growth-arrested rat keratinocytes. Subconfluent cells in DMEM were incubated in chamber slides with 30 μg/ml of Ru@NaY for the times indicated. The cells were washed with saline twice, stained with cFDA, and excited at 488 nm under LSCM. The upper panels are fluorescence images (from a single plane) and the lower panels are overlays of the fluorescence and DIC images.

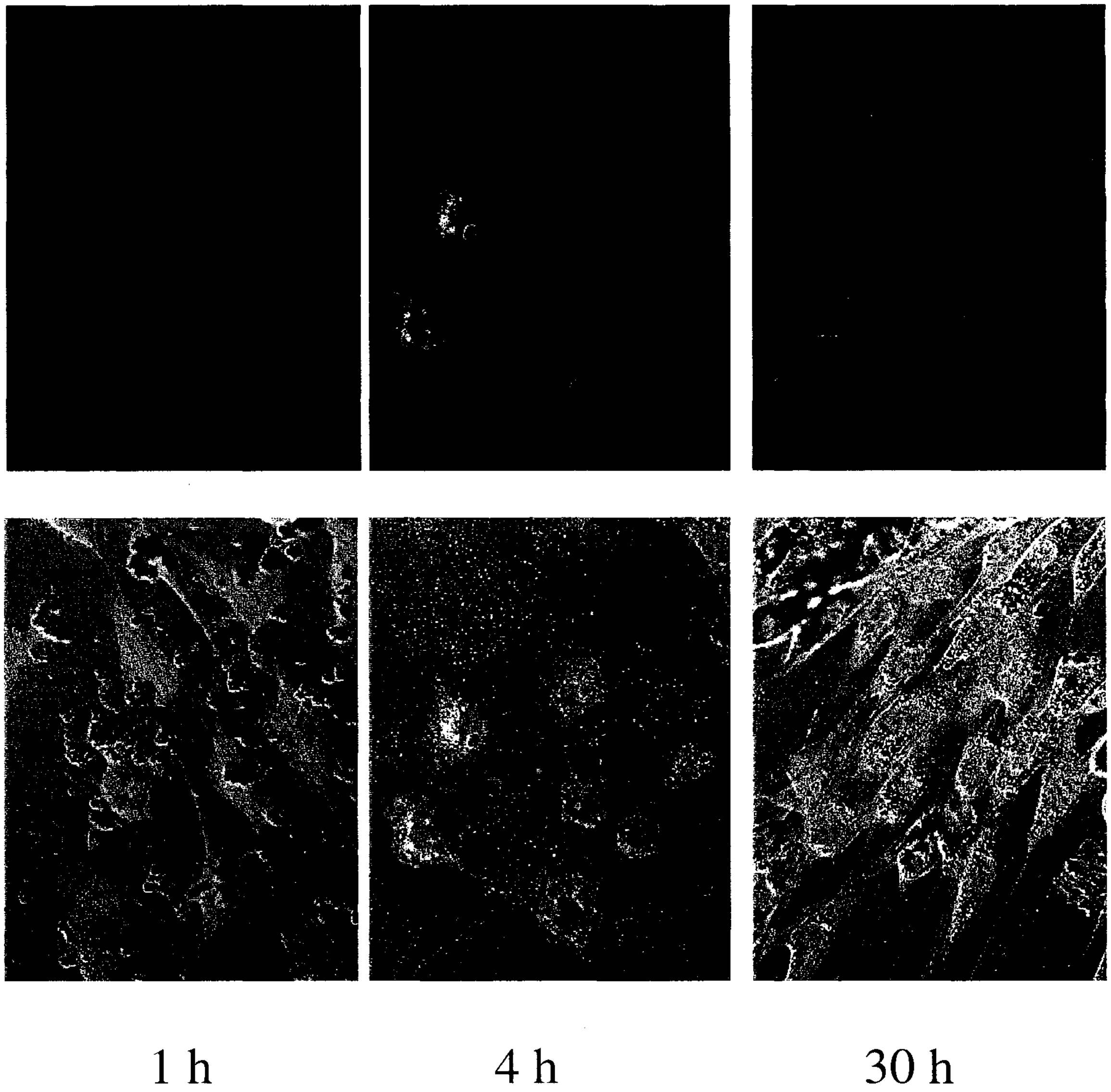
1 h

4 h

30 h

Figure 24. Effects of Ru@NaY exposure on dividing rat keratinocytes. The upper panels are fluorescence images (from a single plane) and the lower panels are overlays of the fluorescence and DIC images. The experimental conditions are given in the caption to Figure 23.

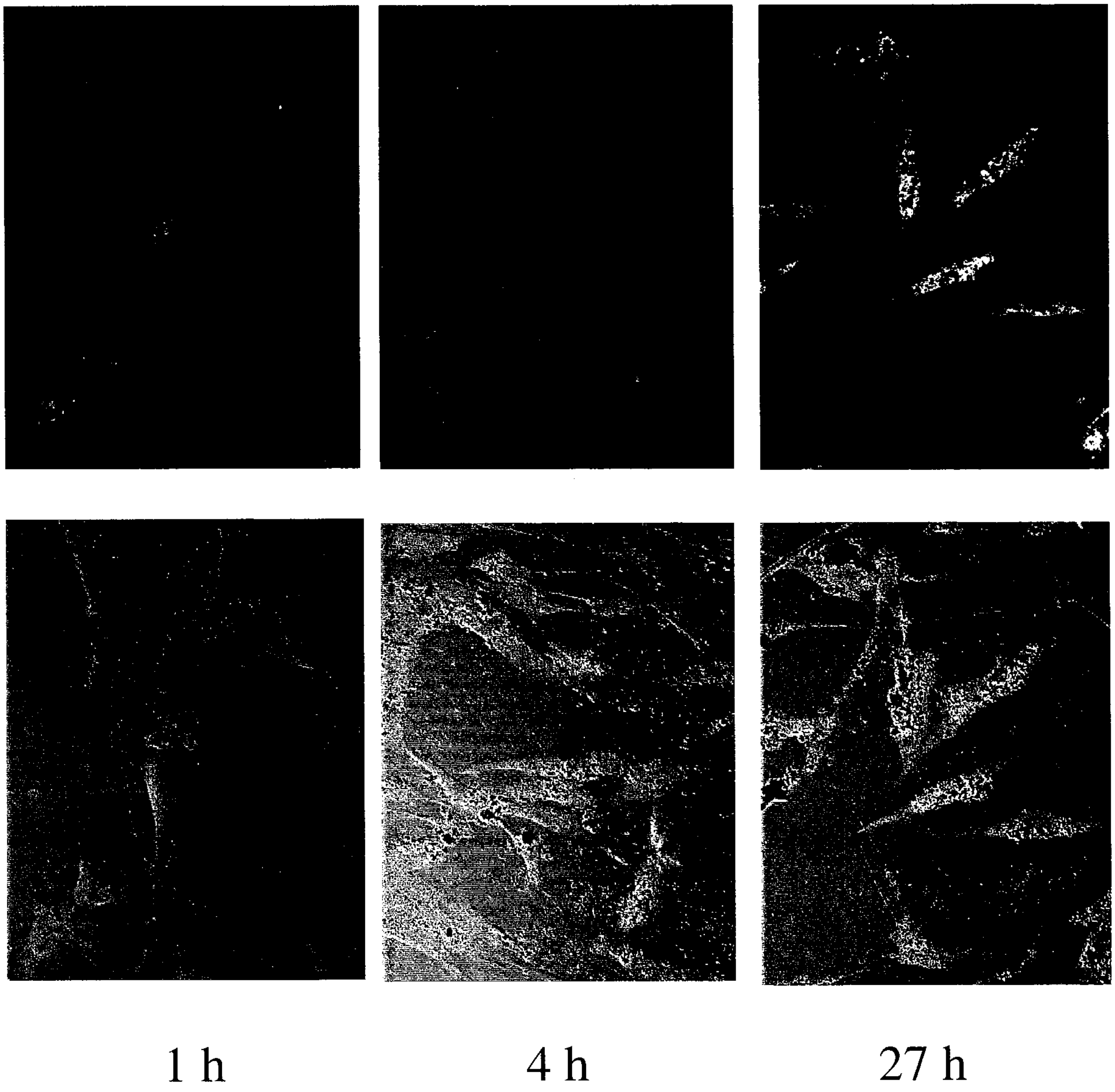

Figure 25. Effects of Ru@NaY exposure on growth-arrested human skin fibroblasts. The upper panels are fluorescence images (from a single plane) and the lower panels are overlays of the fluorescence and DIC images. The experimental conditions are given in the caption to Figure 23.

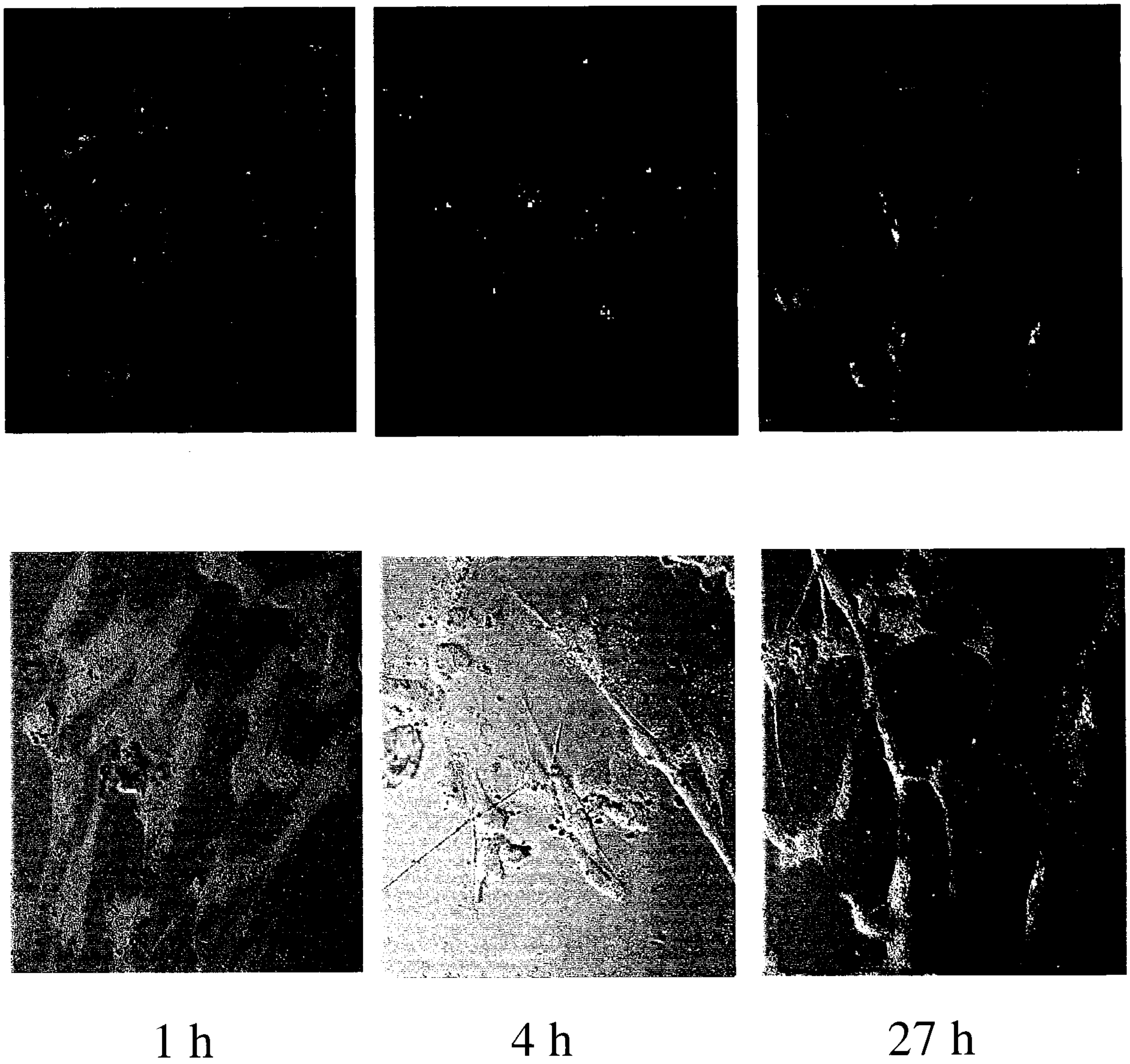

Figure 26. Effects of Ru@NaY exposure on dividing human skin fibroblasts. The upper panels are fluorescence images (from a single plane) and the lower panels are overlays of the fluorescence and DIC images. The experimental conditions are given in the caption to Figure 23.

The same experiments were carried out with F@NaY. After exposure to F@NaY for 1, 4 and 27 h, dividing or growth-arrested human skin fibroblasts were washed with saline and stained with CMTMR. Figure 27 clearly reveals that F@NaY aggregated on the surface of growth-arrested human fibroblasts but did not penetrate the cells. The same results were observed for dividing fibroblasts (data not shown). Z-series scan images and 3D videos confirmed these results (data not shown).

Unmodified NaY was incubated with human skin fibroblasts, the cells were loaded with cFDA and examined by LSCM to verify that the fluorescence of Ru@NaY or F@NaY was from the $Ru(bipy)_3^{2+}$ or fluorescein guests and not from the faujasite itself. In Figure 28, panel A shows the cF fluorescence from the cells and no other fluorescence was detected. Panel B shows the DIC image of the same samples and the faujasite particles are detected. The overlay of the images A and B in panel C reveals that the unmodified faujasite does not fluoresce, and the same results were obtained when the cells were stained with CMTMR (not shown). Thus, the fluorescence detected from the modified zeolite particles must be from the $Ru(bipy)_3^{2+}$ and fluorescein guests and not from the host.

To summarize, the experimental results demonstrate that neither Ru@NaY nor F@NaY penetrated into rat keratinocytes or human skin fibroblasts after 24-30 h exposure to modified zeolites. The zeolites aggregated on the surface of the cells.

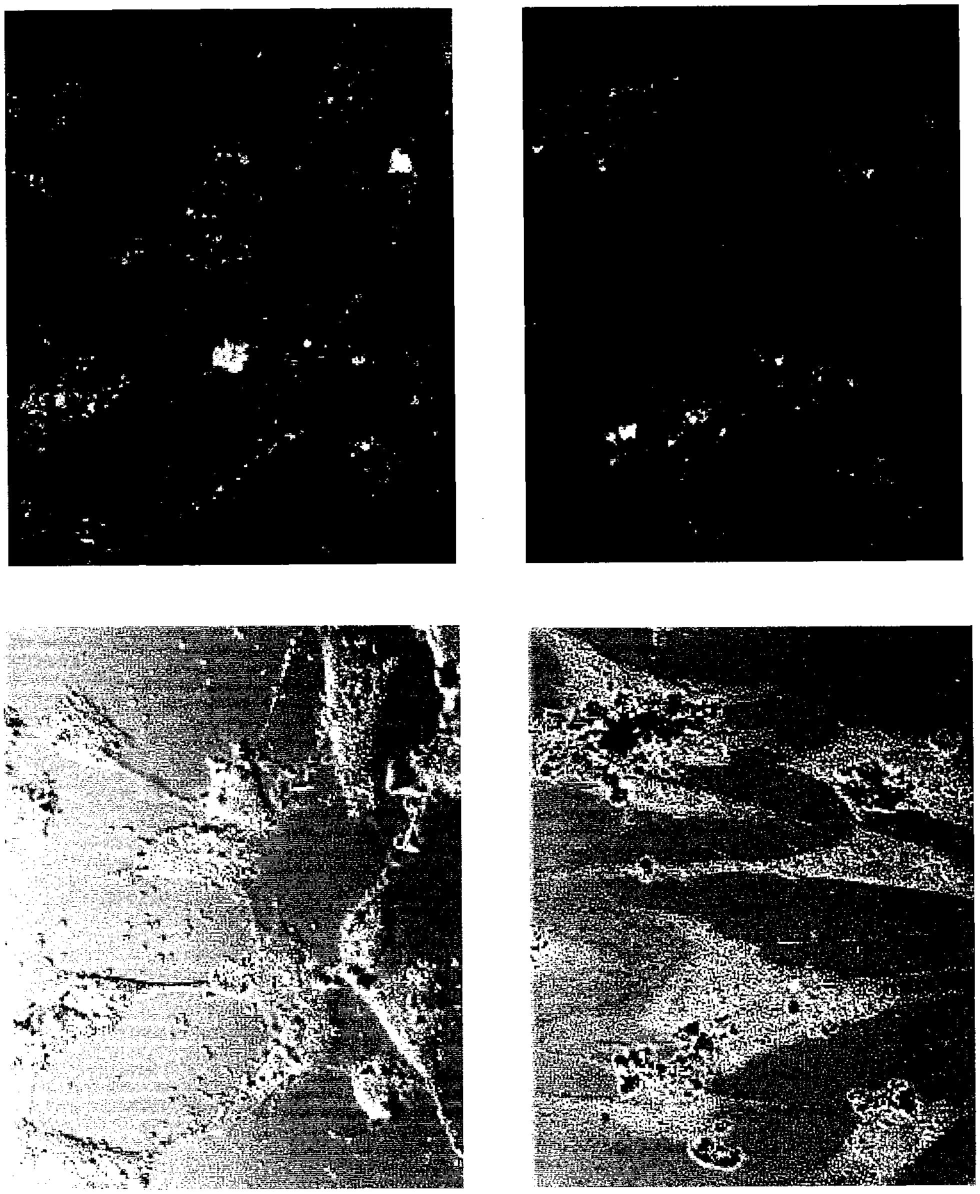

1 h 27 h

Figure 27. Effects of F@NaY exposure on growth-arrested human skin fibroblasts. Subconfluent cells in DMEM were incubated in chamber slides with 30 μg/ml of F@NaY for the times indicated. The cells were washed with saline twice, stained with CMTMR, and simultaneously excited at 488 nm and 543 nm under LSCM. The upper panels are fluorescence images (from a single plane) and the lower panels are overlays of the fluorescence and DIC images.

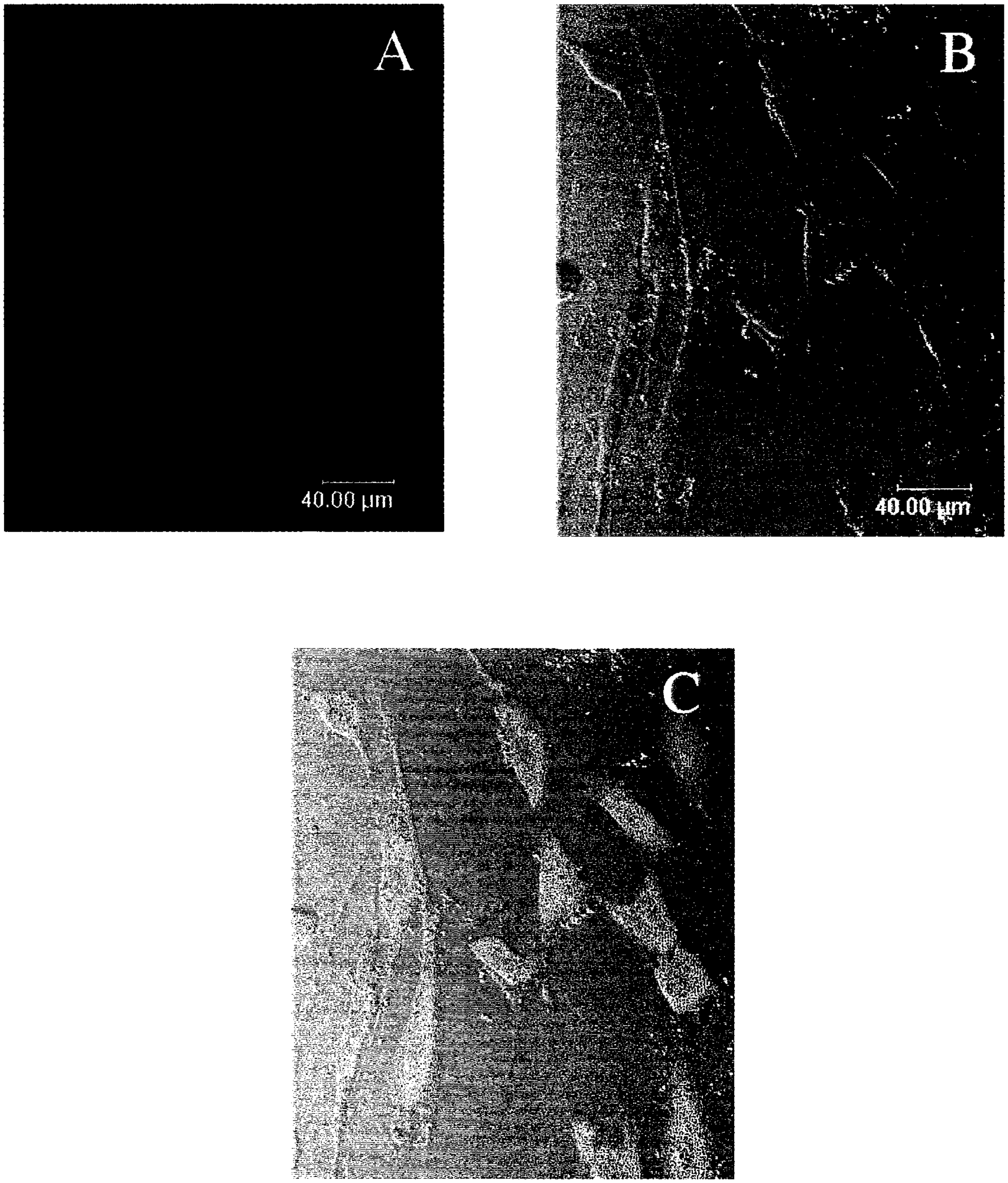

Figure 28. Human skin fibroblasts exposed to free NaY and loaded with cFDA. Subconfluent cells were incubated in saline containing 30 µg/ml of free NaY for ~ 30 min in chamber slides, stained with cFDA, and excited at 488 nm under LSCM. (A) Fluorescence from cF in fibroblasts; (B) DIC image of fibroblasts exposed to free NaY; (C) overlay of the DIC and fluorescence images showing that free NaY is nonfluorescent.

3.3 Effects of UVA, NaY, TiO_2, TiO_2@NaY on oxidative stress in human skin fibroblasts

Oxidative stress is caused by reactive oxygen species (*e.g.*, $O_2^{\bullet -}$, $HO^{\bullet}$, H_2O_2). Oxidative stress can be evaluated by the measurement of H_2O_2 levels in cells. A special fluorescent probe, DCFH-DA, is used to detect changes in H_2O_2 levels in cells by LSCM (Figure 7).

3.3.1 Effect of UVA on H_2O_2 generation in human skin fibroblasts

The effect of UVA alone on H_2O_2 generation in human skin fibroblasts was examined first. After irradiation under UVA lamps for 0 – 45 min, the cells were loaded with DCFH-DA and the fluorescence was examined by LSCM. Figure 29 demonstrates that when the UVA-irradiation time was increased, the fluorescence intensity of DCF inside cells increased, suggesting an increase in intracellular H_2O_2 levels. In Figure 29, the left panels show the untreated DCF fluorescence and the right panels the computer-enhanced images of the same samples. Based on these images, the relative DCF fluorescence intensity was calculated using the software supplied with the microscope. Exposure of human skin fibroblasts to UVA for different times resulted in a large increase in DCF fluorescence intensity with a > 8-fold increase apparent after 45-min UVA irradiation (Figure 30). The statistical analysis is consistent with the fluorescence images; H_2O_2 generation increases with increasing UVA irradiation. The error bar for the UVA 45-min time point is large. As indicated in Figure 30, the experiment was repeated three times. The microscope was broken between the first and second trials. The results of the last two trials were close but are very different from the first trial.

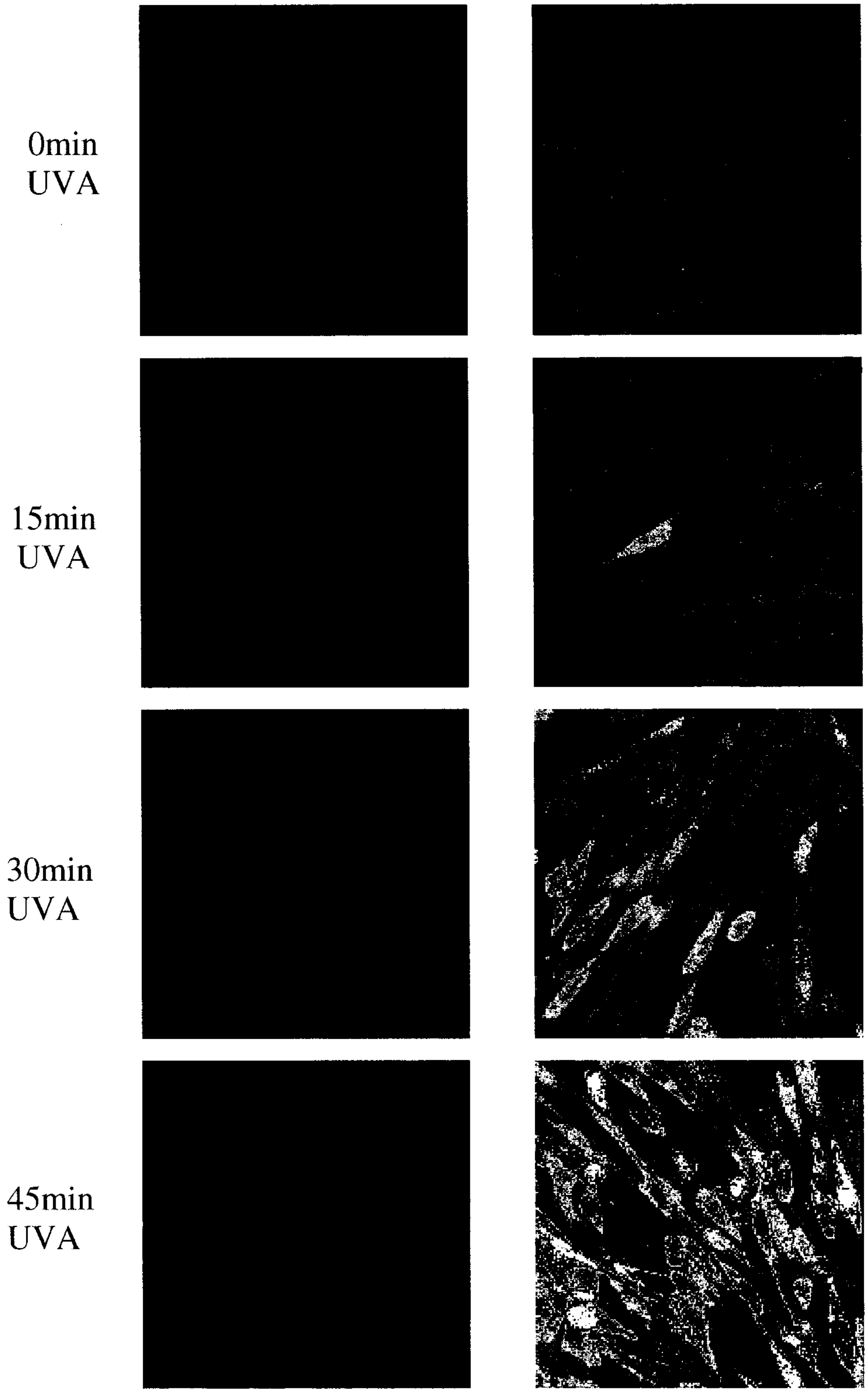

Figure 29. DCF fluorescence in human skin fibroblasts after UVA irradiation for different times. Left panels show DCF fluorescence and right panels are the computer-treated images of the fluorescence. H_2O_2 levels increase with increasing UVA irradiation. Harvested cells were irradiated under UVA lamps (~ 2.0 mW/cm^2) in 1 ml HBSS in chamber slides at 25°C for 45 min and examined by LSCM.

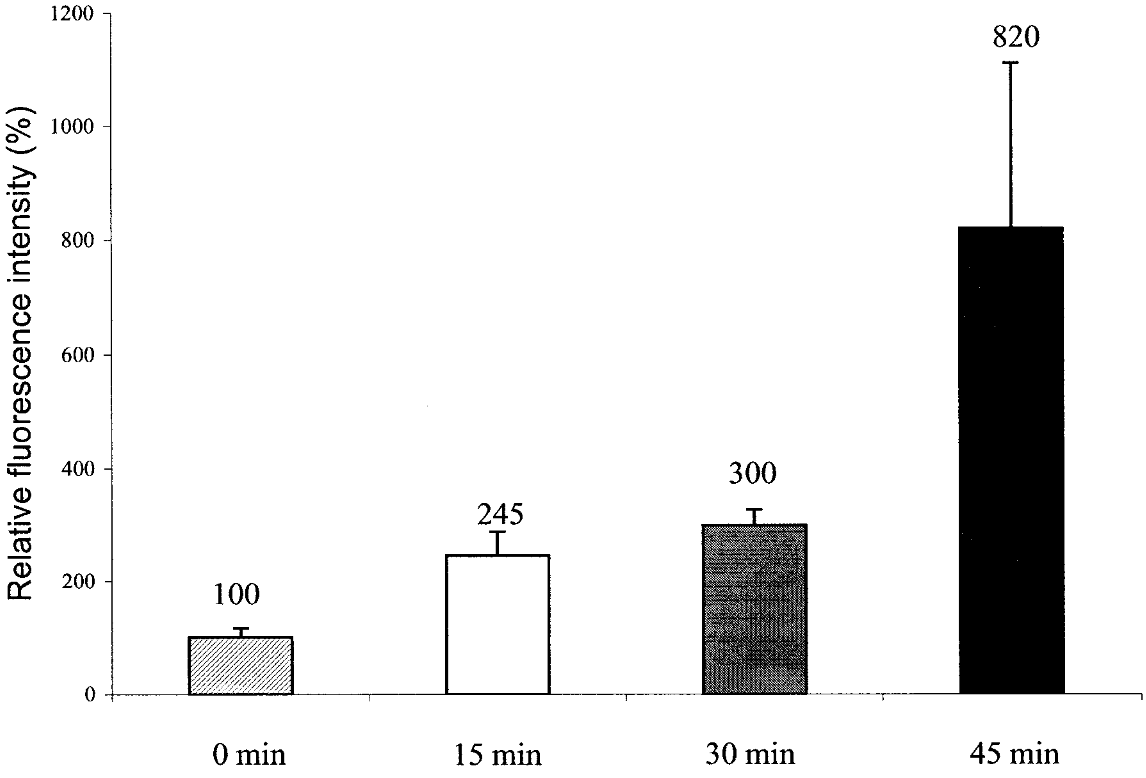

Figure 30. Change in H_2O_2 levels in human skin fibroblasts after UVA irradiation. Harvested cells were irradiated under UVA lamps (~ 2.0 mW/cm^2) in 1 ml HBSS in chamber slides at 25°C for up to 45 min. Fluorescence intensity was averaged over 200 cells for each sample, and the values are relative to the control (0 min). The error bars represent the standard derivation of three experiments (n = 3).

We next examined whether TEMPOL, a free radical and H_2O_2 scavenger, and a superoxide dismutase (SOD) mimic (47, 49, 50), prevented the oxidation of DCFH. Human skin fibroblasts were exposed to UVA irradiation in the absence and presence of 5 mM TEMPOL. The addition of TEMPOL inhibited the increase in DCF fluorescence (Figure 31), induced by 50-min UVA irradiation. However, TEMPOL did not reduce DCF fluorescence in nonirradiated cells, suggesting that the additional H_2O_2, formed from superoxide generated by UVA, participated in DCFH oxidation.

TEMPOL shows maximal absorption between 230 and 250 nm with little absorption above 320 nm (Figure 32). Since the energy intensity spectrum of UVA lamps (Figure 32; data from Luzchem Research) used in the experiments dose not overlap with TEMPOL absorption, the reduction of DCF fluorescence seen in Figure 31 is not due to the absorption of UVA radiation by TEMPOL.

3.3.2 Effect of UVA plus TiO_2, NaY and TiO_2@NaY on H_2O_2 generation in human skin fibroblasts

The effect of exposure of human skin fibroblasts to UVA in the presence of TiO_2, NaY and TiO_2@NaY was examined by LSCM. Compared to the control, the DCF fluorescence increased about 2-fold after UVA irradiation, which is consistent with the results in Figure 30. UVA irradiation in the presence of TiO_2 increased the fluorescence over 2-fold (Figure 33), suggesting that TiO_2 promotes H_2O_2 generation in irradiated cells as shown previously (17, 18). However, the fluorescence of cells exposed to free TiO_2 plus NaY (TiO_2+NaY) increased even more on UVA irradiation compared to cells exposed to TiO_2 only. The fluorescence of cells exposed to free NaY or TiO_2@NaY

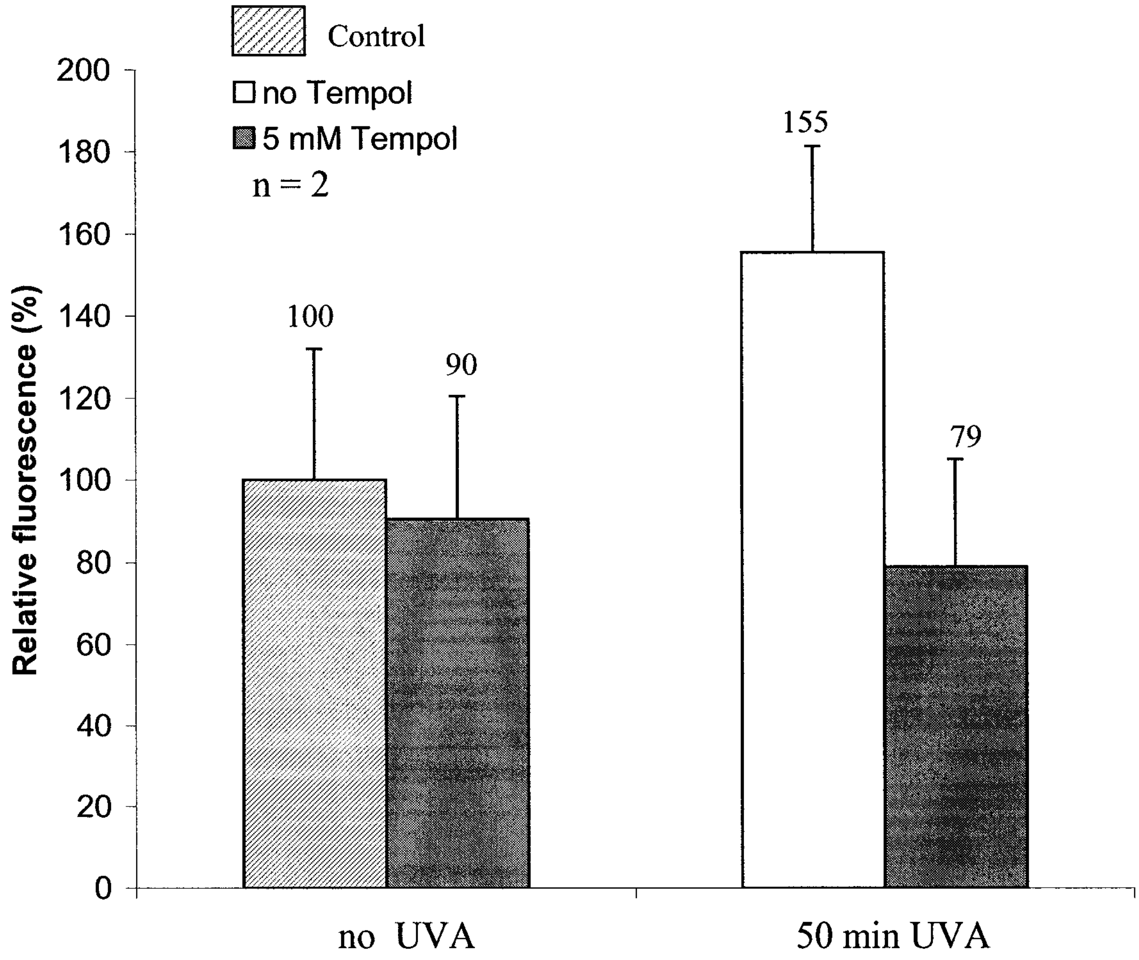

Figure 31. Effect of TEMPOL on H_2O_2 generation in UVA-irradiated human skin fibroblasts. Fluorescence intensity averaged over >150 cells for each sample. The values are relative to the control (no UVA, no TEMPOL).

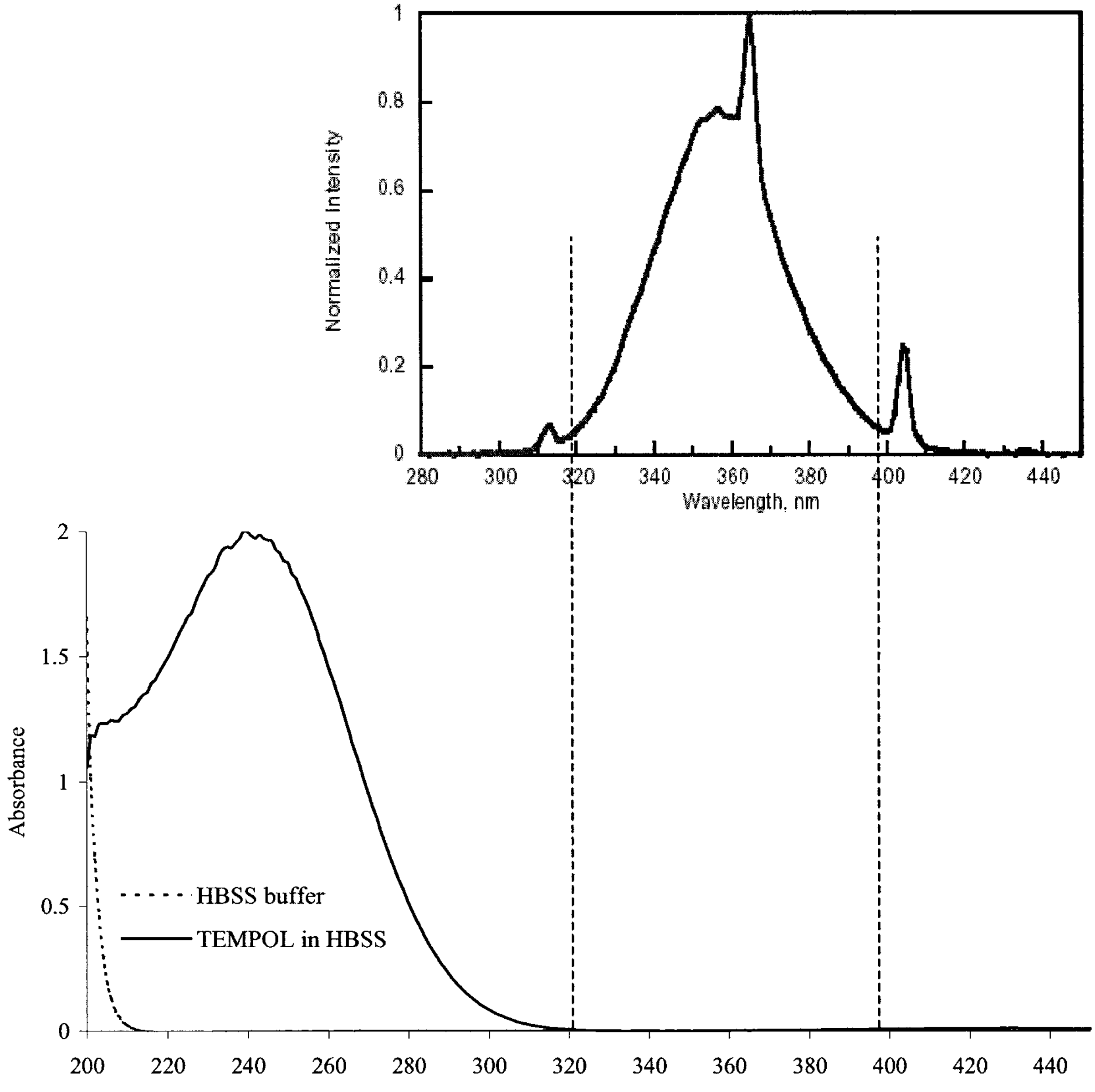

Figure 32. Absorption spectrum of TEMPOL in HBSS buffer *vs* the energy intensity spectrum of the UVA lamps used in the experiments.

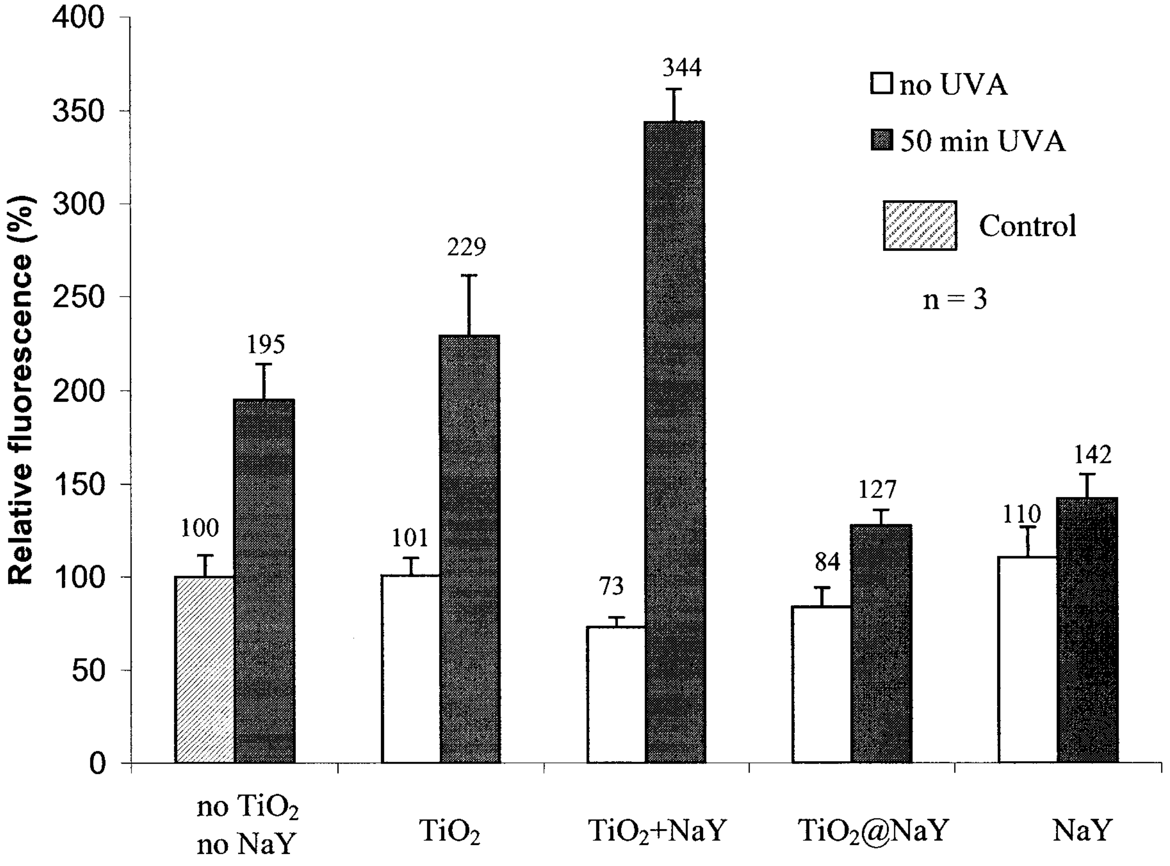

Figure 33. Changes in H_2O_2 levels after 50-min UVA irradiation of human skin fibroblasts exposed to 0.05 mg/ml TiO_2, 0.05 mg/ml TiO_2 plus 0.45 mg/ml NaY (TiO_2:NaY=1:9), 0.5 mg/ml TiO_2@NaY, and 0.5 mg/ml NaY. The fluorescence intensity was averaged over 200 cells for each sample. The values are relative to the control (no UVA, no TiO_2, no NaY).

showed little increase on UVA irradiation. However, without UVA irradiation, the fluorescence of cells exposed to TiO_2+NaY or TiO_2@NaY was less than control cells (Figure 33). These results show that irradiated TiO_2 promoted H_2O_2 generation in cells even when free NaY was present, although the presence of free NaY reduced H_2O_2 generation in cells in the absence of TiO_2. Like free NaY, TiO_2@NaY also reduces H_2O_2 generation in cells under UVA irradiation. Clearly, encapsulation should protect cells from the damage caused by the H_2O_2 produced by UVA-irradiated TiO_2.

Discussion

The proposed supramolecular sunscreens are based on supramolecular chemistry. Submicron particles of a well-defined porous material (zeolites) act as hosts for the actual sunscreen ingredients to alleviate the adverse side effects on the skin, especially under UV radiation, by preventing direct contact of the sunscreen guests with skin. In order to assess the safety of supramolecular sunscreen components, cell penetration of the modified zeolites, Ru@NaY and F@NaY, was tested in this study. Also, the effect of the components on UVA-induced H_2O_2 generation in cells was measured using the fluorescent probe, DCFH-DA.

Zeolites have been studied widely in the context of animal feeds (40) and are recorded as safe oral contrast agents for MRI work (51). The identification and safety of zeolites as hosts in supramolecular sunscreens have not been established. Some sunscreen ingredients such as TiO_2 and PABA penetrate into skin cells and cause adverse side effects (*e.g.*, DNA damage) upon UVR (18, 25). To assess their safety, it is necessary to determine if zeolite particles penetrate into cells. Hence the leakage of guest molecules from the zeolites and the penetration of zeolites into cells were examined using fluorescent guests. Membrane-permeant fluorophores (cFDA, DCFH-DA, CMTMR) that freely diffuse through the membranes of viable cells were used as counterstains in our studies. Confocal fluorescence microscope analysis of yeast, rat keratinocytes and human skin fibroblasts following treatment with free and encapsulated fluorophores was used to determine if the zeolite-fluorophore complexes penetrate the cells under a variety of conditions.

Studies with yeast cells, which are easy to manipulate, allowed us to develop expertise in the use of fluorophores and confocal microscopy. The results obtained show that cFDA and DCFH-DA permeate live yeast cells. Fluorescent cF derived from cFDA was retained in the cells presumably because it possesses extra negative charges whereas DCF derived from DCFH-DA rapidly leaked from the cells (Figure 8). These results are consistent with previous studies (44, 52). $Ru(bipy)_3^{2+}$ permeated yeast cells when the cells were suspended in deionized water but not in PBS. This may be due to osmotic imbalance across the cell membrane and/or to electrostatic attraction between the cell surface and $Ru(bipy)_3^{2+}$ in water. Penetration of the probes into the yeast cells was confirmed using LSCM.

Penetration of the fluorophores into rat keratinocytes and human skin fibroblasts in 0.9% saline was also examined by LSCM. Unlike yeast cells, mammalian cells burst in water, and have to be examined in osmosis-balanced buffer such as 0.9% saline, which was chosen for our studies for convenience. Dividing and growth-arrested mammalian cells attached to slides is closer to their natural environment than suspensions. Mammalian cells settle to the bottom of cuvette more readily than yeast cells because of their greater mass, so it was difficult to detect the fluorescence from fluorophores in mammalian cells using a spectrofluorometer. Like yeast cells, rat keratinocytes and human fibroblasts were easily loaded with cFDA and DCFH-DA, and cF was trapped in the cells much better than DCF. Neither the keratinocytes nor the fibroblasts could be loaded with $Ru(bipy)_3^{2+}$ in saline, similar to the results with yeast cells in PBS. The penetration of fluorescein into mammalian cells also was tested by confocal microscopy under normal conditions. It was difficult to load rat keratinocytes with fluorescein even on incubation for 30 min. However, human skin fibroblasts could be loaded with fluorescein although not to the same extent as cFDA and DCFH-DA. Differences in membrane structure and composition between keratinocytes and fibroblasts clearly lead to differences in fluorescein permeability and retention.

Confocal microscopy was used to examine the penetration of fluorochrome-labeled zeolite particles into the cells. Use of Ru@NaY and F@NaY allows visualization of the zeolite particles, and to ensure that the fluorescence is from encapsulated and not free probes, their escape from the zeolite hosts was tested. The results showed that $Ru(bipy)_3^{2+}$, TP^+ and fluorescein were retained in zeolites (Figures 17, 18, 19), and no leakage of the fluorescent guests was detected over 24 h. Hence, cell penetration of the modified zeolite particles can be followed by monitoring guest fluorescence. Because of its Z-series scan function and high-resolution images, confocal microscopy is a very useful method to determine the penetration of fluorophore-modified particles into cells and the distribution profile within cells. All the collected images, especially the Z-series scan images, showed that neither Ru@NaY nor F@NaY penetrated into rat keratinocytes or human skin fibroblasts. The faujasite particles aggregated on the surface of the cells, which is clearly seen in the 3D video (not shown) of the Z-series images. If the modified particles penetrated into the cells, they would be distributed evenly within cells and not aggregated at several places like the images shown in Figures 23-27.

As skin is in contact with oxygen and increasingly exposed to UVR, due to degradation of the protective ozone layer, the risk of photooxidative damage induced by ROS, leading to phototoxicity, photoaging, and skin cancer, has increased substantially (53–56). ROS are produced from molecular oxygen by the mitochondrial electron carriers and enzymes during the normal metabolism of aerobic cells. It is well known that UVA and UVB irradiation induces the formation of ROS in cutaneous tissues (9, 57 – 61). To protect them from oxidative injury, aerobic cells have evolved a complex antioxidant defense system. However, if the ROS load reaches a critical concentration and overwhelms the antioxidative defense, oxidative or, if mediated by UVR, photooxidative damage to all cellular components including DNA, proteins, lipids, and membranes eventually occurs (9, 62 – 65). Since UVA radiation constitutes more than 90% of the terrestrial UV solar energy spectrum (Figure 1) and penetrates more efficiently than UVB into the proliferative basal layers of the epidermis (66, Figure 3), its effect on skin has been characterized as intrinsic photoaging induced by ROS generation (67). Our studies on ROS generation upon UVA irradiation, which utilized the H_2O_2-index probe DCFH-DA and confocal microscopy, showed increased H_2O_2 generation in a UVA-dose dependent manner consistent with the previous studies (58, 59). The cells in the experiment summarized in Figure 31 were irradiated by UVA for a longer time (50 min) than the cells used in Figure 30 (45 min) but the UVA-induced fluorescence reported in Figure 31 is lower than that in Figure 30. This may be due to the fact that the cells used in the two experiments were at different passages (14th and 11th), and their sensitivity to UVA was different.

To identify the active oxygen species responsible for the oxidation of DCFH (Figure 7), previous studies (46, 68) examined whether catalase, an enzyme that decomposes H_2O_2, prevented the oxidation of DCFH. The addition of catalase completely inhibited the increase in DCF fluorescence intensity after inducing H_2O_2, suggesting that H_2O_2 participated in DCFH oxidation (46, 68). To confirm that DCFH oxidation was caused by

UVA-induced ROS in human skin fibroblasts, we attempted to repeat the above experiments with catalase, which was transferred into cells by electroporation. However, the catalase activity was lost or decreased upon UVA irradiation, and catalase does not permeate biological membranes and has to be incorporated into cells by electroporation. TEMPOL, a superoxide scavenger that is water-soluble and permeates biological membranes, was instead used to examine its effect on DCFH oxidation in our experiments. TEMPOL inhibits oxidative damage mainly by removing superoxide anions (69, 70, 71). Investigators have demonstrated the capability of TEMPOL to protect mammalian cells from damage by superoxide and hydrogen peroxide (47, 49, 50, 71), although TEMPOL exhibits no catalase-like activity. $O_2^{\bullet -}$ production also leads to H_2O_2 production due to the disproportionation reaction:

$$O_2^{\bullet -} + O_2^{\bullet -} + 2H^+ \xrightarrow{SOD} H_2O_2 + O_2$$

This reaction, which is either nonenzymic or catalyzed by SOD, is one of the main sources of H_2O_2 *in vivo* (72). Our results demonstrated that DCF fluorescence intensity was reduced under UVA irradiation after addition of TEMPOL, but the DCF fluorescence intensity of non-irradiated cells with TEMPOL was almost the same as that of the control (Figure 31). These results suggest that the UVA-induced superoxide anion was scavenged by TEMPOL leading to reduction of its downstream product, H_2O_2, and confirmed that DCFH oxidation was caused by UVA-induced H_2O_2..

The formation of ROS, especially hydroxyl radicals, by UV-irradiated TiO_2 has been reported (16, 17, 73) as well as *in vitro* photooxidative damage sensitized by TiO_2 (18, 23, 38, 74). The formation of ROS varied with both the crystal size and form of TiO_2. UV-irradiation of the anatase form produced more free radicals than the rutile form (16, 17). Our results on the effect of UVA-irradiated TiO_2 (anatase form) on H_2O_2 generation in human skin fibroblasts (Figure 33) are consistent with previous reports of irradiated-TiO_2 promoting H_2O_2 generation in cells *in vitro*. The effects of UVA-irradiated NaY and TiO_2 encapsulated in NaY (TiO_2@NaY) on H_2O_2 generation also were examined (Figure 33). The results show that NaY alone protected cells from H_2O_2 generation and that TiO_2@NaY dramatically reduced the H_2O_2 levels in cells under UVA irradiation.

Could NaY be used in sunscreens to prevent UVR damage because of its capability to reduce UVR-induced ROS? The answer is no. Faujasites are usually produced in particle sizes between 500 and 1000 nm, which makes them ideal for *in vitro* studies, but too large to be cosmetically acceptable. Large particles result in more opacity (14) and any color rendered to sunscreen by an ingredient (whitening) is undesirable. Also, studies have shown that the smaller the particle size, the less UV light transmitted and better UVB and UVA protection is expected (14). The goal of our studies was to examine the ability of TiO_2@NaY to protect cells from the adverse effects of UVA-irradiated TiO_2. The results demonstrate that unlike free TiO_2 plus free NaY, which promote H_2O_2 generation, TiO_2@NaY protects cells from ROS generation upon UVA irradiation (Figure 33).

Free faujasite also was shown to reduce H_2O_2 generation in fibroblasts (Figure 33). However, since faujasite particles are too large (200–1000 nm) to be cosmetically acceptable, small zeolites such as β-nanocrystalline (20–30 nm), which have the particle size favoured by the cosmetic industry, should be tested. Unfortunately, sufficient quantities of modified β-nanocrystalline ware not available for this work. However, in future research, the penetration of β-nanocrystalline into cells should be tested since TiO_2 particles of this size are capable of penetrating into the lower layers of the skin (23, 34). Also, the ability of organic sunscreen components encapsulated in zeolites in preventing ROS damage (H_2O_2 generation) in skin cells upon UVA irradiation should be examined.

References

1. K. C. Farmer and M. F. Naylor (1996). Sun exposure, sunscreens, and skin cancer prevention: a year-round concern. Ann Pharmacother. 30: 662-673.

2. W. Frain-Bell (1985).Cutaneous Photobiology, Oxord University Press.

3. V. Bissonauth, R. Drouin, D. L. Mitchell, M. Rhainds, J. Claveau and M. Rouabhia (2000). The efficacy of a broad-spectrum sunscreen to protect engineered human skin from tissue and DNA damage induced by solar ultraviolet exposure. Clin Cancer Res. 6: 4128-4135.

4. M. Wlaschek, I. T.-Poor, L. Naderi, W. Ma, L. A. Schneider, Z. R.-Wolf, J. Schuller and K. S.-Kochanek (2001). Solar UV irradiation and dermal photoaging. J Photochem Photobiol B. 63: 41-51.

5. E. M. Gil and T. H. Kim (2000). UV-induced immune suppression and sunscreen. Photodermatol Photoimmunol Photomed. 16:101-110.

6. F. P. Gasparro, M. Mitchnick and J. F. Nash (1998). A review of sunscreen safety and eficacay. Photochem Photobiol. 68: 243-256.

7. S. Q. Wang,, R. Setlow, M. Berwick, D. Polsky, A. A. Marghoob, A. W. Kopf and R. S. Bart (2001). Ultraviolet A and melanoma: A review. J Am Acad Dermatol. 44: 837-846.

8. M. T. Leccia, M. Yaar, N. Allen, M. Gleason and B. A. Gilchrest (2001). Solar simulated irradiation modulates gene expression and activity of antioxidant enzymes in cultured human dermal fibroblasts. Exp Dermatol. 10: 272-279.

9. C. S. Sander, H. Chang, S. Salzmann, C. S. L. Muller, S. E.-Mudiyanselage, P. Elsner and J. J. Thiele (2002). Photoaging is associated with protein oxidation in human skin in vivo. J Invest Dermatol. 118: 618-625.

10. C. Cayrol, J. Sarraute, R. Tarroux, D. Redoules, M. Charveron and Y. Gall (1999). A mineral sunscreen affords genomic protectio against ultraviolet (UV) B and UVA radiation: in vitro and in situ assays. Br J Dermatol. 141: 250-258.

11. F. P. Gasparro (2000). Sunscreens, skin photobiology, and skin cancer: the need for UVA protection and evaluation of efficacy. Environ Health Perspect. 108:71-78.

12. J. M. Allen, C. J. Gossett and S. K. Allen (1996). Photochemical formation of singlet molecular oxygen ($^1O_2$) in illuminated aqueous solutions of p-aminobenzoic acid (PABA). J Photochem Photobiol B. 32: 33-37.

13. C. Xu, A. Green, A. Parisi and P. G. Parsons (2001). Photosensitization of the sunscreen octyl p-dimethylaminobenzoate by UVA in human melanocytes but not in keratinocytes. Potochem Photobiol. 73: 600-604.

14. Y. Shao, and D. Schlossman (1999). Effect of particle size on performance of physical sunscreen formulas. Presented at PCIA Conf. Shanghai, PRC.

15. M. Sakamoto, H. Okuda, H. Futamata, A. Sakai and M. Lida (1995). Influence of particles size of titanium dioxide on UV-ray shielding property. J Jpn. Soc. Mater. 68: 203-210.

16. T. Uchino, H. Tokunaga, M. Ando and H. Utsumi (2002). Quantitative determination of OH radical generation and its cytotoxicity induced by TiO_2-UVA treatment. Toxicol In Vitro. 16: 629-635.

17. T. Ashikage, M. Wada, H. Kobayashi, M. Mori, Y. Katsumura, H. Fukui, S. Kato, M. Yamaguchi and T. Takamatsu (2000). Effect of the photocatalytic activity of TiO_2 on plasmid DNA. Mutat Res. 466: 1-7.

18. W. G. Wamer, J.-J. Yin and R. R. Wei (1997). Oxidative damage to nucleic acids photosensitized by titanium dioxide. Free Radic Biol Med. 23: 851-858.

19. M. Gulston and J. Knowland (1999). Illumination of human keratinocytes in the presence of the sunscreen ingredient Padimate-O and through an SPF-15 sunscreen reduces direct photodamage to DNA but increase strand breaks. Mutat Res. 444: 49-60.

20. J. Knowland, E. A. Mckenzie, P. J. McHugh and N. A. Cridland (1993). Sunlight-induced mutagenicity of a common sunscreen ingredient. FEBS Lett. 324: 309-313.

21. P. J. McHugh and J. Knowland (1997). Characterization of DNA damage inflicted by free radicals from a mutagenic sunscreen ingredient and its location using an in vitro genetic reversion assay. Photochem Photobiol. 66: 276-281.

22. C. L. Greenstock and E. Harold (1968). Photosensitized dimerization of pyrimidines. Biochem Biophys Res Commun. 30: 21-27.

23. R. Cai, K. Hashimoto, K. Itoh, Y. Kubota and A. Fujishima (1991). Photokilling of malignant cells with ultrafine TiO_2 powder. Bull. Chem. Soc. Japan 64: 1268-1273.

24. I. H. Blank, III. H. Joseph, R. R. Anderson, K. F. Jaenicke and J. A. Parrish (1982). Observations on the mechanism of the protective action of sunscreens. J Invest Dermatol. 78: 381-385.

25. A. Arancibia, G. Borie, D. Cornwell, C. Medrano (1981). Pharmacokinetic study on the percutaneous anbsorption of p-aminobenzoic acid from three sunscreen preparations. Farmaco [Prat]. 36: 357-365.

26. F. P. Gasparro (1993). The molecular basis of UV-induced mutagenicity of sunscreens. FEBS Lett. 336: 184-185.

27. J. M. Allen and C. J. Gossett (1996). Photochemical formation of singlet molecular oxygen in illuminated aqueous solutions of several commercially available sunscreen active ingredients. Chem Res Toxicol. 9: 605-609.

28. D. D.-Debergh, J. Piette and C. Laurent (1989). Cytotoxic and genotoxic effects of extracellular generated singlet oxygen in human lymphocytes in vitro. Mutat Res. 225: 11-14.

29. W. C. Eisenberg, K. Taylor and R. R. Guerrero (1992). Cytogenetic effects of singlet oxygen. J Photochem Photobiol B. 16: 381-384.

30. D. Sairhurst (1997). Surface coating and the optimization of microfine oxides in sunscreen formulatios. Cosmetics & Toiletries Oct. 112: 81-88.

31. M. Kobayashi and W. Kalriess (1997). Photocatalytic activity of titanium dioxide and zinc oxide. Cosmetics & Toiletries Jun. 112: 83-86.

32. V. P. S. Judin (1993). The lighter side of TiO_2. Chemistry in Britain. 503-505.

33. M. R. Hoffman, S. T. Martin, W. Choi and D. W. Bahncmann (1995). Environmental applications of semiconductor photocatalysis. Chem Rev. 95: 69-99.

34. M.-H. Tan, C. A. Commens, L. Burnett and P. J. Snitch (1996). A pilot study on the percutaneous absorption of microfine titanium dioxide from sunscreens. Australas J Dermatol. 37: 185-187.

35. J. Lademann, H.-J. Weigmann, C. Rickmeyer, H. Barthelmes, H. Schaefer, G. Mueller and W. Sterry (1999). Penetration of titanium dioxide microparticles in a sunscreen formulation into the horny layer and the follicular orifice. Skin Pharmacol Appl Skin Physiol. 12:247-256.

36. T. Saito, T. Iwase, J. Horie and T. Morioka (1992). Mode of photocatalytic bactericidal action of powdered semiconductor titanium dioxide on mutans streptococci. J Photochem Photobiol B. 14:369-379.

37. H. Sakai, E. Ito, R-X. Cai, T. Yoshioka, Y. Kubota, K. Hashimoto and A. Fujishima (1994). Intracellular Ca^{2+} concentration change of T24 cell under irradiation in the presence of TiO_2 ultrafine particles. Biochim Biophys Acta. 1201: 259-265.

38. T. Hancock-Chen and J. C. Scaiano (2000). Enzyme inactivation by TiO_2 photosensitization. J Photochem Photobiol B. 57: 193-196.

39. G. Cosa, M. S. Galletero, L. Fernandez, F. Marquez, H. Carcia and J. C. Scaiano (2002). Tuning the photocatalytic activity of titanium dioxide by encapsulation inside zeolites exemplified by the cases of thianthrene photooxygenation and horseradish peroxidase photodeactivation. New J Chem. 0: 1-8.

40. F. A. Mumpton (1999). La roca magica: Uses of natural zeolites in agriculture and industry. Proc Natl Acad Sci U S A. 96: 3463-3470.

41. J. C. Scaiano and H. Garcia (1999). Intrazeolite photochemistry: Toward supramolecular control of molecular photochemistry. Acc Chem Res. 32: 783-793.

42. J. S. Beck, J. C. Vartuli, W. J. Roth, M. E. Leonowica, C. T. Kresge, K. D. Schmitt, C. T-W. Chu, D. H. Olso, E. W. Sheppard, S. B. McCullen, J. B. Higgins and J. L. Schlenker (1992). A new family of mesoporous molecular sieves prepared with liquid crystal templates. J Am Chem Soc. 114: 10834-10843.

43. C. Cole (2001). Sunscreen protection in the ultraviolet A region: how to measure the effectiveness. Photodermatol Photoimmunol Photomed. 17: 2-10.

44. P. Breeuwer, J. L. Drocourt, N. Bunschoten, M. H. Zwietering, F. M. Rombouts and T. Abee (1995). Characterization of uptake and hydrlysis of flurescein diacetate and carboxyfluorescein diacetate by intracellular esterases in Saccharomyces cerevisiae, which result in accumulation of flurescent product. Appl Environ Microbiol. 61: 1614-1619.

45. D A. Bass, J. W. Parce, L. R. Dechatelet, P. Szejda, M. C. Seeds and M. Thomas (1983). Flow cytometric studies of oxidative product formation by neutrophils: a graded response to membrane stimulation. J Immunol. 130: 1910-1917.

46. Y. S. Bae, S. W. Kang, M. S. Seo, I. C. Baines, E. Tekle, P. B. Chock and S. G. Rhee (1997). Epidermal growth factor (EGF)-induced generation of hydrogen peroxide. J Biol Chem. 272: 217-221.

47. J. B. Mitchell, A. Samuni, M. C. Kishna, W. G. DeGraff, M. S. Ahn, U. Samuni and A. Russo (1990). Biologically active metal-independent superoxide dismutase mimics. Biochemistry. 29: 2802-2807.

48. E. F. Bernstein, S. K. Kong, D. B. Brown, B. C. Kwak, T. Takeuchi, R. P. Gasparro and J. Uitto (2001). The nitroxide Temopl affords protection against ultraviolet radiation in a transgenic murine fibroblast culture model of cutaneous photoaging. Exp Dermatol. 10: 55-61.

49. J. B. Mitchell, W. DeGraff, D. Kaufman, M. C. Krishna, A. Samuni, E. Finkelstein, M. S. Ahn, S. M. Haha, J. Gamson and Angelo Russo (1991). Inhibition of Oxygen-dependent radiation-induced damage by the nitroxide superoxide dismutase mimic, Tempol. Arch Biochem Biophys. 289: 62-70.

50. J. R. Reddan, M. D. Sevilla, F. J. Giblin, V. Padgaonkar, D. C. Dziedzic, V. Leverenz, I. C. Misra and J. L. Peters (1993). The superoxide dismutase mimic Tempol protects cultured rabbit lens epithelial cells from hydrogen peroxide insult. Exp Eye Res. 56: 543-554.

51. S. W. Young, F. Qing, D. Rubin, K. J. Jr Balkus, J. S. Engel, J. Lang, W. C. Dow, J. D. Mutch and R. A. Miller (1995). Gadolinium zeolite as an oral contrast agent for magnetic resonance imaging. Magn Reson Imaging 5: 499-508.

52. W. Jakubowski and G. Bartosz (1997). Estimation of oxidative stress in Saccharomyces cerevisae with flurescent probes. Int Biochem cell Biol. 29: 1297-1301.

53. G. T. Wondrak, M. J. Roberts, M. K. Jacobson and E. L. Jacobson (2002). Photosensitized growth inhibition of cultured human skin cells: mechanism and suppression of oxidative stress from solar irradiation of glycated proteins. J Invest Dermatol. 119: 489-498.

54. D. Darr and I. Fridovich (1994). Free radicals in cutaneous biology. J Invest Dermatol. 102: 671-675.

55. R. P. Gallagher J. M. Elwood and C. P. Yang (1989). Is chronic sunlight exposure important in accounting for increases in melanoma incidence? Int J Cancer 44: 813-815.

56. K. S-kochanek, M. Wlaschek, K. Briviba and H. Sies (1993). Singlet oxygen induces collagenase expression in human skin fibroblasts. FEBS Lett. 331:304-306.

57. C. Meewes, P. Brenneisen, J. Wenk, L. Kuhr, W. Ma, J. Alikoski, A. Poswig, T. Krieg and K. S.-Kochanek (2001). Adaptive antioxidant response protects dermal fibroblasts from UVA-induced phototoxicity. Free Radic Biol Med. 30: 238-247.

58. H. Masaki, Y. Okano and H. Sakura (1997). Generation of active oxygen species from advanced glycation end-products (AGE) under ultraviolet light A (UVA) irradiation. Biochem Biophys Res Commun. 235: 306-310.

59. M. O. Parat, M. J. Richard, M. T. Leccia, P. Amblard, A. Favier and J. C. Beani (1995). Does manganese protect cultured human skin fibroblasts against oxidative injury by UVA, dithranol and hydrogen peroxide? Free Rad Res. 23: 339-351.

60. H. Masaki and H. Sakurai (1997). Increased generation of hydrogen peroxide possibly from mitochondrial respiratory chain after UVB irradiation of murine fibroblasts. J Dermatol Sci. 14: 207-216.

61. H. Masaki, T. Atsumi and H. Sakurai (1995). Detection of hydrogen peroxide and hydroxyl radicals in murine skin fibroblasts under UVB irradiation. Biochem Biophys Res Commun. 206: 474-479.

62. R. R. Selzer, S. Nyaga, J. Tuo, A. May, M. Muftuoglu, M. Christiansen, E. Citterio, R. M. Brosh Jr and V. A. Bohr (2002). Differential requirement for the ATPase domain of the cockayne syndrome group B gene in the processing of UV-induced DNA damage and 8-oxoguanine lesions in human cells. Nucleic Acids Res. 30: 782-793.

63. Y. Shindo and T. Hashimoto (1997). Time course of changes in antioxidant enzymes in human skin fibroblasts after UVA irradiation. J Dermatol Sci. 14: 225-232.

64. J. Wenk, A. Foitzik, V. Achterberg, A. Sabiwalsky, J. Dissemond, C. Meewes, A. Reitz, P. Brenneisen, M. Wlaschek, W. M-Ingold and K. S-Kochanek (2001). Selective pick-up of increased iron by deferoxamine-coupled cellulose abrogates te iron-driven induction of matrix-degrading metalloproteinase 1 and lipid peroxidation in human dermal fibroblasts in vitro: A new dressing concept. J Invest Dermatol. 116: 833-839.

65. J-L. Ravanat, T. Douki and J. Cadet (2001). Direct and indirect effects of UV radiation on DNA and its components. J Photochem Photobiol B. 63: 88-102.

66. W. A. Bruls, H. van Weelden and J. C. van der Leun (1984). Transmission of UV-radiation through human epidermal layers as a factor influencing the minimal erythema dose. Photochem Photobiol. 39: 63-67.

67. A. M. Kligman (1969). Early destructive effect of sunlight on human skin. J Am Med Assoc. 210: 2377-2380.

68. M. Ohba, M. Shibanuma, T. Kuroki and K. Nose (1994). Production of hydrogen peroxide by transforming growth factor-β1 and its involvement in induction of egr-1 mouse osteoblastic cells. J Cell Biol. 126: 1079-1088.

69. S. M. Hahn, J. B. Mitchell and E. Shacter (1997). Tempol inhibits neutrophil and hydrogen peroxide-mediated DNA damage. Free Radic Biol Med. 23: 879-884.

70. M. C. Krishna, D. A. Grahame, A. Samuni, J. B. Mitchell and A. Russo (1992). Oxoammonium cation intermediate in the nitoxide-catalyzed dismutation of superoxide. Proc Natl Acad Sci USA. 89: 5537-5541.

71. J. Yamada, S. Yoshimura, H. Yamakawa, M. Sawada, M. Nakagawa, S. Hara, Y. Kaka, T. Iwama, T. Naganawa, Y. Banno, S. Nakashima and N. Sakai (2003). Cell permeable ROS scavengers, Trion and Tempol, rescue PC12 cell death caused by pyrogallol or hypoxia/reoxygenation. Neurosci Res. 45: 1-8.

72. G. Gille and K. Sigler (1995). Oxidative stress and living cells. Folia Microbiol. 40: 131-152.

73. R. Konaka, E. Kasahara, W. C. Dunlap, Y. Yamamoto, K. C. Chien and M. Inoue (1999). Irradiation of titanium dioxide generates both singlet oxygen and Superoxide anion. Free Radic Biol Med. 27: 294-300.

74. R. Dunford, A. Salinaro, L. Cai, N. Serpone, S. Horikoshi, H. Hidaka and J. Knowland (1997). Chemical ocidatio and DNA damage catalysed by inorganic sunscreen ingredients. FEBS Lett. 418: 87-90.